

**Layered Double Oxides/Biomass Composite:
Synthesis, Characterization and Treatment of
Antibiotic Contaminated Water**

Khawla Abdulmutalib Ahmed Azalok

Submitted to the
Institute of Graduate Studies and Research
in partial fulfillment of the requirements for the degree of

Doctor of Philosophy
in
Chemistry

Eastern Mediterranean University
February 2021
Gazimağusa, North Cyprus

Approval of the Institute of Graduate Studies and Research

Prof. Dr. Ali Hakan Ulusoy
Director

I certify that this thesis satisfies all the requirements as a thesis for the degree of Doctor of Philosophy in Chemistry.

Prof. Dr. İzzet Sakallı
Chair, Department of Chemistry

We certify that we have read this thesis and that in our opinion it is fully adequate in scope and quality as a thesis for the degree of Doctor of Philosophy in Chemistry.

Assoc. Prof. Dr. Akeem Oladipo
Co-Supervisor

Prof. Dr. Mustafa Gazi
Supervisor

Examining Committee

1. Prof. Dr. Terin Adalı

2. Prof. Dr. Aslı Baysal

3. Prof. Dr. Mustafa Gazi

4. Prof. Dr. Cumali Kınacı

5. Prof. Dr. Elvan Yılmaz

6. Assoc. Prof. Dr. Hayrettin Ozan Gülcan

7. Assoc. Prof. Dr. Akeem Oladipo

ABSTRACT

A new composite of manganese-iron layered double oxides-biochar (MnFe LDO/BC) was successfully synthesized. The as-prepared composite was characterized using Fourier-transform infrared spectroscopy, scanning electron microscope, X-ray diffractometer and time-resolved spectroscopy. MnFe LDO/BC was applied for the elimination of antibiotic residues like tetracycline (TEC) and metronidazole (MEZ) from contaminated water via adsorption and advanced oxidation processes. The performance of MnFe LDO/BC was evaluated through isotherm studies, reuse efficiency, photocatalytic and adsorption kinetics. The characterization results indicated that the MnFe LDO/BC composite has a sufficient specific surface area of 524.8 m²/g, saturation magnetization value at 28.5 emu/g, energy band gap of 2.85 eV and photocurrent response of 3.8 μA/cm². The maximum adsorption capacity of MnFe LDO/BC for TEC and MEZ was 38.3 mg/g and 40.8 mg/g at pH 3 and 5, respectively. The adsorption behavior fits the Langmuir isotherm and pseudo-second-order models with correlation coefficient $R^2 \geq 0.98$.

The composite demonstrated high photocatalytic efficiency under UV light; TEC and MEZ degradation reached ~98.0% after 60 min of UV light illumination in the presence of 50 mg of MnFe LDO/BC catalyst and 6 mM of H₂O₂. Under various antibiotics degradation processes, UV/MnFe LDO/BC/H₂O₂ demonstrated the highest degradation efficiency with a rate constant of 0.266 1/min and lowest energy consumption cost of 0.38\$ at 7.56 kWh/m³ which is ~13 times lower than the degradation of TEC and MEZ by the photolytic process under the same conditions. The radical trapping results revealed that the photocatalytic decomposition of TEC

and MEZ followed a multistage mechanism influenced mainly by HO^\bullet and $\text{SO}_4^{\bullet-}$ radicals and partially by h^+ and $^\bullet\text{O}_2^-$. The performance of the novel MnFe LDO/BC composite for antibiotics mineralization surpassed several studied catalysts and maintained ~88% reuse efficiency after three consecutive recycling tests.

Keywords: Layered double oxide biomass composite; antibiotics elimination; photocatalytic mineralization; antibiotics adsorption.

ÖZ

Bu çalışmada, yeni bir manganez-demir katmanlı çift oksit-biyokömür (MnFe LDO/BC) kompoziti başarıyla sentezlendi. Hazırlanan kompozit, Fourier dönüşümlü kızılötesi spektroskopisi, taramalı elektron mikroskobu, X-ışını difraktometresi ve zamanla çözülmemiş spektroskopisi kullanılarak karakterize edildi. Kirlenmiş sudan tetrasiklin (TEC) ve metronidazol (MEZ) gibi antibiyotik kalıntılarının adsorpsiyon ve gelişmiş oksidasyon süreçleri yoluyla ortadan kaldırılması için MnFe LDO/BC uygulandı. MnFe LDO/BC'nin performansı izoterm çalışmaları, yeniden kullanım verimliliği, fotokatalitik ve adsorpsiyon kinetiği ile değerlendirildi.

Karakterizasyon sonuçları, MnFe LDO/BC kompozitinin $524.8 \text{ m}^2/\text{g}$ değerinde yeterli bir spesifik yüzey alanına, 28.5 emu/g değerinde doygunluk manyetizasyon değerine, 2.85 eV değerinde enerji bant aralığına ve $3.8 \mu\text{A}/\text{cm}^2$ değerinde foto akım yanıtına sahip olduğunu gösterdi. TEC ve MEZ için MnFe LDO/BC'nin maksimum adsorpsiyon kapasitesi pH 3 ve 5'te sırasıyla 38.3 mg/g ve 40.8 mg/g olarak ölçüldü. Adsorpsiyon davranışı, $R^2 \geq 0.98$ korelasyon katsayısı ile Langmuir izotermine ve sözde ikinci dereceden modellere uyar.

Kompozit, UV ışığı altında yüksek fotokatalitik verimlilik göstermiştir; TEC ve MEZ degradasyonu, 50 mg MnFe LDO/BC katalizörü ve 6 mM H_2O_2 varlığında 60 dakika UV ışık aydınlatmasından sonra $\sim 98.0\%$ 'a ulaştı. Çeşitli antibiyotik bozunma süreçleri altında, UV/MnFe LDO/BC/ H_2O_2 uygulaması, 0.266 1/dak hız sabiti ve 7.56 kWh/m^3 'te $0.38 \text{ \$}$ 'lık en düşük enerji tüketim maliyeti ile en yüksek bozunma verimliliğini göstermiş olup, TEC ve MEZ'nin aynı koşullar altında fotolitik işleme

bozunması için gerekli olan enerji tüketimine kıyasla yaklaşık 13 kat daha düşük olduğunu göstermiştir. Radikal yakalama sonuçları, TEC ve MEZ'nin fotokatalitik ayrışmasının, esas olarak $\cdot\text{OH}$ ve $\cdot\text{SO}_4^-$ radikallerinden ve kısmen h^+ ve $\cdot\text{O}_2^-$ etkisi ile çok aşamalı bir mekanizmayı takip ettiğini ortaya çıkarmıştır. Antibiyotik mineralizasyonu için yeni MnFe LDO/BC kompozitinin performansı, üzerinde çalışılan birkaç farklı katalizörü geride bıraktı ve üç ardışık geri dönüşüm testinden sonra ~%88 yeniden kullanım verimliliğini korudu.

Anahtar Kelimeler: Katmanlı çift oksit biyokütle kompoziti; fotokatalitik mineralleşme; tetrasiklin ve metronidazol degradasyonu; antibiyotik adsorpsiyonu.

DEDICATION

*To my lovely husband and children, to my dear parents for their
prayers and encouragements, and my sisters and brothers.*

*This thesis is also dedicated to all those people who struggle
for a cleaner and healthier tomorrow.*

ACKNOWLEDGEMENT

First I would like to thank God Almighty who gives me the volition and power to complete my Ph. D study at EMU with success.

My deep gratitude and indebtedness first go to my great supervisor Prof. Dr. Mustafa Gazi for his unlimited support, advice, guidance and for being one of the best and a professional mentor. This work would not be possible without you.

Deeply, I thank my dear co-supervisor Assoc. Prof. Dr. Akeem for his great efforts, valuable criticism, constant encouragement, and he remained a crutch of inspiration and true guide thought to get this dissertation complete in time.

I am also grateful to all of those whom I had the pleasure to work in the faculty of pharmacy; I would especially like to thank Assist. Prof. Dr. Mehmet Garip for the experience and the knowledge I gained during the period of my work as an analytical (I) and (II) lab assistant.

Special thanks also go to all my friends, classmates and lab-mates in the department for their support all the time. And all the staff of the chemistry department for being very helpful and professional. And to my dear colleagues in the department of chemistry Dr. Ayo Ifebajo, Dr. Edith Ahaka and Dr. Faisal Mustafa, Dr. Mamoon Alokour, Abdullah, and Karar Shukur, as well as my dear officemates and friends at the Faculty of Pharmacy for their help, support and encouragement that gave me the strength to overcome all the difficulties in this journey. God bless you all guys!

Last but not the least, my utmost appreciation to my Cypriot dad and mum; Mr. Emirali and Gülay Sari, the words fail to express my great gratitude and thanks for all that you have provided me and my family. May Allah reward you.

TABLE OF CONTENTS

ABSTRACT.....	iii
ÖZ.....	v
DEDICATION.....	vii
ACKNOWLEDGEMENT.....	viii
LIST OF TABLES.....	xiii
LIST OF FIGURES.....	xiv
1 INTRODUCTION.....	1
1.1 Remediation of Antibiotic Residues via.....	3
1.1.1 Batch Adsorption System.....	3
1.1.1.1 Chemical Composition of Agricultural Waste/Biomass.....	4
1.1.2 Advanced Oxidation Processes.....	6
1.2 Objectives of This Thesis.....	11
1.3 Scope of This Study.....	12
1.4 The Framework of the Thesis.....	13
2 LITERATURE REVIEW.....	14
2.1 Photobased Treatment Approach for Wastewater.....	14
2.1.1 Photolysis Process.....	14
2.1.2 Photocatalysis.....	15
2.1.3 Fenton, Fenton-like, and Photo-Fenton.....	16
2.2 Layered Double Hydroxide LDH and Layered Double Oxide LDO.....	17
3 METHODOLOGY.....	20
3.1 Chemical Materials and Equipment.....	20
3.2 Preparation of Adsorbates.....	21

3.3 Preparation of Adsorbents.....	22
3.3.1 Preparation of MnFe Layered Double Hydroxides LDH/ Palm Seeds Powder PSP.....	23
3.3.2 Preparation of MnFe Layered Double Oxides LDO/ Biochar BC	23
3.4 Characterization of As-prepared Composite.....	24
3.5 Adsorption Experiments	25
3.5.1 Adsorption Kinetics and Isotherms	25
3.5.2 Batch Adsorption for TEC and MEZ Removal by MnFe LDO/BC.....	27
3.5.3 Desorption and Reusability Experiments	27
3.6 Photocatalytic Experiments	28
3.6.1 Photodegradation of TEC and MEZ Antibiotics by MnFe LDO/BC.....	28
3.6.2 Data Analysis and Kinetic Study for Photocatalyst Degradation of Antibiotics	29
4 RESULTS AND DISCUSSIONS.....	30
4.1 Characterization	30
4.1.1 Physicochemical Characterization of MnFe LDO/BC.....	30
4.1.2 Photocurrent Measurement and Band Gap Determination of MnFe LDO/BC Composite	34
4.2 Optimize Batch Adsorption Conditions.....	35
4.2.1 Effect of Solution pH.....	35
4.2.2 Effect of Adsorbent Dosage	40
4.2.3 Effect of Initial Antibiotic Solution with Time	41
4.2.4 Effect of Temperature.....	42
4.2.5 Comparison of Performance of MnFe LDO/BC for TEC and MEZ Removal.....	43

4.3 Kinetic and Isotherm of Adsorption Studies	44
4.3.1 Kinetic Study for TEC and MEZ.....	44
4.3.2 Isotherm Adsorption Study for TEC and MEZ	50
4.3.3 Thermodynamic Studies of TEC and MEZ Removal by MnFe LDO/BC	51
4.4 Photocatalytic Activities Results.....	52
4.4.1 Evaluation of Photocatalyst Performance of MnFe LDO/BC for Antibiotic Degradation	52
4.4.2 Effect of MnFe LDO/BC Dosage.....	55
4.4.3 Effect of H ₂ O ₂ and K ₂ S ₂ O ₈ Oxidants Concentration.....	56
4.4.4 Performance Under Optimized Conditions and Radical Trapping Test...	58
4.4.5 Degradation Kinetics of TEC and MEZ Under Various Photo-degradation Conditions.....	60
4.4.6 Proposed Mechanism for TEC and MEZ Photo-degradation Study	63
4.4.7 Comparison of Photocatalytic Performance of MnFe LDO/BC	65
4.5 Adsorptive Reusability and Photo-stability of MnFe LDO/BC Composite.....	66
4.6 Evaluation of Adsorption and Photocatalytic Performance of MnFe LDO/B...	68
5 CONCLUSION AND FUTURE WORK	69
REFERENCES	73

LIST OF TABLES

Table 1: Chemical composition of various biomass (dry basis)	6
Table 2: Some of the physical properties of selected antibiotics.....	21
Table 3: Characterization of adsorption Kinetics models (Kola’s thesis, 2017)	25
Table 4: Characterization of adsorption isotherms models (Kola’s thesis, 2017)	26
Table 5: Textural characteristics of MnFe-LDO–based materials.....	32
Table 6: Compression of monolayer adsorption capacities of TEC	43
Table 7: Compression of monolayer adsorption capacities of MEZ	44
Table 8: Kinetic parameters of TEC removal by MnFe LDO/BC at 295.15K	49
Table 9: Kinetic parameters of MEZ removal by MnFe LDO/BC at 295.15K	49
Table 10: Adsorption isotherm parameters of TEC and MEZ onto MnFe LDO/BC	50
Table 11: Thermodynamic parameters of TEC and MEZ removal by MnFe LDO/BC	52
Table 12: Degradation kinetics of TEC and correlation coefficients (R^2) under different processes	61
Table 13: Degradation kinetics of MEZ and correlation coefficients (R^2) under different processes	62
Table 14: Comparison of photocatalytic performance of MnFe LDO/BC for TEC and MEZ removal	66
Table 15: Evaluation of adsorption and photocatalytic performance of MnFe LDO/BC	68

LIST OF FIGURES

Figure 1: Adsorbent derived from biomass for removal different pollutants from wastewater effluents (Dai et al., 2018)	4
Figure 2: Chemical structure and percent composition of lignocellulosic biomass	6
Figure 3: Schematic representation and classification of different treatments based on advanced oxidation processes (AOPs) (Amor et al., 2019)	8
Figure 4: Schematic representation of typical mechanism of ADOs (reproduced with permission from Oladipo et al © 2020 John Wiley & Sons, Inc.)	8
Figure 5: Commonly used photobased techniques (reproduced with permission from Oladipo et al © 2020 John Wiley & Sons, Inc.)	14
Figure 6: Schematically presentation of LDH structure (Richetta et al., 2016).....	18
Figure 7: Calibration curves of (a) TEC and (b) MEZ	22
Figure 8: Preparation steps of MnFe LDO/BC composite.....	24
Figure 9: SEM micrographs of MnFe LDO/BC composite.....	31
Figure 10: N ₂ adsorption–desorption isotherms and pore volume and surface area distributions (inset) (a); Magnetic hysteresis loops for MnFe LDO and MnFe LDO/BC (b); XRD patterns of samples (c); and FTIR spectra of the synthesized samples (d)	34
Figure 11: Transient photocurrent responses of MnFe LDO and MnFe LDO/BC samples under visible light ($\lambda > 420$ nm) irradiation (a); and UV-vis DRS (b) and Tauc plots of both samples(b-inset)	35
Figure 12: Effect of pH on the removal of (a) TEC and (b)MEZ onto MnFe LDO/BC; (c) pH _{pzc} of the adsorbent.....	38

Figure 13: Distribution of TEC and MEZ antibiotic species and interaction with MnFe LDO/BC under varying solution pH	39
Figure 14: Effect of dosage of adsorbent on the removal of TEC and MEZ.....	41
Figure 15: Effect of initial antibiotic concentration on the removal of (a) TEC and (b) MEZ onto MnFe LDO/BC	42
Figure 16: Effect of temperature on both antibiotic systems	43
Figure 17: First order (a); second-order (b); Elovich (c); and Weber-Morris kinetic models of TEC removal	46
Figure 18: First order (a); second-order (b); Elovich (c); and Weber-Morris kinetic models of MEZ removal	47
Figure 19: Comparative investigation of (a) TEC (b) MEZ degradation under different systems	55
Figure 20: Effect of MnFe LDO/BC dosage on the degradation of (a) TEC, and (b) MEZ	56
Figure 21: Effect of H ₂ O ₂ and K ₂ S ₂ O ₈ oxidants concentration on (a-b) TEC; and (c-d) MEZ degradation	58
Figure 22: Performance under optimized conditions and radical trapping test of (a-b) TEC; and (c-d) MEZ degradation	60
Figure 23: Schematic illustration for the proposed mechanism of TEC and MEZ degradation under UV-light irradiation using MnFe LDO/BC.....	65
Figure 24: Regeneration and reuse of spent MnFe LDO/BC as adsorbent (a) and photocatalyst (b).....	68

Chapter 1

INTRODUCTION

Pharmaceutical products are polycyclic aromatic hydrocarbons compounds which are used in human and veterinary medicine, as well as agricultural activities, for the prevention and treatment of microbial diseases (Aram et al., 2020; Kalhori et al., 2017). Antibiotics, as a kind of pharmaceuticals, are widely used against bacterial infections and also as growth promoters (Alamgir et al., 2020). According to recent reports, around two hundred thousand tons of antibiotics have been consumed over the last 50 years (Aram et al., 2020). Nasseh et al., 2020 also reported that ~15% of the total manufactured drugs around the world are antibiotics, moreover, more than 70% of them are released in inactive form into the environment via faeces and urine from human and livestock and less than 30% of them are metabolized in the body (Ifebajo et al., 2019). Thus, the disposal of the antibiotic residues from municipal wastewater treatment plants led to accumulation in the aquatic systems and detected in the water surface, groundwater, soil, and even in drinking water (Zeng et al., 2018). These antibiotic residues are generally not degraded by the conventional biological treatment method due to their aromatic structures (Carrales-Alvarado et al., 2014). In the long term, they pose risks to the environment and public health (Hena et al., 2020).

Among the commonly used antibiotics, tetracycline (TEC) and metronidazole (MEZ) have enjoyed a broad usage against anaerobic bacterial and parasitic infections

(Kalhori et al., 2017). TEC antibiotics is an amphoteric molecule due to existence of multi-ionizable functional groups in their chemical structure including tricarbonyl group (C1-C3), dimethyl ammonium (C4), and phenolic diketone moiety (C10-C12) (Li et al., 2010). These groups can be protonated and deprotonated depending on the pH of the medium, thus, tetracycline can be found in different ionization species as a cation (pH 3.3), zwitterion (pH 3.3-7.7), or anion (pH 9.3) (Wang et al., 2010; Zhao et al., 2012). TEC has been used as feed additives in intensive livestock production (Wang et al., 2010). While, MEZ antibiotic; (2-(2-methyl-5-nitro-1H-imidazol-1-yl), is generally applied to treat infections caused by *Trichomonas vaginalis* and *Giardia lamblia*; which are a type of anaerobic and protozoan bacteria, or as a supplementary element to domestic fowl and fish feed (Carrales-Alvarado et al., 2014). However, the excessive consumption and misuse of these antibiotics led to their presence in various water channels posing serious health risks (Oladipo and Ifebajo 2018; Ifebajo et al., 2019).

Recently, antibiotics residues have received high attention (Vu et al., 2010), being designated as emerging and/or new compounds, due to their physio-chemical properties such as solubility in water, ionizability, polarity, and volatility that make degradability, and quantification of these residues difficult (Oliveira et al., 2020). According to the threatening risks of antibiotics that may include chronic toxic impact, allergic responses and potential development of antibiotic- resistance bacteria, carcinogenic, mutagenic and fatal abnormalities elements, quest for efficient and rapid technologies to limit its environment is extremely needed (Ifebajo et al., 2019; Aram et al., 2020). Numerous methods have been designed for the elimination of antibiotic-containing effluents (Zeng et al., 2018; Kang et al., 2010).

1.1 Remediation of Antibiotic Residues via

1.1.1 Batch Adsorption System

The adsorption treatment process is used as a wastewater treatment method for water containing both high and low concentration of organic and inorganic pollutants, due to its low-cost adsorbent, easy design and operating system. Adsorption is a surface phenomenon based on the attraction of the dissolved particle in a liquid phase (adsorbate) onto the solid surface phase (adsorbent) via physio or chemo sorption action. Various adsorbents based biomass have been synthesized and applied to remove different kinds of harmful and toxic pollutants (dyes, pesticides, drugs, oil substances, heavy metals, gases) from wastewater as shown in Figure 1.

Biomass possesses many positive features which include biodegradability, eco-friendly, with high efficiency (Liao et al., 2018), moreover, the physiochemical properties of the biomass (high surface area, multifunctional group, porosity, etc.) play an important role for the attraction of the target pollutants from the aqueous phase to the solid phase. The biosorbents can be used as it is (naturally) or it can be physically or chemically modified/activated to improve its pore size, increase oxygen or nitrogen content, chemical strength, thermal stability, as well as develop its efficiency. On the other hand, some troubles are faced in separating and regenerating spent biosorbents for many consecutive reuse cycles. To overcome these problems, researchers have directed attention towards the fabrication of magnetic biosorbent and then separating it using a magnetic separation technology, which is considered as a rapid and effective technique for separating magnetic particles (Shao et al., 2012). For instance, Cazette et al., 2016 studied the uptake of sunset yellow food dye by magnetized activated carbon derived from coconut shell (Cazette et al., 2016).

Konicki et al., 2017 synthesized magnetic Fe@graphite core-shell nanocomposite for the removal of anionic dyes (Konicki et al., 2017). Magnetic chicken bone-based biochar (MCBB) was successfully synthesized and efficiently adsorbed rhodamine-B (RB) dye and tetracycline (TEC) in multi-component systems by Oladipo et al., (2017).

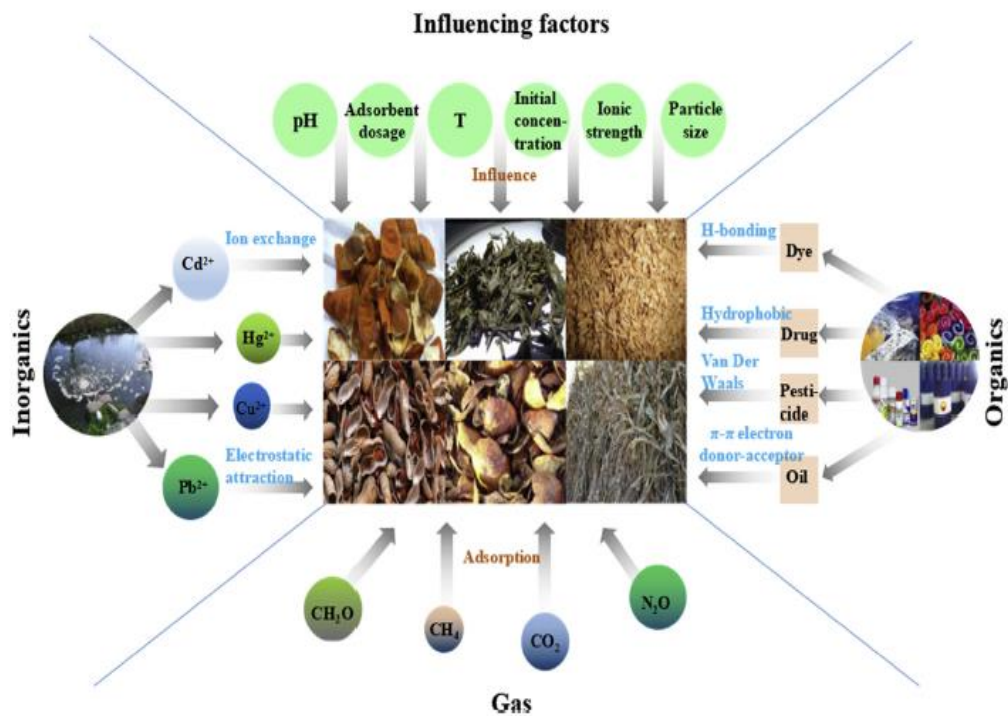


Figure 1: Adsorbent derived from biomass for removal different pollutants from wastewater effluents (Dai et al., 2018)

1.1.1.1 Chemical Composition of Agricultural Waste/Biomass

Mainly, the biomass wastes are rich in biopolymer composition in their chemical structure such as cellulose, hemicellulose, and lignin in addition to extractive materials and ash content. In other word, biomass wastes are lignocellulosic materials (Dai et al., 2018). Cellulose makes up a framework of the plant cell wall and it is a linear polysaccharide, also it consists of glucose units that are linked together by 1-4 β -D anhydroglucopyranose units with a molecular formula of

$C_6H_{10}O_5$, the strength of the plant cell walls and its Young's modulus depends on the amount of cellulose content. On the other hand, hemicellulose is located at the primary cell wall and it is a hydrophilic (Tezara et al., 2016), it is a branched heteropolymer molecule that composes of pentose (xylans), galactose units (galactans), and alternating units of mannose and glucose (mannans or glucomannans) (Ruiz et al., 2013). While a lignin component is an aromatic polyphenolic polysaccharides structure (Dai et al., 2018). Figure 2 shows the chemical structure and the percent composition of the lignocellulosic biomass materials. The percent composition of these components is varied depending on the type of crop residues (Ayeni et al., 2018; Mo et al., 2018) as shown in Table 1. This composition gives the unique chemical structure with multifunctional groups on the surface of the biomass residues like carboxyl, hydroxyl, amino, carbonyl, phosphate, methoxy, and phenol groups, etc. (Hassanein and Koumanova 2010; Basu et al., 2017). These functional groups act as binding sites to attract the toxic pollutants from contaminated water (Omo-Okoro et al., 2018).

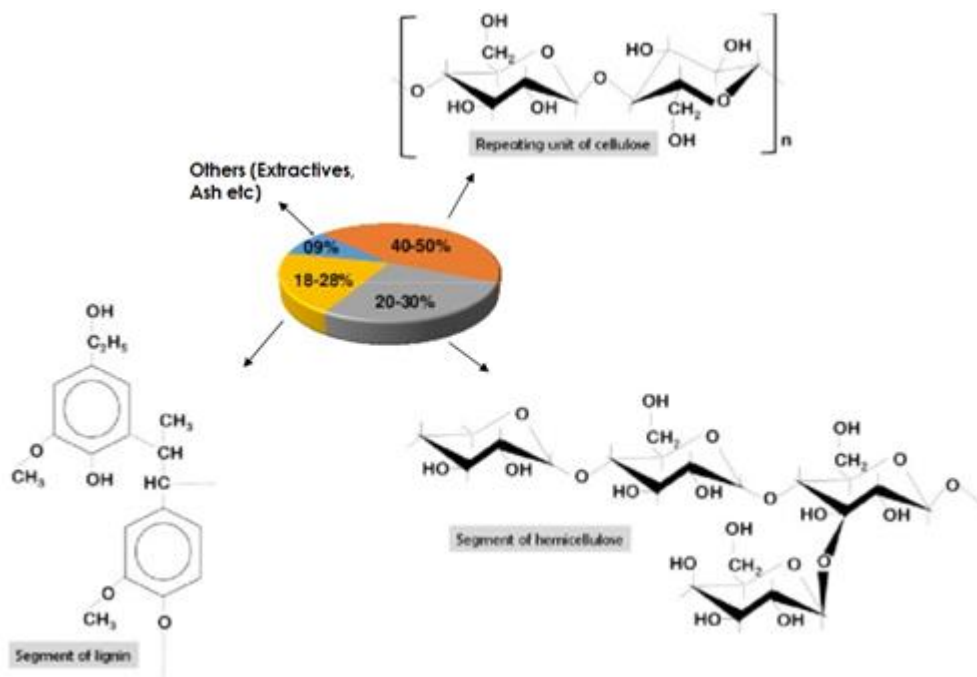


Figure 2: Chemical structure and percent composition of lignocellulosic biomass

Table 1: Chemical composition of various biomass (dry basis)

Biomass	Percent Composition				Reference
	Cellulose	Hemicellulose	Lignin	Extractives and ash	
Palm kernel shell	24.5	22.9	33.5	19.1	Chan et al. 2015
Palm meso-crap fiber	23.1	22.2	30.6	24.1	Chan et al. 2015
Empty fruit bunch	26.6	26.9	18.6	27.9	Chan et al. 2015
Rice husk	35.0	17.0	26.0	22.0	Heng et al. 2017 and Pode 2016
Sweet sorghum bagasse	35.0	23.9	16.0	25.0	Rohowsky et al.2013
Corn cobs	44.0	33.0	18.0	5.0	Wang et al.2011
Corn Stover	38.7	21.7	19.3	-	Chen et al. 2009
Sugar cane bagasse	56.0	4.59	36.4	4.2	Robl et al. 2016
Sunflower stalks	33.5	21.7	14.3	26.6	Ruiz et al. 2013

1.1.2 Advanced Oxidation Processes

Amongst all water treatment methods, advanced oxidation processes (AOPs) are promising, efficient, eco-friendly methods to remove persistent organic pollutants in wastewater effluents such as antibiotic residues. In recent years, AOPs have received high attention, due to a large number of applied research works (Anderozzi et al., 2003; Gazi et al., 2017; Oladipo et al., 2019; Oturan and Aaron 2014). These oxidation processes are characterized by the generation of highly reactive radicals with a sufficient concentration to effectively purify contaminated water at room temperature and normal pressure (Oturan and Aaron 2014). The most common radicals generated and active oxygen species used in AODs process including hydroxyl radical ($\cdot\text{OH}$), sulfate radical ($\text{SO}_4^{\cdot-}$), organic peroxy radicals ($\text{ROO}\cdot$), hydrogen peroxide (H_2O_2), ozone (O_3), persulfate ($\text{S}_2\text{O}_8^{2-}$), permanganate (MnO_4^-), chlorine dioxide (ClO_2) (Amor et al., 2019; Oh et al., 2016). The sulfate radicals are extremely reactive species between the other radicals and active oxygen species due to its high oxidation potential of $E^\circ = 2.5\text{-}3.1\text{V}$, and it possesses longer half-life, also it can selectively degrade pollutants at broader pH (1-10). The next more reactive radicals are hydroxyl radicals ($\cdot\text{OH}$) with oxidation potential of $E^\circ = 2.3\text{-}2.7\text{V}$ and pH range of 7-12 to degrade the pollutant (Hazime et al., 2014). There are several types of AOPs based on the formations methods of the radicals; homogenous or heterogeneous methods via different chemical, photochemical, sonochemical, and electrochemical reactions, as presented in Figure 3. The typical mechanism of the AODs as presented in the Figure 4, in short term, the target pollutant is oxidized either by radicals and/or oxidative species and finally mineralized into less toxic compound like carbon dioxide CO_2 , water H_2O , and others.

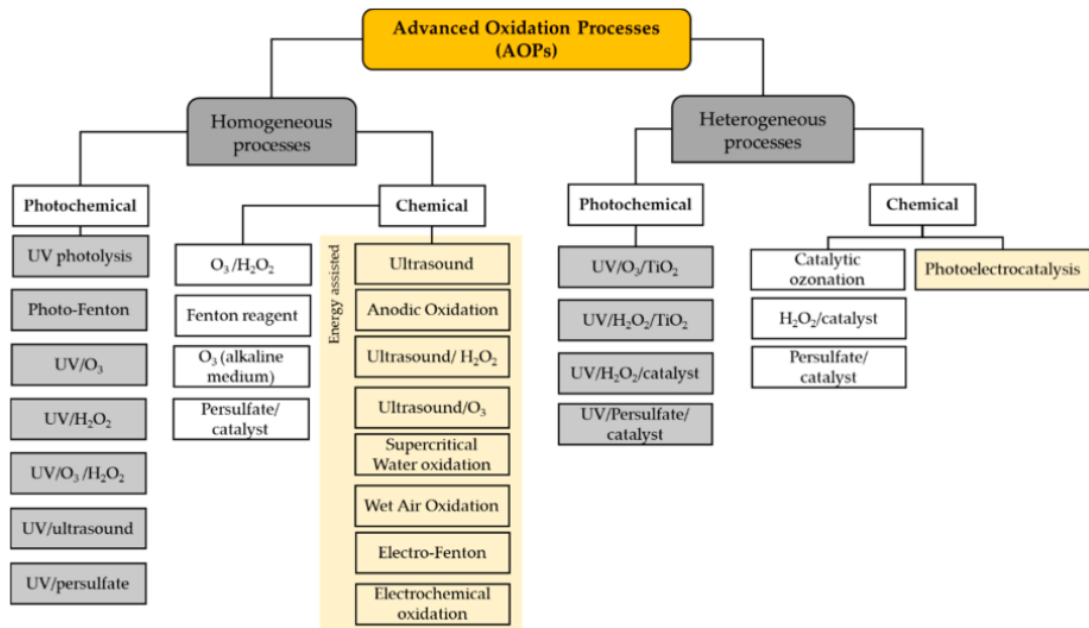


Figure 3: Schematic representation and classification of different treatments based on advanced oxidation processes (AOPs) (Amor et al., 2019)

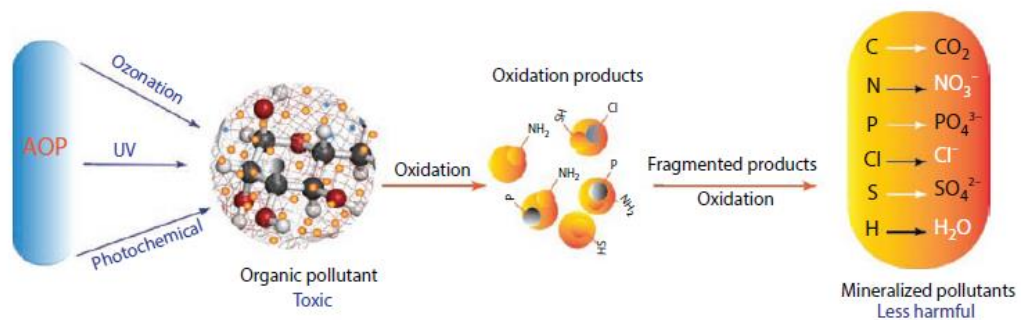
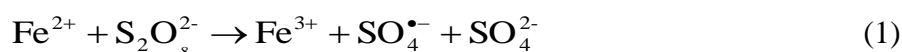


Figure 4: Schematic representation of typical mechanism of ADOs (reproduced with permission from Oladipo et al © 2020 John Wiley & Sons, Inc.)

The oxidizing free radicals can be generated using different activation agents including heat, base, activation of a transition metal, UV-light, and ultrasound (Hou et al., 2019). Among these agents, the transition metal activation method is not very complex in reactor configuration, economic compared with UV and ultrasound method that required high energy, and more favourable in an AOPs especially in the heterogeneous process (Oh et al., 2016), however, some of the metals are toxic, and non-environmental friendly, such as Co^{2+} leaching from a catalyst during the

activation process is very poisonous and high carcinogenic even at low concentration (Hou et al., 2019; Oh et al., 2016). To solve this problem, iron-, manganese-, copper-based catalyst was replaced to provide a safe and eco-friendly alternative catalyst.

The heterogeneous mixed transition metal catalysts consist at least two different metals species in their framework (Oh et al., 2016). In the scan of a transition metal, Ferrous ion Fe^{2+} is one of the most common reagents used for persulfate $\text{S}_2\text{O}_8^{2-}$ activation to produce sulfate radicals $\text{SO}_4^{\bullet-}$, because of its abundance in nature, cheap, non-toxic, and environmentally friendly (Ouyang et al., 2017; Zhu et al., 2016). The following reactions show the generation of via Fe^{2+} ions:



However, some studies have been reported that excess Fe^{2+} could react with $\text{SO}_4^{\bullet-}$ as in the reaction (2) resulting in rapid scavenging of $\text{SO}_4^{\bullet-}$ and decrease its degradation efficiency of the target pollutants (Woods et al., 1963).



Many successful attempts have been reported to avoid the quick depletion of Fe^{2+} and promote the $\text{Fe}^{2+}/\text{Fe}^{3+}$ renewal to ease $\text{S}_2\text{O}_8^{2-}$ activation. Ahmad et al., 2012 studied Fe^{2+} - EDTA (ethylenediaminetetraacetic acid) and Fe^{3+} -EDTA in $\text{S}_2\text{O}_8^{2-}$ activation system for remediation of trichloroethylene contaminated groundwater. However, the authors reported competition between the EDTA and the free $\text{SO}_4^{\bullet-}$ radicals (Ahmad et al., 2012).

Another study introduced iron nanoparticles (nFe_3O_4) as Fe^{2+} alternative to activate $\text{S}_2\text{O}_8^{2-}$ for the degradation of sulfamonomethoxine (Yan et al., 2011), regardless of

high surface energy and magnetic interaction; however, the aggregation of $n\text{Fe}_3\text{O}_4$ might decrease its activity towards persulfate activation. Also, spinel copper ferrites CuFe_2O_4 , nanoparticles were reported as a catalyst for photocatalytic degradation of 4-Chlorophenol (Manikandan et al., 2015). Zhang et al. found that nanoscale magnetic CuFe_2O_4 /Multi-Walled Carbon Nanotubes (MWCNTS) exhibited an optimal performance for persulfate activation with a mass ratio of 2:1 between CuFe_2O_4 and MWCNTS on the degradation of diethyl phthalate (Zhang et al., 2016).

Traditional single metal oxide semiconductor such as ZnO and TiO_2 have been widely used as photocatalysts to destroy many organic and pharmaceutical contaminations, like antibiotics, in wastewater effluents (Derikvandi and Nezamzadeh-Ejhih 2017). Because ZnO and TiO_2 are not toxic, have good stability, and high pH range (Bashiri et al., 2020).

In the photocatalysis process, the semiconductor is irradiated either by UV or Visible light irradiation and electron-hole pairs are generated. The photogenerated electron can react with the dissolved oxygen and produce superoxide and hydroxide radicals. These radicals can attack the pollutants in the solution and break them down into inorganic products such as water and carbon dioxide (Ifebajo et al., 2019; Essawy et al., 2020). To avoid the fast recombination rate of the photogenerated carrier which is the main drawback of the heterogeneous photocatalysis, various modified and heterojunction semiconductors have been developed (Oladipo et al., 2018). For example, mixing two or more semiconductors with different band gap energies generates a new heterostructure semiconductor, thus, effectively minimize electron-hole (e^-/h^+) pairs recombination through a charge separation of the carries.

Derikvandi & Nezamzadeh-Ejhi 2017 reported that NiS-ZnS coupled onto clinoptilolite nanoparticles NC system enhanced the charge transfer and showed the best photodegradation activity for metronidazole within 150 min irradiation time. Moreover, the photocatalytic activity of some carbon-based TiO₂ composites have been reported in the literature as a modification to improve the photocatalysis activity of TiO₂. Bashiri et al., 2020 modified the TiO₂ with Fe₃O₄/reduced graphene oxide for metronidazole degradation; the reduced graphene oxides exhibited an excellent mobility of charge carrier and reduced the electron/hole recombination. As a result, a complete mineralization of metronidazole was achieved at an optimum experimental conditions.

Some metal-containing LDHs and calcined LDOs materials received high attention and have been broadly used as photocatalysts in many industrial and environmental applications, because of their simple preparation, low cost, and high reusability (Xu et al., 2011). Generally, the photodegradation of organic pollutant using LDOs-based photocatalyst involves two main steps: (1) surface adsorption (2) decomposition of the adsorbed molecules under light irradiation. For instance, Valente et al., 2009 studied the adsorption and photocatalytic degradation of 2,4-D and phenol using Mg-Zn-Al mixed oxides, and ~97% degradation was obtained.

1.2 Objectives of This Thesis

This work aims to synthesize layered double oxides based biochar composite to efficiently remove and degrade antibiotics from contaminated water. In this research; LDOs was synthesized via co-precipitation technique and coupled with palm seed based biochar:

- The performance of palm seed-based biochar was exploited for elimination and degradation of organic contaminants
- The performance of the as-synthesized composite was investigated under various operation conditions.
- The adsorption and photocatalytic degradation mechanisms were explored and established considering characterization results and radical trapping studies.

1.3 Scope of This Study

To our best knowledge, there is no much researches have been reported on the modification of biochar with layered double oxides for antibiotics removal in the literature. Therefore, this thesis focus on the application of the novel LDO/biochar as a cost-competitive material to eliminate pharmaceuticals (tetracycline TEC and metronidazole MEZ antibiotic residues) from contaminated water effluents. The contaminated water samples used were artificially simulated in the laboratory.

The synthesized composite was characterized, and the analyte concentrations were determined using UV–vis spectrophotometer (Beijing, T80+) under lab conditions. The adsorption procedures were run in duplicate and the mean value of results were recorded. The photocatalysis process was run in a self-designed photocatalytic reactor box consisting of 4 UV-light bulbs (Fluorescent lamp T8, W5) in the presence and absence of oxidants. Also, reusability and regeneration of spent composite were assessed.

1.4 The Framework of the Thesis

Chapter 1: Introduction; introduces the challenges of antibiotic contaminated water, treatment methods and commonly used adsorbents and photocatalysts and drawbacks.

Chapter 2: Literature Review; here, a brief overview of the photobased treatment techniques and their classifications are discussed. Layered double hydroxide/oxide materials are introduced as an effective photocatalyst.

Chapter 3: Methodology; The materials, research methods and analytical characterizations used are discussed. Effects of parameters affection adsorption and photodegradation are explained including the respective data analyses details.

Chapter 4: Results and Discussions; results obtained, trend and observations are discussed and interpreted in this section.

Chapter 5: Conclusions; significant results and trends are summarized and suggestions for future work are exploited.

Chapter 2

LITERATURE REVIEW

2.1 Photobased Treatment Approach for Wastewater

Photobased technique is a promising treatment methods for destruction of persistent organic pollutants in wastewater (Molareza et al., 2016). The techniques may involve the use of oxidizing and reactive radicals which interact with organic pollutants in the presence of light and/or catalysts. In general, the organic pollutants are degraded into inorganic compounds which are considered less harmful such as water, carbon dioxide, other intermediates and salts (Oladipo et al. 2020). Below are the commonly used photobased techniques; Figure 5:

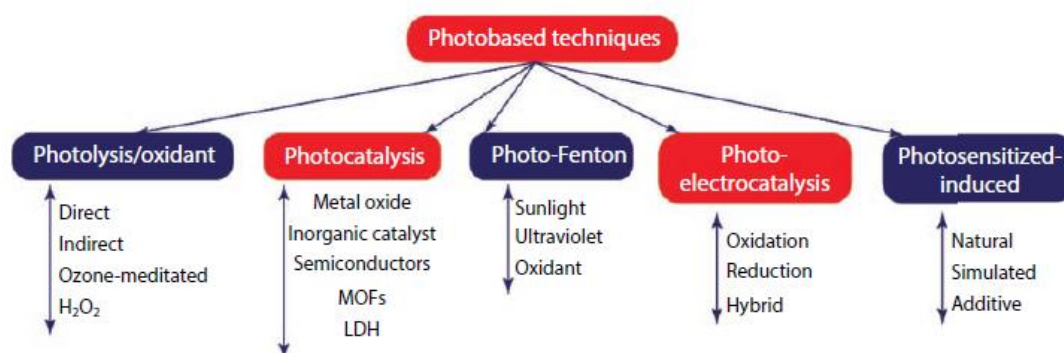


Figure 5: Commonly used photobased techniques (reproduced with permission from Oladipo et al © 2020 John Wiley & Sons, Inc.)

2.1.1 Photolysis Process

This process is the simplest photodecomposition technique that is used for degradation of organic pollutants containing wastewater. It involves a direct or

indirect chemical reaction between the light with sufficient energy and the pollutant molecules, which leads to break down of the chemical bonds present in that molecules. Several operating factors affect the rate of the photolysis process including; solution pH, the chemical structure and reactivity of the organic pollutant, the light properties, and the intensity of radiation.

In direct photolysis, there are different sources of energy that can be used in this process such as UV lamps, natural sunlight, low/medium pressured mercury lamps, solar energy simulators that radiate visible light or xenon lamps. Here, a chromophore in the target pollutant will absorb the energy of the light/photon, then either decomposes or get excited (Oladipo et al., 2020). Although, many researchers reported that it is difficult to achieve a complete mineralization for the organic pollutant using the direct photolysis, thus, the photolytic process is often aided by natural photosensitizers. Yeasmin et al., reported the photolytic degradation of Azinphos-methyl; AZM (organophosphate insecticide) using UV-A radiation and they detected the formation of N-methylanthranilic acid as a fluorescent photochemical intermediate compound (Yeasmin et al., 2009).

For indirect photolysis process which is also called sensitized photolysis process, the transient reactive species (a sensitizer such as NO_x , NO_3^- , O_3 in air/minerals, humic and fulvic acids) absorb the light then excited to the higher energy state to start sequence of reactions which may yield oxidants ($\cdot\text{OH}$ or $\text{ROH}\cdot$) that can destroy the target pollutant.

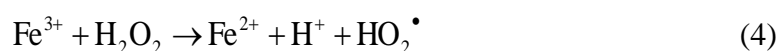
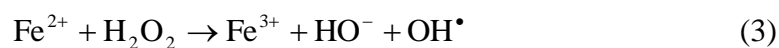
2.1.2 Photocatalysis

Photocatalysis is a mechanism that involves the production of oxidative and reductive species when photons are absorbed by one or more catalytic materials with

energy equal to or greater than their band gap energy. In its first process, the valence band (VB) and the conduction band (CB) respectively form photo-generated holes (h^+) and electrons (e^-). Consequently, these photogenerated charge carriers then react to produce reactive oxidizing species such as $\cdot\text{OH}$ and with water or dissolved oxygen, which decompose pollutants into smaller molecular compounds as well as inactivate micro-organisms. The photocatalysis process can be classified into two types; homo and hetero-geneous photocatalysis. In the homogeneous photocatalysis catalysts are in the same phase as the reaction mixture, while heterogeneous catalysts are in distinct phases. Homogeneous catalysts allow for greater interaction with the reaction mixture than heterogeneous catalysts.

2.1.3 Fenton, Fenton-like, and Photo-Fenton

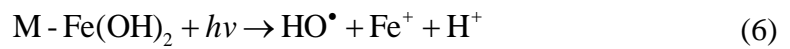
The Fenton process involves ferrous (Fe^{2+}) ions and an oxidant (usually H_2O_2) for the formation of hydroxyl radicals ($\cdot\text{OH}$) which attack the organic pollutant, as presented in the following chemical reactions (3) & (4):



Due to the high standard redox potential of $\cdot\text{OH}$ radicals (2.7 V_{SHE}), it can remove a hydrogen atom from the organic pollutant and form organic radicals that further undergo series of chemical reactions to break down the target pollutant into smaller and less toxic compounds (Kavitha and Alanivelu 2004). Despite all the advantages that the Fenton process have, such as simple in design, safe, and high performance; it has some disadvantages such as production of large quantities of sludge with high metal concentration, and mostly it works only in the acidic pH medium (Ifebajo et al., 2020). To overcome these drawbacks, the Fenton-like reaction is used. This

reaction is based on heterogeneous Fenton-like catalysts containing Fe^{2+} ions associated with other materials such as activated carbon, silica, zeolite, and resins.

In the photo Fenton-like process, the reaction is taking place in the presence of solar or ultraviolet light irradiation to enhance the overall production of OH^\bullet radicals according to these reactions, where M represents other materials;



It is worthy to mention that the photodegradation process involves adsorption of the target pollutants on the surface of the photocatalyst before photocatalytic reaction occurs via the photogenerated reactive species.

2.2 Layered double hydroxide LDH and Layered Double Oxide LDO

In recent years, researchers have directed focus towards hydrotalcite-like materials which have a special layered structure. The layered double hydroxides (LDH) are widely applied in water treatment as adsorbent, photocatalyst, electrocatalyst, and so on (Hou et al., 2019). The LDH material has a general chemical formula written as $[\text{M}^{2+}_{1-x} \text{M}^{3+}_x(\text{OH})_2]^{x+} [\text{A}_{x/n}^{n-}]^{x-} \cdot m\text{H}_2\text{O}$, where M^{2+} is the divalent such as Mg^{2+} , Mn^{2+} , and Zn^{2+} and M^{3+} is the trivalent cations like Al^{3+} , Fe^{3+} and Mn^{3+} , and $\text{A}_{x/n}^{n-}$ refers to the interlayer anion such as CO_3^{2-} , NO_3^- , Cl^- , or SO_4^{2-} . The positive charge generated by the substitution of a part of the M^{3+} by M^{2+} in the brucite-like layers was compensated by the presence of anions in the interlayer space, so called anionic clay. The schematic diagram of LDH or anionic clays presented in Figure 6 (Parida and Mohapatra, 2012). The composition of LDH is adjustable, so, the divalent and

trivalent cations, as well as the interlayer anion, can be completely or partially replaced by other ones of cations or anions (Mahjoubi et al., 2017).

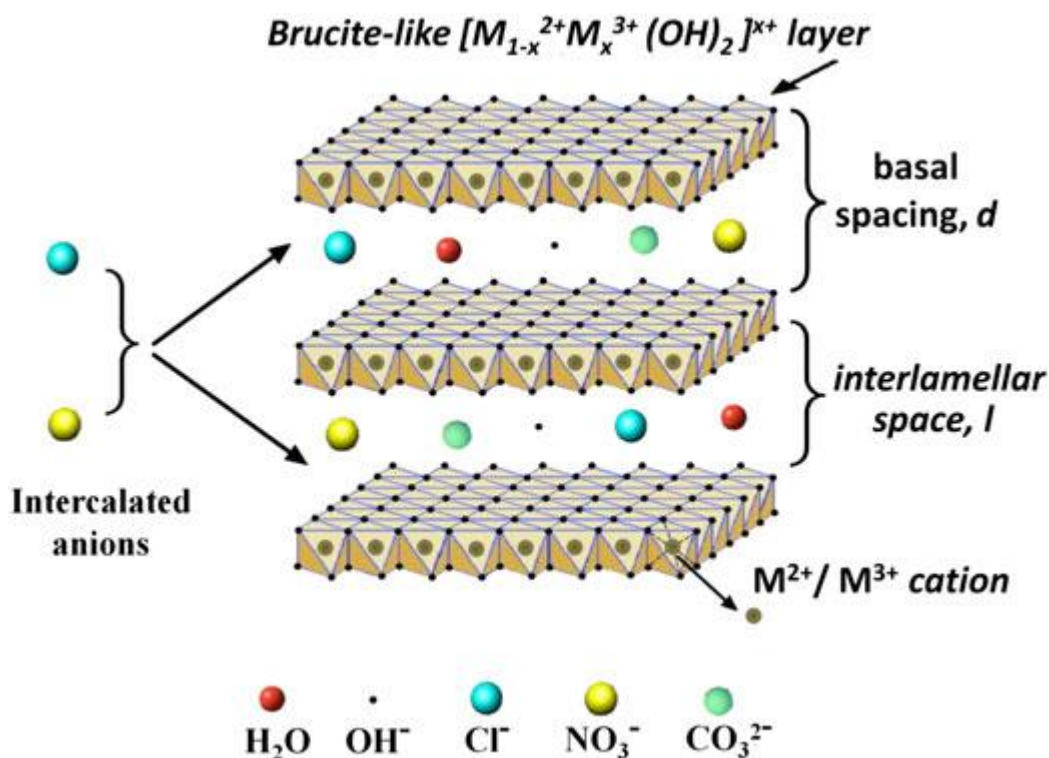


Figure 6: Schematically presentation of LDH structure (Richetta et al., 2016)

The calcination of LDH material is considered an outstanding method for producing well distributed mixed metal oxides (MMO) materials with higher photocatalytic efficiency than the conventional methods (Patnaik et al., 2017). Recently, the MMO materials have received a high attention as potential cost-competitive adsorbent, higher anion-exchange capability and effective photocatalysts, due to their intrinsic chemistries and unique “memory effect” (Zhang et al., 2020; Ifebajo et al., 2020). Chen et al. (2019) reported that MgMn-LDO exhibited superior catalytic performance, almost 97.1% of tetracycline is degraded within 20 min. Lv et al. 2018 concluded that NiAl-LDO₅₀₀ has a larger surface area than NiAl-LDH, resulting in a significant removal capacity of As (V) and reached 198.1 mg/g via intercalation through rebuilding of primary layered structure. To further improve the performance

of catalyst, recent studies have directed research focus on the addition of carbon-rich materials to pure semiconductors (Shao et al., 2012; Lai et al., 2019).

Biochar being carbon rich is a promising environmental remediation material; it possesses sufficient specific surface area and variety of oxygen-containing functional groups such as carboxyl, hydroxyl and carbonyl, which provide strong interactive reactions with pollutants. Also, biochar can be integrated with layered double oxide (LDO) materials to produce robust composites with better performance than individual component. Consistent with reports from our lab, Oladipo et al. 2019 and Ifebajo et al. 2019,2020 revealed that the combination of LDO with biochar promoted the performance, recovery and stability of the composite after spent for abatement of organic dyes. Worthy to mention that recent studies have also shown that apart from the adsorption capacity of biochar, its persistent free radicals are capable of activating H_2O_2 to generate $\cdot OH$ which further degrade organic pollutants in water (Li et al., 2019; Lai et al., 2019).

Considering the mentioned improved performance of biochar based LDO composite, magnetic recyclable MnFe LDO/biochar hybrid photocatalyst was synthesized in the study via co-precipitation-calcination technique for photocatalytic degradation of tetracycline (TEC) and metronidazole (MEZ). The morphology, structural integrity, photo-response and performance of as-synthesized hybrid photocatalyst were investigated. The TEC and MEZ degradation kinetics, probable mechanism and the reuse efficiency of the hybrid catalyst were explicated. Results herein highlights the powerful synergistic combination of layered double oxide and biochar for antibiotic mineralization.

Chapter 3

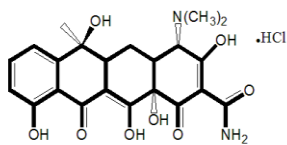

METHODOLOGY

3.1 Chemical Materials and Equipment

Agriculture biomass waste; Palm seeds were collected around the Eastern Mediterranean University campus, North Cyprus. The pharmaceutical materials; tetracycline hydrochloride and metronidazole were bought from a pharmacy located in TRNC and their physicochemical properties and chemical structure being shown in Table 2. Chemical reagents such as Ferric chloride hexahydrate ($\text{FeCl}_3 \cdot 6\text{H}_2\text{O}$; MW: 270.30 g/mol) and sodium hydroxide (NaOH), Hydrochloric acid (HCl) were purchased from Sigma-Aldrich (Germany). Manganese chloride tetrahydrate ($\text{MnCl}_2 \cdot 4\text{H}_2\text{O}$; MW: 197.90 g/mol) was manufactured by Alfa Aesar. All of these chemicals were analytical grade. The water that is used in all experiments was double-deionized water.

The laboratory pH meter (pH/Cond 720, Germany) was used for adjusting the pH of worked solutions. A conventional oven (BINDER GmbH, model BD115-EZ, Tuttlingen, Germany) was employed to dry the raw materials. For calcination process of the samples, a muffle furnace (Naberthem GmbH model, Lilienthal, Germany) was used.

Table 2: Some of the physical properties of selected antibiotics

Properties	Antibiotics	
	TEC	MEZ
Molecular mass	480.9	171.15
Maximum wavelength (nm)	360	320
pKa	3.3, 7.7, 9.7	2.5
Colour	yellow	cream
Molecular formula	C ₂₂ H ₂₅ ClN ₂ O ₈	C ₆ H ₉ N ₃ O ₃
Solubility in water	8.6	9.5
Chemical structure		

3.2 Preparation of Adsorbates

200 mg/L of fresh antibiotics (TEC and MEZ) stock solutions were prepared individually by mixing an exact amount (0.02 g) of the antibiotics powder in 100 mL double deionized water. The working solution was produced via a serial dilution of the initial stock solutions until the desired concentrations of 2-80 mg/L achieved. Then, the calibration curves were plotted (Figure 7) and the useful data were sorted out.

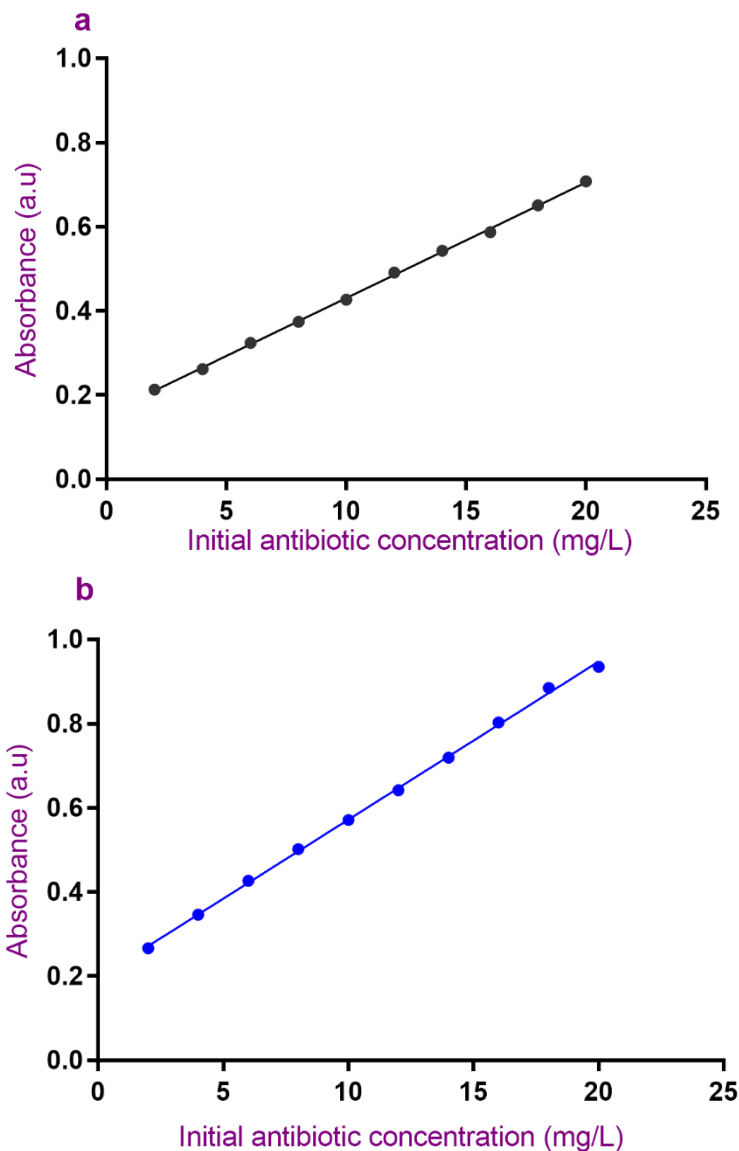


Figure 7: Calibration curves of (a) TEC and (b) MEZ

3.3 Preparation of Adsorbents

Palm seeds were collected from the palm trees around the Eastern Mediterranean University campus (Turkish Republic North Cyprus). The seeds were husked, washed many times with distilled water to remove any impurities, and then dried using a conventional oven at 80°C for two days. After that, the dried seeds were ground into powder using mortar and pestle, sieved to uniform particle size. The obtained palm seeds powder was denoted as PSP and kept in a dried place until use.

3.3.1 Preparation of MnFe layered double hydroxides LDH/ Palm seeds powder PSP

The MnFe LDH nanoparticles were prepared via co-precipitation method (Ifebajo AO, et al; 2019). Briefly, 25 mL of each of aqueous solution of $\text{MnCl}_2 \cdot 4\text{H}_2\text{O}$ (0.1 M) and $\text{FeCl}_3 \cdot 6\text{H}_2\text{O}$ (0.2 M) were mixed for few minutes in 100 mL beaker, then the mixture was dropped into 50 mL aqueous solution of NaOH (1 M) by using 60 mL syringe under constant stirring at 350 rpm at room temperature. 1 g of palm seed powder (PSP) were introduced to the system. Afterwards, the solution pH was adjusted to 9.0 by adding drops of 1 M of HCl or 1 M NaOH. The suspension product was aged for 24 h at 65°C under continuous stirring. The obtained black precipitate of MnFe LDH/PSP was washed several times with 60% ethanol followed by distilled water, then filtered and dried using a conventional oven at 80°C overnight. The dried LDH/biomass was ground by a mortar into a fine powder (as presented in Figure 8) and kept in a desiccator for further uses.

3.3.2 Preparation of MnFe layered double oxides LDO/ biochar BC

6 g of dried MnFe LDH/PSP product were placed in a clean crucible and calcined in a muffle furnace at 10°C/min was the heating rate and 500°C for 2 h under limited oxygen. The final product was designated as MnFe LDO/BC. The percentage yield and the weight loss were calculated for the product after cooling down at room temperature.

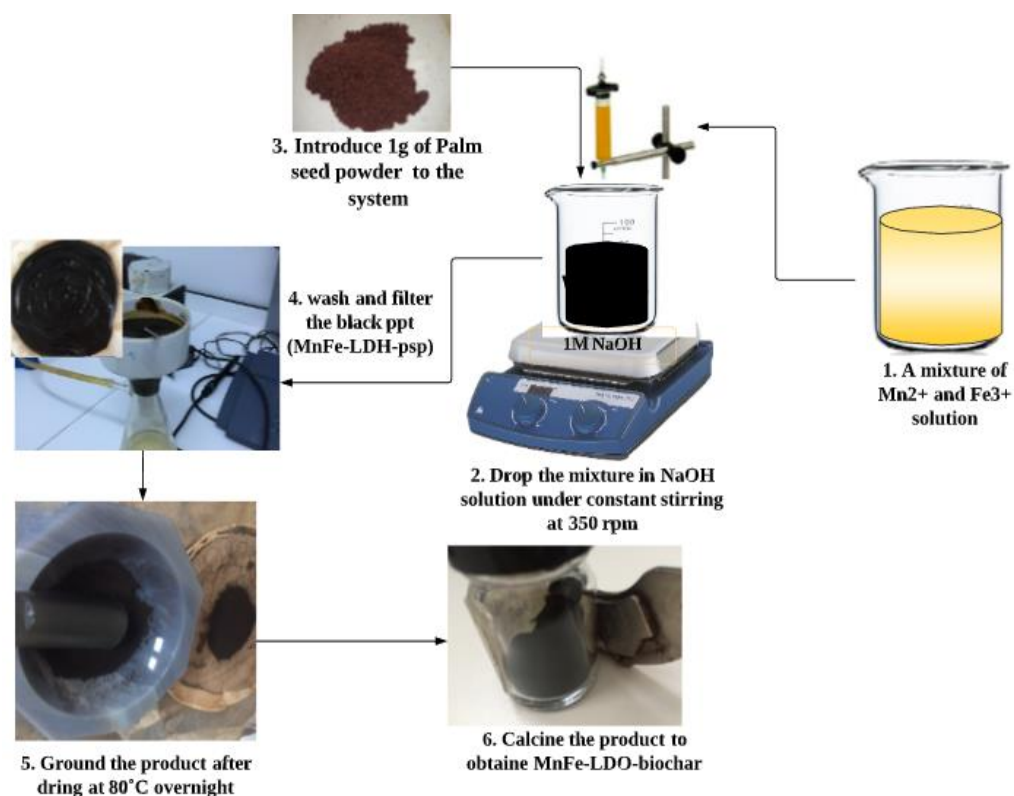


Figure 8: Preparation steps of MnFe LDO/BC composite

3.4 Characterization of As-prepared Composite

The characterizations were done at Cyprus International University, TRNC, University M'Hamed Bougara of Boumerdes, Algeria and Eastern Mediterranean University. Scanning electron microscopy SEM (JEOL, Japan) was used to characterize the morphology structure of the samples. As-prepared MnFe LDO/BC composite were subjected to N_2 adsorption-desorption isotherms at -196°C on the Autosorb analyzer (QuantaChrome, USA) to quantify the specific surface area and the size of the pores. A Vibrating sample magnetometer (VSM, 7400, lakeshore, USA) was employed to examine the magnetic properties of the samples at room temperature.

The crystallinity structure of MnFe LDO and MnFe LDO/BC samples were evaluated via X-ray diffraction XRD patterns using an advanced diffractometer

(Bruker D8, Germany) operated at 40 kV, 30 mV, step size of 2° and Cu K α radiation ($\lambda=1.5417\text{\AA}$). The obtained results were compared and matched with the standard JCPDS files. A Fourier transform infrared FTIR-8700 spectrophotometer (Perkin-Elmer, Japan) was used within the range of 4000–400 cm^{-1} to determine the functional groups. The ASTM standard procedure (Boehm analysis) was used to determine pH points zero charge (pH_{pzc}) according to the procedure reported by Oladipo & Gazi, 2015a, 2015b; Oladipo et al., 2019. The residual antibiotic concentration was determined by a double beam UV–Vis spectrophotometer (T80+, PG Instruments Ltd, UK).

3.5 Adsorption Experiments

3.5.1 Adsorption Kinetics and Isotherms

The kinetics of adsorption TEC and MEZ onto MnFe LDO/BC were investigated using pseudo-first, pseudo-second order models, Elovich and intraparticle diffusion kinetic models (Mehr et al., 2019). The related equations are mentioned in Table 3. This step helps to characterize the dynamic behaviour of the adsorption process and to provide information about the uptake rate of the adsorbent (Oladipo et al., 2019).

Table 3: Characterization of adsorption Kinetics models (Kola's thesis, 2017)

Model type	Linear form	Description	Reference
Pseudo-first-order (Physiosorption)	$\ln(q_e - q_t) = \ln q_e - k_1 t$	k_1 (1/min) is the first-order rate constant,	Li et al., 2018
Pseudo-second-order (Chemisorption)	$\frac{t}{q_e} = \frac{1}{k_2 q_e^2} + \frac{t}{q_e}$	k_2 (g/mg min) is the second-order rate constant,	Heydaripour et al., 2019

Elovich (Heterogeneous)	$q_t = \alpha + \beta \ln t$	α (mg/g min) and β (g/mg) are the initial Elovich sorption and desorption rate constant at time t , respectively.	Oladipo et al., 2018
Weber-Morris intra-particle diffusion (rate limiting step)	$q_t = k_p t^{1/2} + C$	K_p is the intraparticle diffusion rate constant (mg/g min), and C is a constant refers to the thickness of the boundary layer (g/mg).	Oladipo et al., 2018

* q_e and q_t are the amount of antibiotics species adsorbed at equilibrium and time t per unit mg/g, respectively.

The study of adsorption isotherm was also considered and four general models were applied (Table 4) on the experimental results to understand the interactions between the adsorbate molecules and the solid phase of the adsorbent (Oladipo et al., 2018).

Table 4: Characterization of adsorption isotherms models (Kola's thesis, 2017)

Model types (predictions)	Equation	Description	Reference
Langmuir (Homogeneous adsorption)	$C_e/q_e = 1/q_m b + C_e/q_m$	q_e and q_m are the equilibrium and maximum adsorption capacity (mg/g), b is Langmuir constant (L/mg) C_e is equilibrium concentration of pollutants (mg/L).	Shrestha et al., 2014
Freundlich (Heterogeneous adsorption)	$\log q_e = \log k_F + n \log C_e$	q_e is equilibrium uptake capacity; K_F is Freundlich constant related to bond energies; n is a constant indicative of sorption intensity.	Wang and Chen, 2009
Temkin	$q_e = B_1 \ln k_T + B_1 \ln C_e$ $B_1 = \frac{RT}{b_T}$	R is the universal gas constant (8.314 J/mol k), T is the absolute temperature. K_T (L/mg) is the maximum binding energy, and B_1 is the heat of adsorption (kJ/mol); b_T is Temkin isotherm constant.	Wang and Chen. (2009)
Dubinin-Radushkevich	$\ln q_e = \ln q_m - k_{D-R} \varepsilon^2$ $E = \frac{1}{\sqrt{2} k_{D-R}}$	ε is Polanyi potential; k_{D-R} is D-R constant related to the mean free energy of adsorption. E is mean energy of sorption	Matouq et al., 2015

Redlich-Peterson	$\frac{C_e}{q_e} = \frac{1}{k_{rp}} + C_e^g \frac{a_{rp}}{k_{rp}}$	K _{rp} and a _{rp} are R-P equilibrium constant; g is exponent constant value from (0–1). When (g = 1, R-P equation → Langmuir equation).	Oladipo et al., 2019
-------------------------	--------------------------------------------------------------------	------------------------------------------------------------------------------------------------------------------------------------------------------------	----------------------

3.5.2 Batch Adsorption for TEC and MEZ Removal by MnFe LDO/BC

All the adsorption experiments for removal antibiotics were carried in a 100 mL of Erlenmeyer flask with 50 mL antibiotic solution and 50 mg of adsorbent under electronic shaker at 350 rpm. The effect of batch parameters such as pH (2-11), adsorbent amount (50, 70, 100, 150 mg), adsorbate concentration (20-80 mg/L) at different time intervals on the removal of the antibiotic were investigated. All the experiments were run in duplicates and the average value recorded with the standard deviation of %. The amount of antibiotics adsorbed in mg/g on MnFe LDO/BC; removal capacity q_e , and removal efficiency R (%) were computed using the related Eqs. (7 and 8) as mentioned in the other studies (Oladipo et al., 2018; Oladipo et al., 2019).

$$\text{Removal capacity } q_e (\text{mg /g}) = (C_i - C_e) \times \frac{V}{m} \quad (7)$$

$$\text{Removal efficiency R (\%)} = \frac{(C_i - C_e)}{C_i} \times 100 \quad (8)$$

where C_i and C_e are the initial and equilibrium concentrations (mg/L); respectively, V is the volume of the antibiotic solution (L) and m is the mass of the adsorbent (g).

3.5.3 Desorption and Reusability Experiments

The evaluation of reusability and the stability of MnFe LDO/BC were studied through four consecutive adsorption-desorption cycles. Herein, the adsorbent reuse cycle was operated at the optimum conditions of 50 mL of 20 mg/L antibiotic concentration in a 100 mL conical flask at an optimum pH for 4 h. The absorbance of

residual TEC and MEZ solutions concentration was recorded and the uptake adsorption was calculated in each cycle. The used MnFe LDO/BC was eluted by 0.1 M NaOH solution under 1 h agitation at 250 rpm. The eluted MnFe LDO/BC was washed three times with distilled water and regenerated at 80°C for 1 h, then subjected to successive reuse cycles (Oladipo et al., 2018). This was also done for the MnFe LDO/BC used in photo-degradation process.

3.6 Photocatalytic Experiments

3.6.1 Photodegradation of TEC and MEZ Antibiotics by MnFe LDO/BC

The degradation of tetracycline and metronidazole antibiotics via photocatalysis process using UV- light irradiation (Fluorescent lamp T8, W5) was evaluated. The effect of catalyst concentration (0.025, 0.05, and 0.075 g/L) was investigated using 50 mL of 20 mg/L antibiotics solution in 100 mL Erlenmeyer flask in the presence and absence of (4, 6, and 8 mmol) of H₂O₂/ K₂S₂O₈. The mixture was mechanically shaken at 200 rpm for 30 min in dark in order to achieve the adsorption-desorption equilibrium on the catalyst surface (Oladipo 2018). All the studied experiments were carried out at the optimum pH. The used MnFe LDO/BC was separated from the bulky solution by an external magnet, and then 2 mL of the solution was taken out at scheduled time intervals as 30, 60, 120, 180, 240, and 300 min. The concentration of the supernatant antibiotic was detected at 360 nm for TEC and 320 nm for MEZ by using UV-vis spectrophotometry double beam (T80+PG Instruments Ltd, UK). Radical trapping studies were followed by the addition of scavengers (state quantity and which scavengers) into the solutions.

3.6.2 Data Analysis and Kinetic Study for Photocatalyst Degradation of Antibiotics

The degradation efficiency E% and reaction kinetics for photocatalyst degradation of TEC and MEZ antibiotics were calculated using the following Eqs. (9) and (10), respectively:

$$E\% = 1 - \left(\frac{C_t}{C_o} \right) \times 100 \quad (9)$$

$$\ln \left(\frac{C_t}{C_o} \right) = -k_{app} \times t \quad (10)$$

where,

C_o and C_t (mg/L) represent the initial TEC or MEZ concentration before irradiation and at selected times, respectively; while k_{app} (1/min) is the apparent pseudo-first-order rate constant; and t is time. The apparent rate constant values were calculated by applying the method of the linear regression of plotting Eq. 10.

Chapter 4

RESULTS AND DISCUSSIONS

4.1 Characterization

4.1.1 Physicochemical Characterization of MnFe LDO/BC

The SEM images of as-prepared samples are presented in Figure 9 (a-c). MnFe LDO/BC possess rough aggregated wrinkled pores surface (Figure 9 a). The highlighted sections revealed that the surface contained a reconstructed hexagonal lamellar-like structure, which is characteristic of the layered double oxide morphology (Ifebajo et al., 2019). Figure 9 b shows a smoother lamellar-like structure of MnFe LDO morphology which became roughened after the addition of biochar (Figure 9 c). Worthy to mention that the MnFe LDO/BC maintained the characteristics morphologies of both biochar and MnFe LDO with obvious interconnected pores with wrinkled edges that influenced its surface adsorption and photocatalytic properties (Shao et al., 2012).

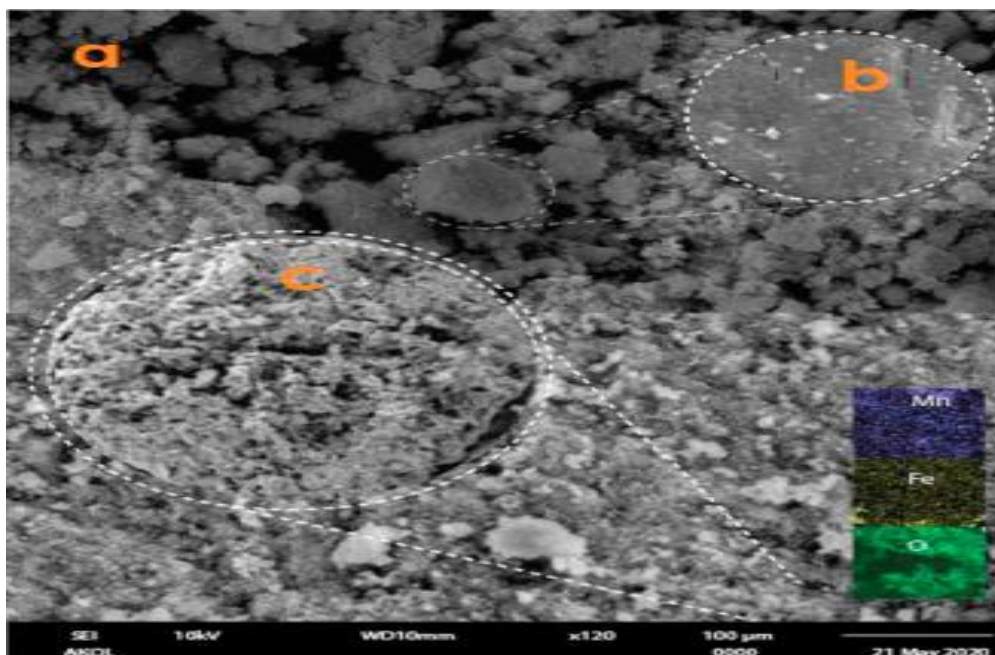


Figure 9: SEM micrographs of MnFe LDO/BC composite

The results of N_2 adsorption-desorption isotherm studies of the MnFe LDO/BC and MnFe LDO samples are shown in the Figure 10 a. It is clear that the samples exhibit I and IV isotherm types with H4 hysteresis in the relative pressure > 0.7 , which indicates the presence of mesopores (2-50 nm) and micropores (< 2 nm) according to IUPAC pores classification. As seen in the inset of Figure 10 a, the pore size distribution of MnFe LDO/BC was determined from desorption data using the BJH equation (Li et al., 2018). Suggesting the presence of narrow slit-shaped mesopores typical of LDH-based materials. The specific surface area S_{BET} , micropores surface area S_{mic} , micropores volume V_{mic} , and mesopore volume V_{mes} of the samples are tabulated in Table 5. The V_{mes} and average pore diameter D_p values, as well as S_{BET} and total pore volume V_t of MnFe LDO/BC were higher than the other samples which can provide the good conditions for the migration of antibiotic molecules (Oladipo et al., 2019; Li et al., 2018).

Table 5: Textural characteristics of MnFe-LDO-based materials

Samples	Nitrogen adsorption-desorption							Magnetic properties		
	Pore volume (cm ³ g ⁻¹)		Surface area (m ² g ⁻¹)			Pore size (nm)	M _s	H _c	M _r	
	^a V _t	^b V _{mes}	^c V _{mic}	^d S _{BET}	^e S _{mic}	^f S _{ext}	^g D _p	emu g ⁻¹	O _e	emu g ⁻¹
Biochar	0.86	0.23	0.63	389.5	173.9	215.6	2.36	0	0	0
MnFe-LDO	0.73	0.18	0.55	276.9	157.5	119.4	1.98	33.9	9.11	28.9
MnFe-LDO-biochar	0.95	0.54	0.41	524.8	169.1	355.7	3.65	28.5	7.32	23.7

a Total pore volume measured at P/Po~ 0.99.

b Mesopore volume obtained by deducting V_{mic} from V_t.

c Micropore pore volume obtained from the t-plot.

d Brunauer–Emmett–Teller specific surface area obtained via N₂ adsorp. isotherm at P/Po = 0.05–0.35.

e Micropore surface area from the t-plot.

f External surface area obtained by deducting S_{mic} from S_{BET}.

g The average pore diameter calculated by 4V_t/S_{BET}, assuming an open-ended cylindrical pore model.

Note: The cross-sectional area of the N₂ is assumed to be 0.162 nm².

Figure 10 b demonstrates the magnetic hysteresis loop for MnFe LDO/BC and gives (28.5 emu/g) specific saturation magnetization, (23.7 emu/g) retention, and 7.32O_e of coercivity which proves MnFe LDO/BC can be separated using an external magnetic field. The existence of the biochar in MnFe LDO/BC decreased its magnetic properties values in comparison with the value of pure MnFe LDO sample (33.9 emu/g, specific saturation magnetization; 28.9 emu/g, retention; and 9.11O_e, of coercivity) (Oladipo et al., 2020).

The crystallinity structure of the synthesized MnFe LDH and MnFe LDO/BC was investigated by XRD analysis as seen in Figure 10 c. The results show that the MnFe LDH sample contain diffraction peaks at 2θ = 24.5°, 31.2°, 37.3°, 41.2°, 45.3°, 51.7° which are well indexed to the crystal planes (012), (104), (110), (133), (202) and (018), respectively. The observed peaks in the XRD pattern could be excellently indexed to the cubic spinel MnFe₂O₄ (JCPDS card 10-0319). The interlamellar

spacing (d_{300}) was determined as 8.9 Å. Shao et al., 2012 and Zhen et al., 2008 reported the same results. Notable, after coupling and calcination, the intensity of the peaks weakened or disappeared, due to the collapse of the layered structure of LDH after calcination. Additionally, the new peaks were observed at $2\theta = 57.2^\circ$ and 62.7° with indices of (440) and (511) that related to the diffraction reflections of MnFe_2O_4 which matched with the standard (JCPDS No. 10-0319) (Oladipo et al., 2019).

The FTIR spectrum of MnFe LDO/BC composite showed in Figure 10 d. For the MnFe LDH spectrum, the broad peak at 3368 cm^{-1} is related to the stretching vibration of O–H groups in the intercalated water molecules and hydroxide-like brucite layers (Hou et al., 2019). The weak peak at 1631 cm^{-1} is either due to bending vibrations of the interlayers or the H–O–H group of adsorbed water of the MnFe LDH (Oladipo et al., 2019). Notably, the observed peaks located at 1032, 545.66 and 878.61 cm^{-1} could be attributed to the Cl^- ions in the interlayer of the MnFe LDH, Fe-OH, Mn-OH OH, Fe-O and Mn-O, respectively (Li et al., 2016). For the MnFe LDO/BC, the peak at $\sim 3368\text{ cm}^{-1}$ and peak at 1631 cm^{-1} was weakened. New peak around $1400\text{--}1500\text{ cm}^{-1}$ appeared and ascribed to the aromatic structure of the biochar. The intense peak around 545 cm^{-1} is ascribed to the mixed metal oxide (MnFe_2O_4) which is consistent with the XRD data.

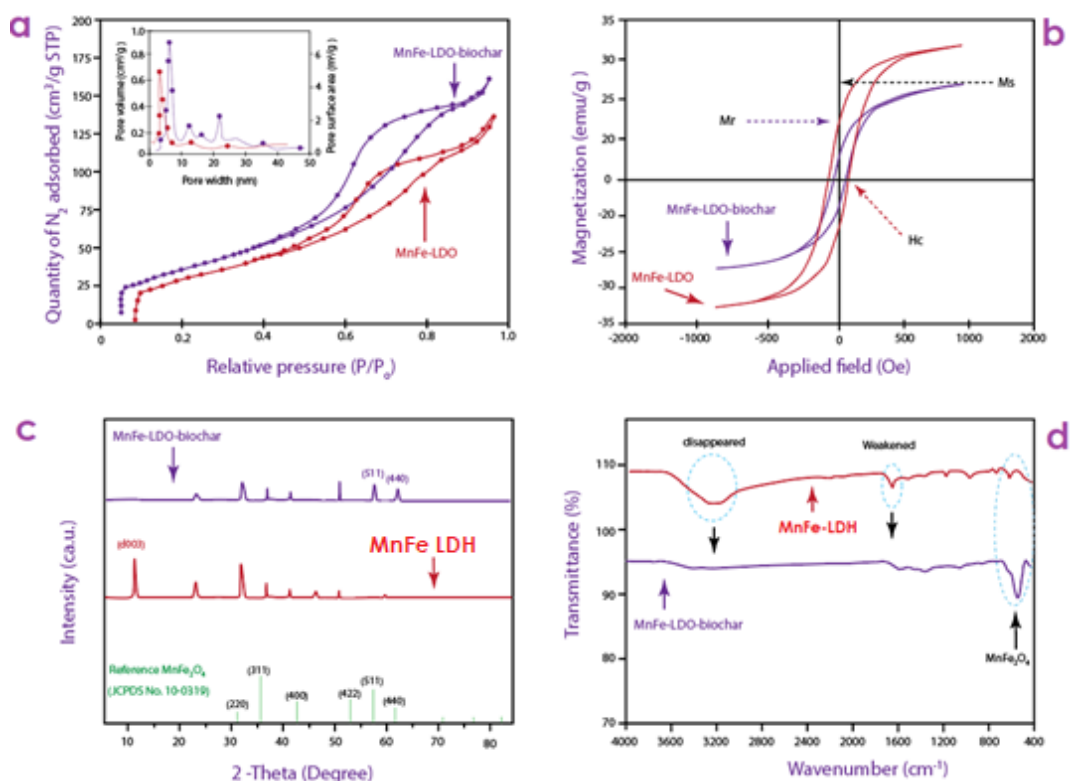


Figure 10: N₂ adsorption–desorption isotherms and pore volume and surface area distributions (inset) (a); Magnetic hysteresis loops for MnFe LDO and MnFe LDO/BC (b); XRD patterns of samples (c); and FTIR spectra of the synthesized samples (d)

4.1.2 Photocurrent Measurement and Band Gap Determination of MnFe LDO/BC Composite

Figure 11 illustrates the transient photocurrent response of as-prepared MnFe LDO and MnFe LDO/BC which was carried out under visible light irradiation ($\lambda > 420$) for four on/off sequential cycles (Atacan et al., 2020), to evaluate the photo-generated charge separation efficiency of the samples. The MnFe LDO/BC sample exhibited the larger photocurrent density ($3.7 \mu\text{A cm}^{-1}$) than MnFe LDO ($2.7 \mu\text{A cm}^{-1}$). Thus, the separation and transfer of photo-excited electrons and holes of MnFe LDO/BC are more rapid and efficient than that generated by MnFe LDO. This results indicating that as-prepared of MnFe LDO/BC may display higher photocatalytic activities (Zhao et al., 2020).

Moreover, it is observed from the photocurrent density versus wavelength of the samples that both of them can absorb visible-light (Figure 11 b), also, the band gap energy E_g of MnFe LDO and MnFe LDO/BC were computed as 3.11 and 2.85 eV, respectively by the plot of transformed Kubelka Munk function versus the bandgap energies (Figure 11 b-inset) (Atacan et al., 2020; and Jaing et al., 2020).

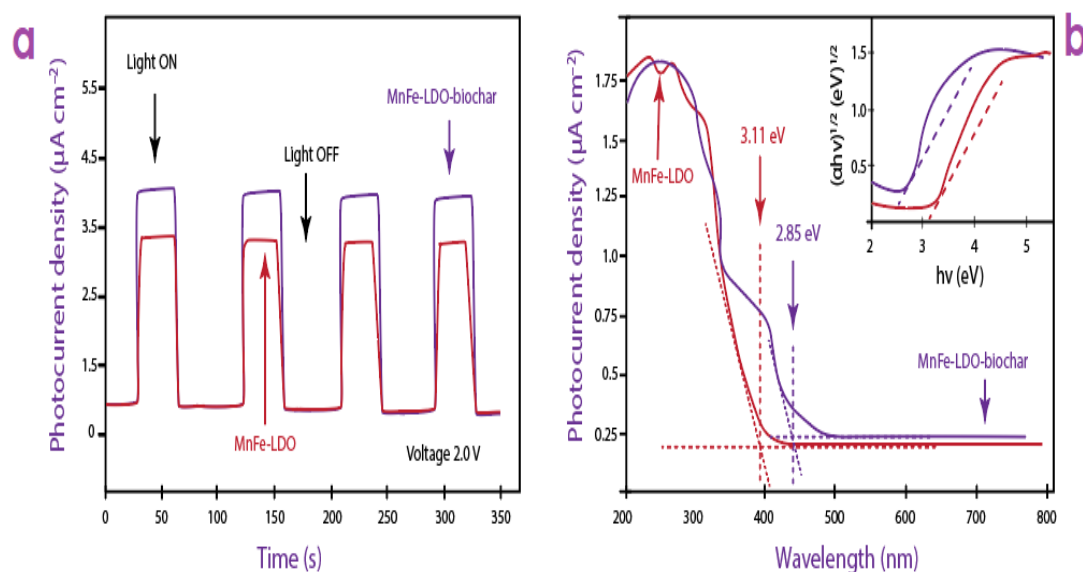


Figure 11: Transient photocurrent responses of MnFe LDO and MnFe LDO/BC samples under visible light ($\lambda > 420$ nm) irradiation (a); and UV-vis DRS (b) and Tauc plots of both samples(b-inset)

4.2 Optimization Batch Adsorption Conditions

4.2.1 Effect of Solution pH

The influence of the solution pH on the removal of TEC and MEZ antibiotic solution was examined to establish the adsorptive performance of the MnFe LDO/BC is demonstrated in Figure 12 a and b. Here, 20 mg/L of the antibiotic solution was used when the pH was varied from 2 to 11. In the case of TEC solution, the adsorptive performances of biochar, MnFe LDO and MnFe LDO/BC were investigated. It is clear that the removal efficiency increased from ~28.9% at pH 2 to 60.5, 73.3, and

80.1% at pH 3 in the presence of 50 mg biochar, MnFe LDO, and MnFe LDO/BC, respectively, after 24 h contact. The removal efficiencies increased slightly and remained nearly stable when the pH was raised between pH 3.3 and 7.7, then decreased remarkably beyond pH 10. These results could be attributed to the pH-dependent speciation of TEC ($pK_a = 3.3, 7.7, \text{ and } 9.7$), and the surface charge of the adsorbent (Figure 12 c; $pH_{pzc}=8.0$) (Oladipo and Ifebajo 2018). TEC can be present in three different molecular species in the aqueous phase, it can exist as a cation, below pH 3.3; due to the protonation of dimethylammonium group, as a zwitterion, between pH 3.3 and 7.7; when the phenolic diketone moiety is deprotonated, and as an anion above pH 7.7; resulting from the loss of protons from the tricarbonyl system and phenolic diketone moiety (as presented in Figure 13).

At pH 3, the TEC adsorption by the biochar, MnFe LDO and MnFe LDO/BC is not based on electrostatic interaction; because the surfaces of these adsorbents were positively charged at pH below the pH_{pzc} which electrostatically repelled the predominant cationic TEC species. Hence, the adsorption in this region is attributed to other interactions such as the pore filling, biochar- π - π -TEC interaction and/or cation exchange between the adsorbents and cationic TEC species. On the other hand, electrostatic attraction occurred between the zwitterionic (neutral) form of TEC and the adsorbents at neutral pH while the lower TEC removal observed at the highly alkaline pH is due to electrostatic repulsion between the negatively charged MnFe LDO/BC ($pH > pH_{pzc}$) and the predominant anionic TEC species (Shao et al., 2012, Liu et al., 2012).

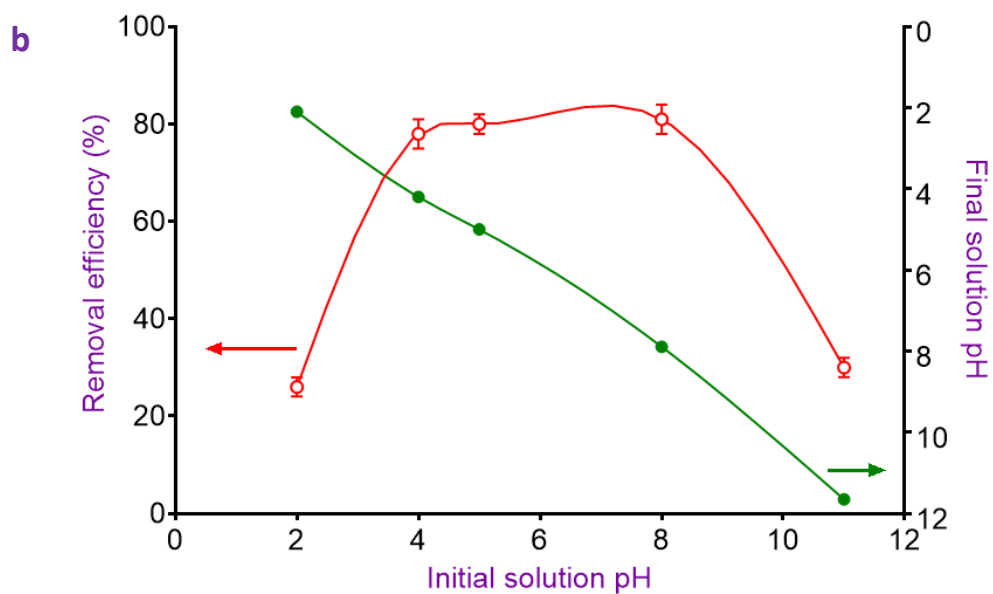
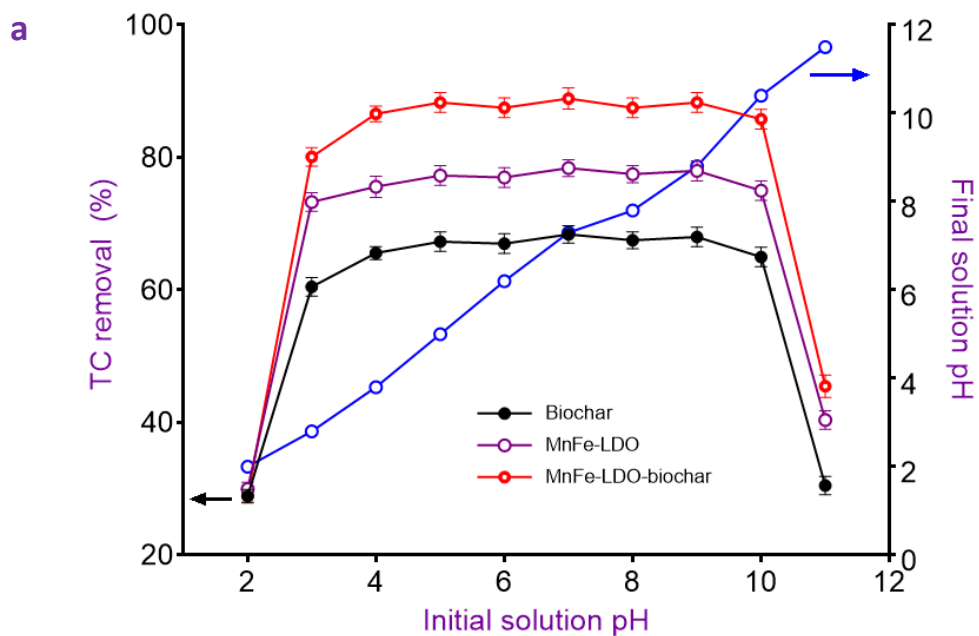
Similarly, The MnFe LDO/BC removal efficiency of MEZ increased rapidly from 26.5% at pH 2 to 78.8% at pH 4 while the removal efficiency remained nearly stable

beyond pH 4 until it reached pH 8. A decreasing trend is noticed when the solution pH is increased after pH 8. The observed adsorption trend is attributed to the combination of surface chemistry of the MnFe LDO/BC ($\text{pH}_{\text{pzc}} = 8.0$; Figure 12 c) and the pH dependent distribution of MEZ ($\text{pK}_a = 2.5$).

At $\text{pH} \leq 2.5$, the MEZ molecule is almost in a protonated form (as cation species). This explains the lower adsorption of MEZ at pH 2 which is due to the electrostatic repulsion between the positively charged surface of MnFe LDO/BC⁺ and the cationic MEZ as illustrated in Figure 13 (Carrales-Alvarado et al., 2014). As the solution pH is adjusted beyond 2.5, the MEZ⁻ anionic form prevails (Bashiri et al., 2020) and can act as an electron donor and acceptor due to its aromatic and electron-deficient structure (Asgari et al., 2019).

As the pH increases, the concentration of the H⁺ decreases and unable to hinder the approach of MEZ⁻ to the MnFe-LDO/BC⁺ surface leading to increased removal efficiency. So between pH 3 to 8, the MEZ adsorption can occur via electrostatic attraction between anionic MEZ⁻ and MnFe-LDO/BC⁺, anion exchange between the LDO and anionic MEZ species, hydrogen bonding, π - π interaction between MEZ aromatic structure and the biochar aromatic moiety. Beyond pH 8, the surface of the catalyst becomes negative (MnFe-LDO/BC⁻) and electrostatically repelled the anionic MEZ⁻ (Bashiri et al., 2020; Asgari et al., 2019; Nasseh et al., 2020; Aram et al., 2020). During reactions, the final pH of TEC solution decreased slightly particularly at highly acidic medium while it remained relatively stable or slightly higher in other cases. The lower the final solution pH relative to the initial pH the more the leaching amount of the constituent metal ions (Mn and Fe ions). Results

herein revealed that the MnFe-LDO/BC is stable and can be used under a wide pH condition (Figure 12 a).



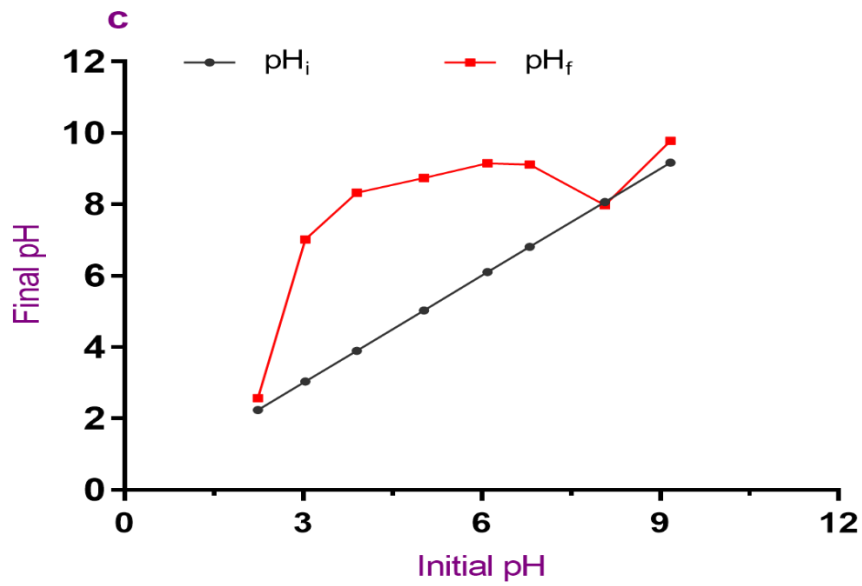
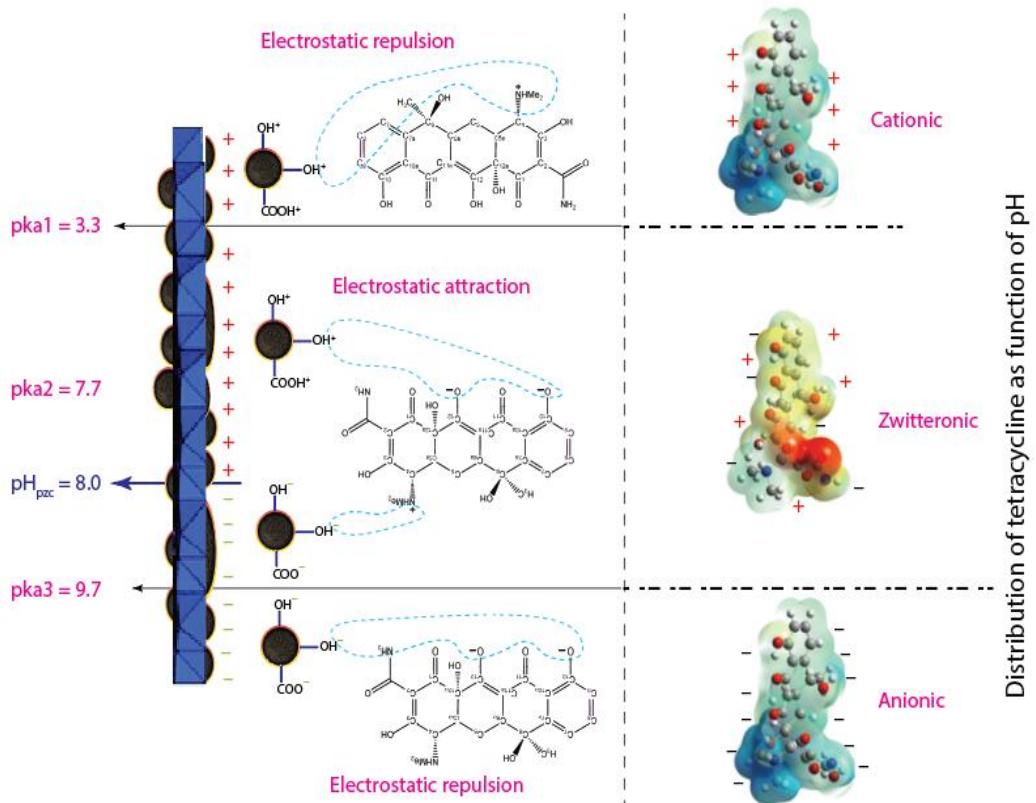


Figure 12: Effect of pH on the removal of (a) TEC and (b) MEZ onto MnFe LDO/BC; (c) pH_{pzc} of the adsorbent



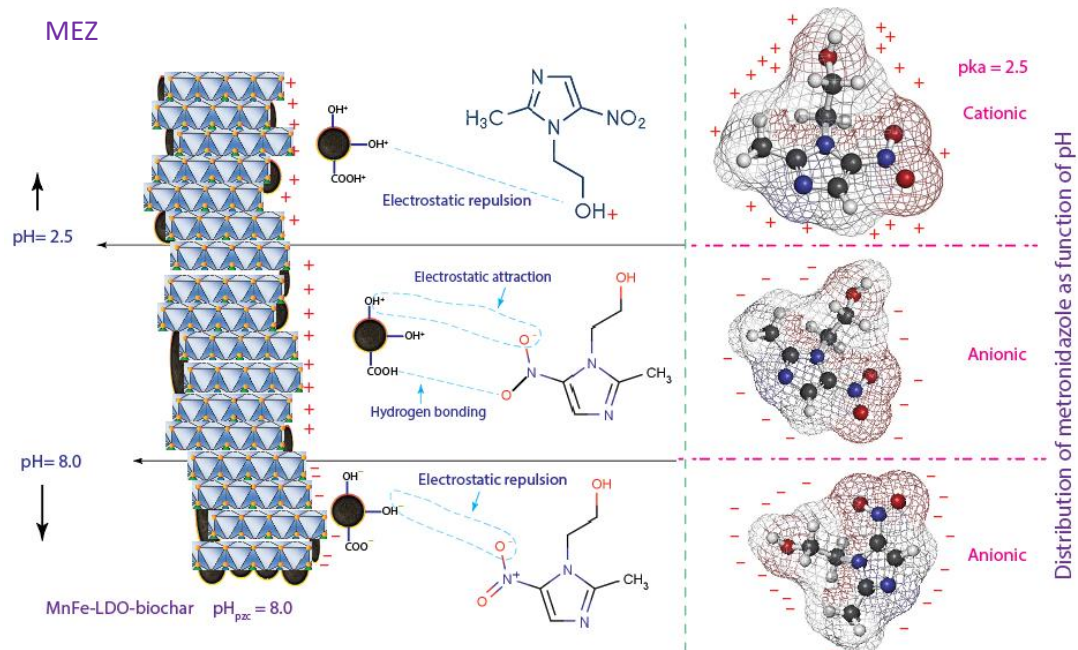


Figure 13: Distribution of TEC and MEZ antibiotic species and interaction with MnFe LDO/BC under varying solution pH

4.2.2 Effect of Adsorbent Dosage

As seen in the Figure 14, the amount of both antibiotics adsorbed per unit mass of MnFe LDO/BC drastically decreased from 16.85 to 7.08 mg/g of TEC and from 17.11 to 5.5 mg/g for MEZ as the dosage of the adsorbent increases from 0.05 to 0.150 g/L. Due to the agglomeration phenomenon of the adsorbent that may cause the reduction of the availability of active sites (Oladipo et al., 2019).

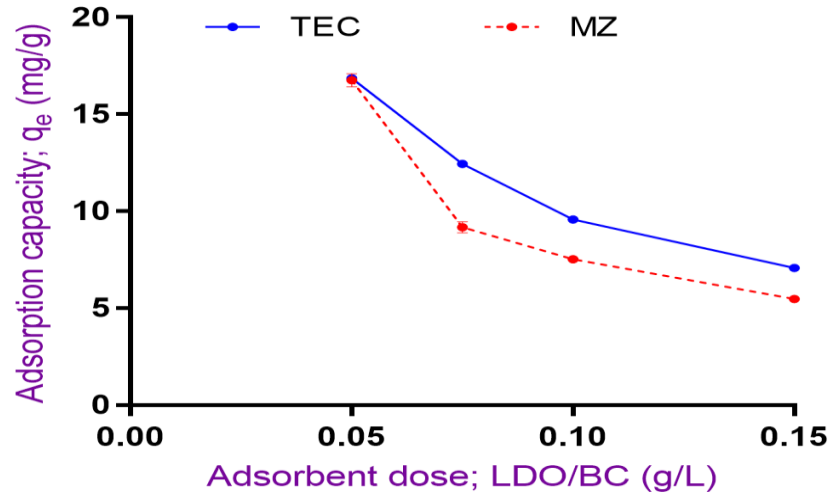


Figure 14: Effect of dosage of adsorbent on the removal of TEC and MEZ

4.2.3 Effect of Initial Antibiotic Solution with Time

The effect of initial TEC and MEZ concentration was examined simultaneously with per-determine time as shown in Figure 15 a-b; respectively. Overall, the adsorption process incremented as the initial concentration changed from 20 to 80 mg/L in both antibiotic systems and continued gradually increases with the time until it reached an optimum level at 360 min for TEC (34.14 mg/g; 80 mg/L) and at 30 min for MEZ (52.63 mg/g; 80 mg/L). The initial rapid adsorption is attributed to the presence of many unoccupied adsorption sites which later become occupied as the concentration gradient increases while the adsorbent dosage remained constant.

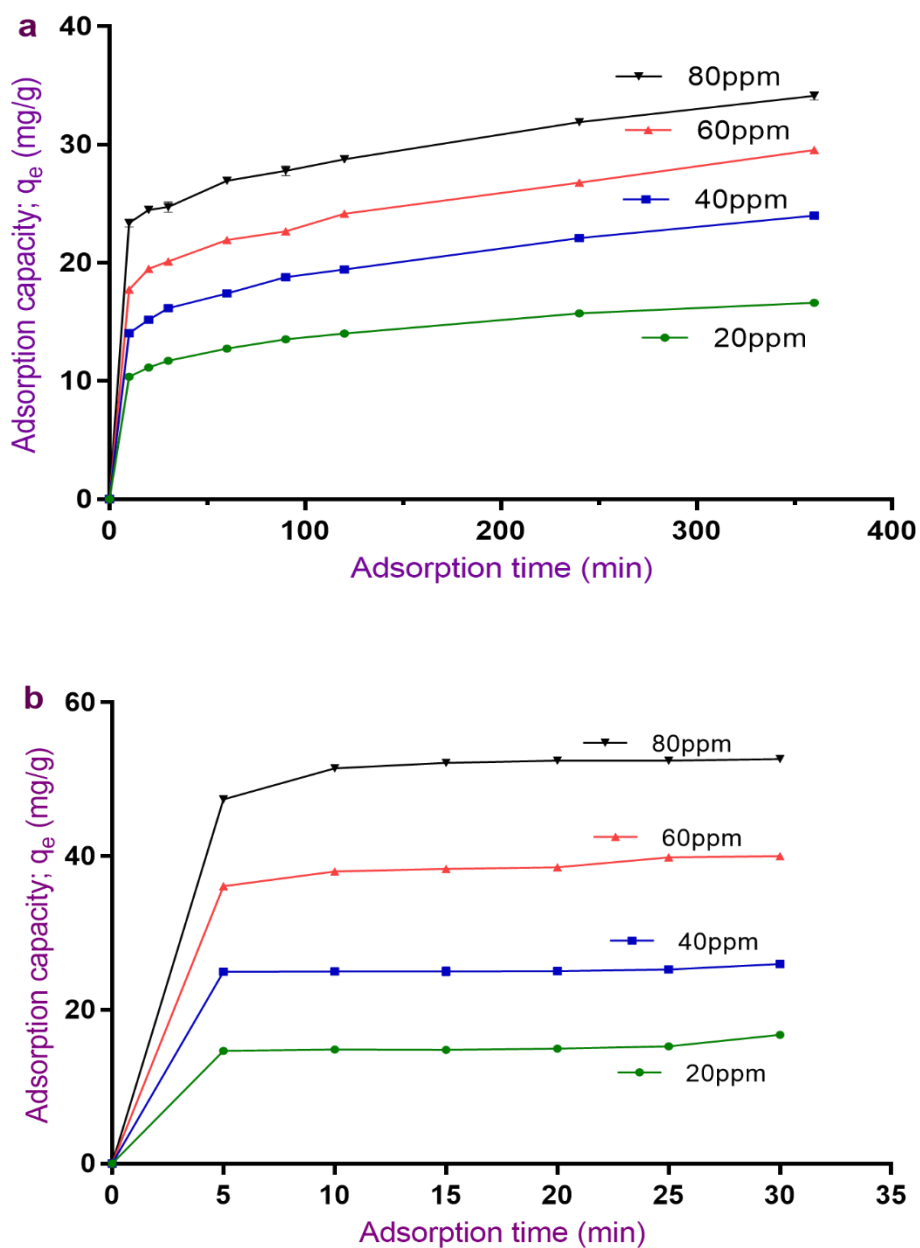


Figure 15: Effect of initial antibiotic concentration on the removal of (a) TEC and (b) MEZ onto MnFe LDO/BC

4.2.4 Effect of Temperature

The impact of reaction temperature was examined within four degrees of temperatures (20, 35, 45, and 55°C) as shown in the Figure 16 for both TEC and MEZ adsorption. Evidently, the adsorption capacity of the adsorbent decreased as the solution temperature changed from 20°C to 55°C for both pollutants. The amount of TEC adsorbed per unit mass declined obviously from 19.45 mg/g to 11.23 mg/g as

the temperature change from 20°C to 55°C, and the same trend was observed in MEZ uptake but slightly decreased from 16.76 mg/g to 15.16 mg/g at the same temperatures. These results indicate that the adsorption of TEC and MEZ unfavourable at high temperature.

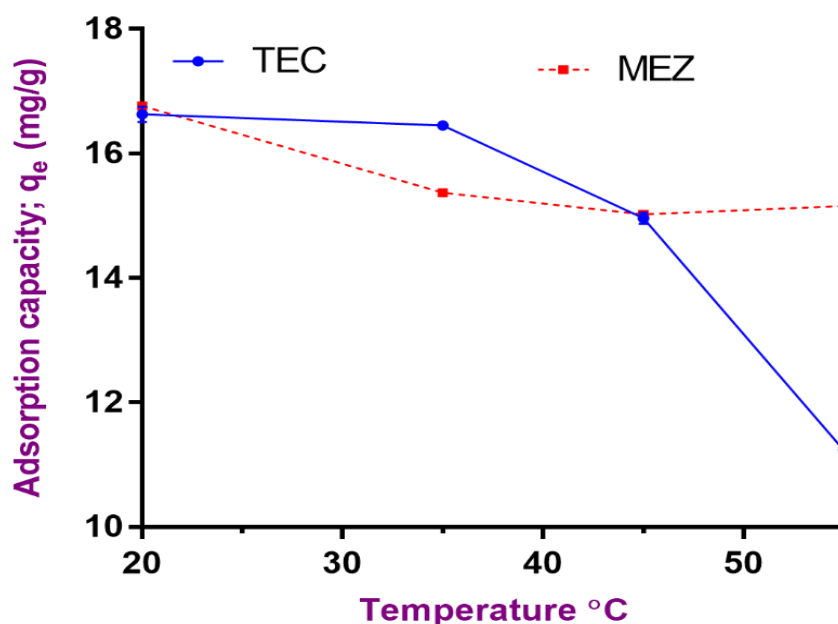


Figure 16: Effect of temperature on both antibiotic systems

4.2.5 Comparison of Performance of MnFe LDO/BC for TEC and MEZ

Removal

Table 6: Comparison of monolayer adsorption capacities of TEC

Adsorbent	pH	T(K)	qm (mg/g)	Ref.	Trend
MnFe LDO/BC	3	293	38.31	This work	TEC adsorption extremely depends on the solution pH, unfavourable at high temperature. It based on biochar- π - π -TEC interaction and/or cation exchange between the LDO and cationic TEC species
Layered non-swelling clay mineral illite (IMt-2)	5-6	-	32	Chen et al. 2012	The adsorption results show that it is on dependent on the solution pH and the ionic strength.

Acid bio-char	ambient pH	303	23.26	Liu et al., 2012	pH is an important factor impacting the TEC adsorption by electrostatic attraction. The adsorption of TEC on the bio-chars is dependent on both monolayer physical adsorption process, and some chemical interactions.
Nano cellulose	5	318	7.73	Rathod et al. 2015	The kinetics results best fitted with the double exponential models and pseudo-second order
Silica oxide	7	239	5.87	Brigante and Schulz 2011	TEC adsorption was favorable at all studied cases with a heterogeneous energy of adsorbent active sites.

Table 7: Compression of monolayer adsorption capacities of MEZ

Adsorbent	pH	T(K)	qm (mg/g)	Ref.	Trend
MnFe LDO/BC	5	293	40.82	This work	The MEZ adsorption can occur via electrostatic attraction between anionic MEZ and MnFe-LDO/BC+, unfavourable at high temperature.
Light-weight expanded clay aggregates (LECA)	7	298.0	56.31	Kalhari et al., 2017	The MEZ molecules adsorbed by physical adsorption on the adsorbent, and it's removal decreased in the presence of foreign ions like CO ₃ ²⁻ , NO ₃ ⁻ .
Siris seed pods	7	303	53.19	Ahmed and Theyda 2013	MEZ adsorption is exothermic and spontaneous under-examined conditions with best fitted by Langmuir isotherm.
Fe ₃ O ₄ -chitosan nano-adsorbent(CTS-MNPs)	3	282	49.03	Asgari et al., 2020	The adsorption is involved in a multilayer, endothermic, and spontaneous process.
Multiwalled carbon nanotubes(MWCNT)	2	289	30.6	Carrales-Alvarado et al. 2014	As carboxylic and phenolic content on the surface of carbon materials increased, the amount of MEZ adsorbed is decreased.

4.3 Kinetic and Isotherm of Adsorption Studies

4.3.1 Kinetic Study for TEC and MEZ

The four linear forms of kinetics models (Table 3 above) were applied on the experimental data to understand the adsorption rate and determine the equilibrium time (Ahmed and Theydan 2013; Martins et al., 2015). The kinetic parameters at

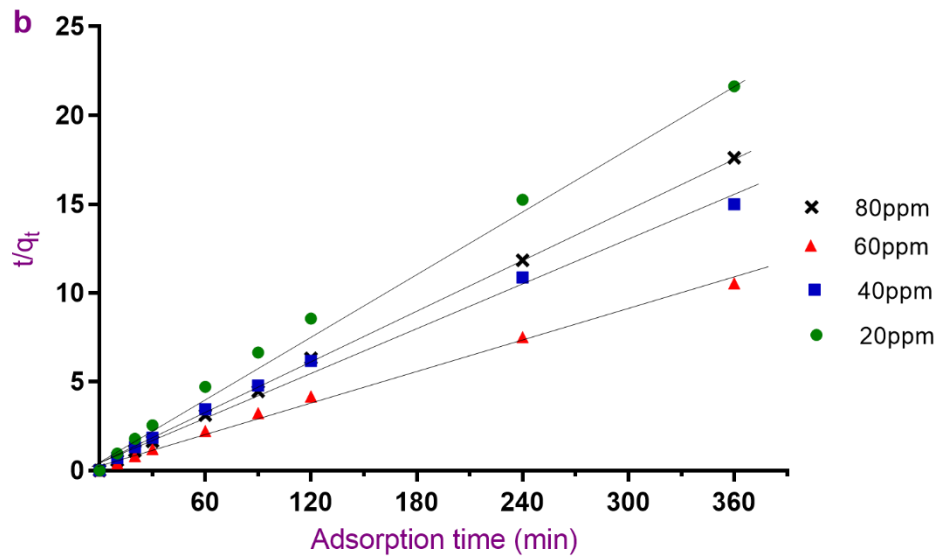
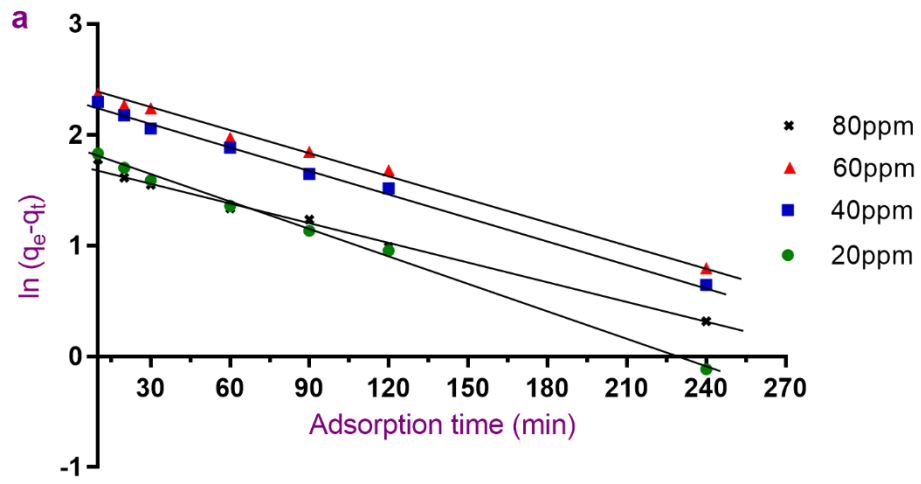
different initial antibiotic concentrations (20-80 mg/L), correlation coefficient values (R^2), and average error values were tabulated in Table 8 and 9 and the linear plots of the results are shown in the Figure 17 and 18. As shown in the table, R^2 values obtained from pseudo-second-order (P.S.O) are higher (0.989-0.999) than that of pseudo-first-order (P.F.O) (0.709-0.996) for both TEC and MEZ adsorption.

Also, the mean error function χ for P.S.O model is extremely lower than the P.F.O model which means that the q_e , calculated values are very close to q_e , experimental values in comparison with those values of P.F.O. By considering these three significant kinetic parameters, the removal of TEC and MEZ is fitted well by P.S.O model, which gives a hint that this adsorption is a chemisorption process (Shao et al 2012). Besides, the initial kinetic rate factor h was determined by multiplying the rate constant of P.S.O model K_2 in the square of q_e calculated as shown below (Ifebajo et al.,2018):

$$h = q_{e,cal}^2 \times K_2 \quad (11)$$

The rapid initial adsorption rate of TEC lies between 0.091-0.941 when compared to MEZ which lies between 0.010- 0.085.

The obtained Figure from plot q_e vs $t^{0.5}$ related to intraparticle diffusion model showed multi-linear plots as well as deviation from the origin which confirm that the intraparticle diffusion is not only the rate-limiting step other mechanisms were involved during the adsorption of both pollutants. The TEC adsorption exhibited high R^2 value ≥ 0.98 and extremely low error $\chi \leq 0.021$.



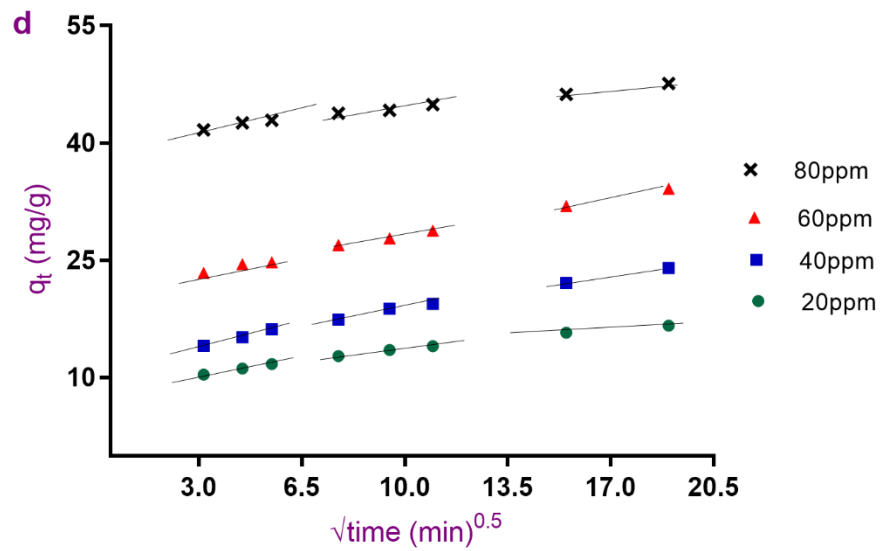
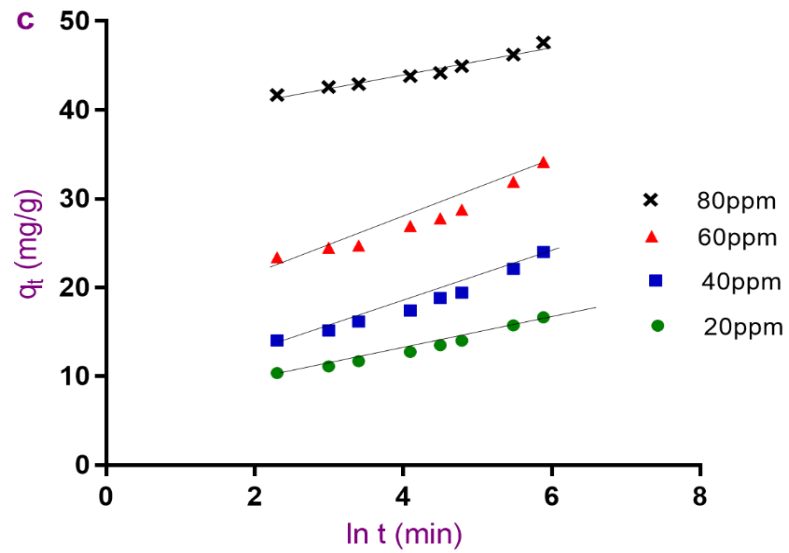
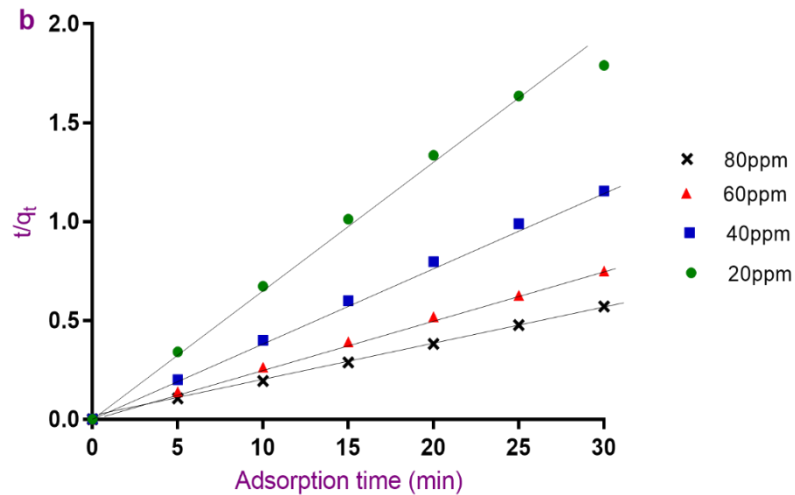


Figure 17: First order (a); second-order (b); Elovich (c); and Weber-Morris kinetic models of TEC removal



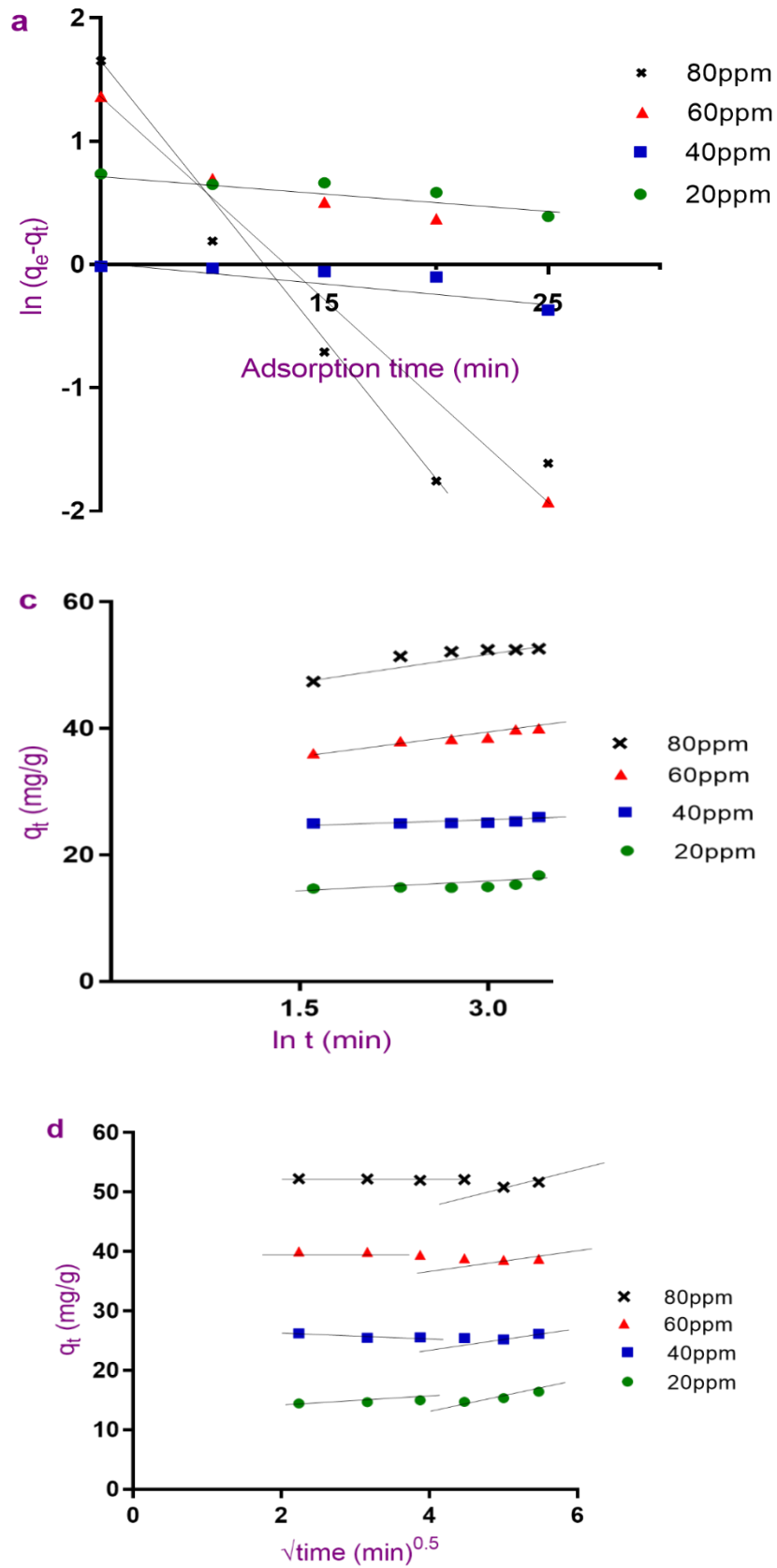


Figure 18: First order (a); second-order (b); Elovich (c); and Weber-Morris kinetic models of MEZ removal

Table 8: Kinetic parameters of TEC removal by MnFe LDO/BC at 295.15K

Kinetic models	Equations	Parameters	Conc. (mg/L)			
			20	40	60	80
		$q_{e, \text{expt.}} \text{ (mg/g)}$	16.6	24.0	34.1	47.6
Pseudo-second-order	$\frac{t}{q_e} = \frac{1}{k_2 q_e^2} + \frac{t}{q_e}$	$k_2 \text{ (g/mg min)}$	0.003	0.001	0.0003	4.12E-5
		$q_{e, \text{cal.}} \text{ (mg/g)}$	17.0	24.6	34.6	47.6
		Δq_t	0.41	0.57	0.46	0.01
		R^2	0.997	0.994	0.996	0.999
		χ	0.02	0.02	0.01	0.0003
		$h \text{ mg/g min}$	0.941	0.785	0.407	0.091
Pseudo-first-order	$\ln(q_e - q_t) = \ln q_e - k_1 t$	$K_1 \text{ (1/min)}$	0.008	0.007	0.007	0.006
		$q_{e, \text{cal.}} \text{ (mg/g)}$	6.43	10.10	11.35	5.78
		Δq_t	10.2	13.9	22.8	41.8
		R^2	0.989	0.996	0.995	0.991
		χ	1.59	1.38	2.007	7.24
Elovich	$q_t = \alpha + \beta \ln t$	$\alpha \text{ (mg/g min)}$	5.88	7.01	13.52	37.11
		$\beta \text{ (g/mg)}$	1.76	2.72	3.35	1.68
		Δq_t	19.7	0.97	0.93	0.59
		R^2	0.980	0.967	0.960	0.953
		χ	0.86	0.04	0.03	0.01
Weber-Morris intra-particle diffusion	$q_t = k_p t^{1/2} + C$	$C \text{ (g/mg)}$	9.49	12.55	21.32	40.88
		$K_p \text{ (mg/g min)}$	0.39	0.62	0.68	0.35
		Δq_t	0.36	0.26	0.10	0.005
		R^2	0.987	0.994	0.997	0.992
		χ	0.021	0.0106	0.0030	0.0001

Table 9: Kinetic parameters of MEZ removal by MnFe LDO/BC at 295.15K

Kinetic models	Equations	Parameters	Conc. (mg/L)			
			20	40	60	80
		$q_{e, \text{expt.}} \text{ (mg/g)}$	16.8	26.0	40.0	52.6
Pseudo-second-order	$\frac{t}{q_e} = \frac{1}{k_2 q_e^2} + \frac{t}{q_e}$	$k_2 \text{ (g/mg min)}$	0.0003	2.4E-5	1.2E-5	3.3E-6
		$q_{e, \text{cal.}} \text{ (mg/g)}$	16.8	26.0	41.0	53.8
		Δq_t	0.0	0.0	1.0	1.2
		R^2	0.989	0.999	0.999	0.999
		χ	0.0006	0.0004	0.023	0.021
		$h \text{ (mg/g min)}$	0.085	0.016	0.035	0.010
		Pseudo-first-order	$\ln(q_e - q_t) = \ln q_e - k_1 t$	$K_1 \text{ (1/min)}$	0.015	0.016
$q_{e, \text{cal.}} \text{ (mg/g)}$	2.30			1.13	9.73	8.14
Δq_t	14.5			24.9	30.3	5.45
R^2	0.827			0.709	0.764	0.903
χ	6.3			22.08	3.11	44.46
Elovich	$q_t = \alpha + \beta \ln t$	$\alpha \text{ (mg/g min)}$	13.04	24.18	32.79	43.15
		$\beta \text{ (g/mg)}$	0.811	0.388	2.10	3.13
		Δq_t	0.97	0.48	0.07	1.15
		R^2	0.474	0.452	0.947	0.857
		χ	0.06	0.02	0.002	0.021
Weber-Morris intra-particle	$q_t = k_p t^{1/2} + C$	$C \text{ (g/mg)}$	13.25	24.27	33.83	45.67
		$K_p \text{ (mg/g min)}$	0.49	0.24	1.15	1.42
		Δq_t	0.83	0.41	3.96	0.83

diffusion	R^2	0.573	0.557	0.936	0.724
	χ	0.05	0.02	0.09	0.02

4.3.2 Isotherm Adsorption Study for TEC and MEZ

Adsorption isotherm is very important as it gives insights about how adsorbates interact with adsorbents in the solution. The experimental data were fitted to four different isotherm models and the most suitable model was selected considering both the correlation coefficient (R^2) and the error functions (χ and Δq_e). As shown in Table 10, Freundlich model exhibits comparable R^2 values of 0.99 for TEC and 0.89 for MEZ with very high Δq_e and χ . Note that the Langmuir model exhibited high correlation coefficients closer to unity with the lowest error functions; hence, the adsorption mechanism is well fitted a monolayer mechanism. This is consistent with Redlich-Peterson isotherm model since the linear constant “g” closer to 1.0 (Oladipo et al., 2019). Furthermore, the magnitudes of mean sorption energy E that calculated from D-R isotherm model were less than 8 kJ/mol for both antibiotic adsorption process which is indicative of a physical adsorption process.

Table 10: Adsorption isotherm parameters of TEC and MEZ onto MnFe LDO/BC

Isotherm models	Linear plots	Parameters	TEC	MEZ
Freundlich	$\log q_e$ vs. $\log C_e$	k_F (mg/g)(mg/L) ⁿ	11.8	9.87
		n	0.27	0.43
		Δq_e	20.7	4.25
		R^2	0.99	0.89
		χ	1.53	0.12
Langmuir	$\frac{1}{q_e}$ vs. $\frac{1}{C_e}$	q_m (mg/g)	38.3	40.8
		b (L/mg)	0.15	0.21
		Δq_e	4.17	0.81
		R^2	0.985	0.899
		χ	0.11	0.02
Temkin	q_e vs. $\ln C_e$	B_1 (KJ/mol)	6.55	10.9
		K_T (L/mg)	3.32	1.31
		Δq_e	17.5	25.1
		R^2	0.959	0.805
		χ	1.1	1.7
Redlich-Peterson	$\frac{C_e}{q_e}$ vs. C_e	K_{rp} (L/g)	5.88	6.14
		α_{rp} (L/mg) ^g	0.15	0.12
		Δq_e	4.59	0.35

		g	0.99	0.94
		R ²	0.985	0.799
		χ	0.12	0.009
Dubinin– Radushkevich	ln q _e vs. ε ²	q _m (mg/g)	29.2	39.5
		k _{D-R} (mol ² /KJ ²)	1.41	2.00
		E (KJ/mol)	0.600	0.500
		Δq _e	0.12	0.61
		R ²	0.794	0.703
		χ	0.004	0.016

4.3.3 Thermodynamic Studies of TEC and MEZ Removal by MnFe LDO/BC

The influence of the variation of solution temperature on the adsorption of TEC and MEZ by MnFe LDO/BC composite was examined. The following thermodynamic parameters; Gibb's free energy (ΔG°), Enthalpy (ΔH°), and entropy (ΔS°) were calculated to further explain the adsorption mechanisms. The distribution coefficient K_d was calculated as the ratio of adsorbed amount q_e of adsorbate to the equilibrium concentration C_e (Eq. 12), the ΔG° was calculated using Eq. 13. Finally, ΔH° and ΔS° were obtained from the slope and intercept of the plot of ln K_d vs 1/T (K) as expressed in Eq. 15.

$$K_d = \frac{q_e}{C_e} \quad (12)$$

$$\Delta G^\circ = -RT \ln K_d \quad (13)$$

$$\Delta G^\circ = -T\Delta S^\circ + \Delta H^\circ \quad (14)$$

Van't Hoff's equation;

$$\ln K_d = \frac{\Delta S^\circ}{T} - \frac{\Delta H^\circ}{RT} \quad (15)$$

where;

R is the universal gas constant = 8.314 J/mol K, and the temperature T was in the range of 293.15-328.15 K).

Table 11 for both adsorption systems, shows that the values of ΔG° were negative at all studied temperatures which confirms that the adsorption of TEC and MEZ onto MnFe LDO/BC composite was spontaneous in nature; also it was physisorption process because of the values fall between 20 and 0 kJ/mol (Zhang et al., 2009). The values of ΔH° and ΔS° are negative, which confirms that the adsorption processes were exothermic with less degree of randomness of the adsorbate at the interface of the adsorbent during adsorption process.

Table 11: Thermodynamic parameters of TEC and MEZ removal by MnFe LDO/BC

TEC				
T(K)	ΔG°(kJ/mol)	ΔS°(J/mol K)	ΔH°(kJ/mol)	R²
295.15	-3.90	-84.3	-29.1	0.7689
308.15	-3.49			
318.15	-2.89			
328.15	-0.68			
MEZ				
T (K)	ΔG°(kJ/mol)	ΔS° (J/mol K)	ΔH° (kJ/mol)	R²
295.15	-4.01	-28.0	-12.0	0.8012
308.15	-3.07			
318.15	-2.92			
328.15	-3.11			

4.4 Photocatalytic Activities Results

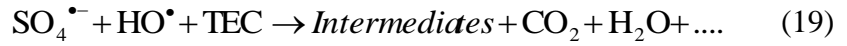
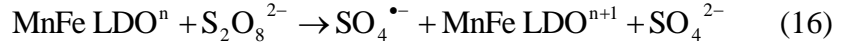
4.4.1 Evaluation of Photocatalyst Performance of MnFe LDO/BC for Antibiotic Degradation

The performance of the MnFe LDO/BC for degradation of TEC and MEZ antibiotic was investigated and compared under different degradation scenarios/systems as presented in the Figure 19 a-b. In these systems, the pH of the solution was adjusted to pH 3 and 25 mg of MnFe LDO/BC and 5 mM of H₂O₂/ K₂S₂O₈ oxidants were used.

For the TEC solution, and with the blank system, no degradation was recorded when the solution was agitated for 300 min without UV-light and catalyst (used as the control blank test). About 37% of TEC degradation was observed in the first 30 min of UV light irradiation without the catalyst (photolysis) system of shining the light. No further degradation was observed even after 300 min. ~20% of TEC was degraded in H₂O₂ system after 300 min of degradation reaction time. The low degradation efficiency here might be related to the fact that hydrogen peroxide generates low hydroxide radicals ($\cdot\text{OH}/\text{H}_2\text{O}$, $E^\circ = 2.38 - 2.72$ eV) in acidic solution (Hazime et al. 2014; Essawy et al. 2020). While in the presence of K₂S₂O₈, 57.5% of TEC was degraded after 120 min and increased to 89.7% after 300 min of UV irradiation. It is worthy to mention that K₂S₂O₈ can be activated by the UV-light in a wide range of pH to generate $\text{SO}_4^{\cdot-}/\text{SO}_4^{2-}$, $E^\circ = 2.5 - 3.1$ eV (Lin et al., 2016). From Figure 18 a, the UV+K₂S₂O₈ system exhibited higher degradation efficiency than UV+H₂O₂; this could be due to the higher density and selectivity of the generated $\text{SO}_4^{\cdot-}$ species at pH 3. When the MnFe LDO/BC was used with UV-light alone, the TEC degradation efficiency was noticed to be 1.3 times higher than in the UV+K₂S₂O₈ system at 120 min, and reached 92% after 300 min.

The MnFe LDO/ BC/ UV+K₂S₂O₈ system exhibited the highest degradation efficiency of the TEC. It reached 93.4% after 120 min and increased to 97.3% after 180 min. This is attributed to synergistic effects of the generated radicals and appropriate structure of the catalyst. Specifically, the S₂O₈²⁻ ions could be activated by electron transfer from the LDO transition metals (MnFe) (Zhu et al., 2020) and also by the UV light (Lin et al. 2016) to produce $\cdot\text{SO}_4^-$ radicals which then reacts

with H₂O molecules to generate extra [•]OH to cooperatively degrade TEC according to Eqs. (16) – (19):



Similar observation trends were recorded for MEZ degradation using the same seniors above. As shown in Figure 19 b, the MEZ degradation rate by MnFe LDO/BC/UV+H₂O₂ appeared to be the fastest, it reached 90% after 30 min and increased gradually to ~100% after 240 min of UV-irradiation. This could be attributed to that the MEZ degradation followed pseudo-first-order kinetics. The calculated k_{app} value for MEZ degradation in MnFe LDO/BC/UV+H₂O₂ was 0.1180 1/min which was 2.59 and 1.32 faster than LDO/BC/UV and MnFe LDO/BC/K₂S₂O₈/UV systems, respectively.

Overall, this study revealed that oxidant (H₂O₂ and K₂S₂O₈) or UV alone was inefficient in the degradation of TEC and MEZ; their removal efficiencies were ≤ 22% after 300 min which were comparatively lower to 90% achieved by MnFe/LDO/BC/UV. Therefore, MnFe/LDO/BC is an active light-driven photocatalyst for the remediation of emerging pseudo refractory pollutants from wastewater.

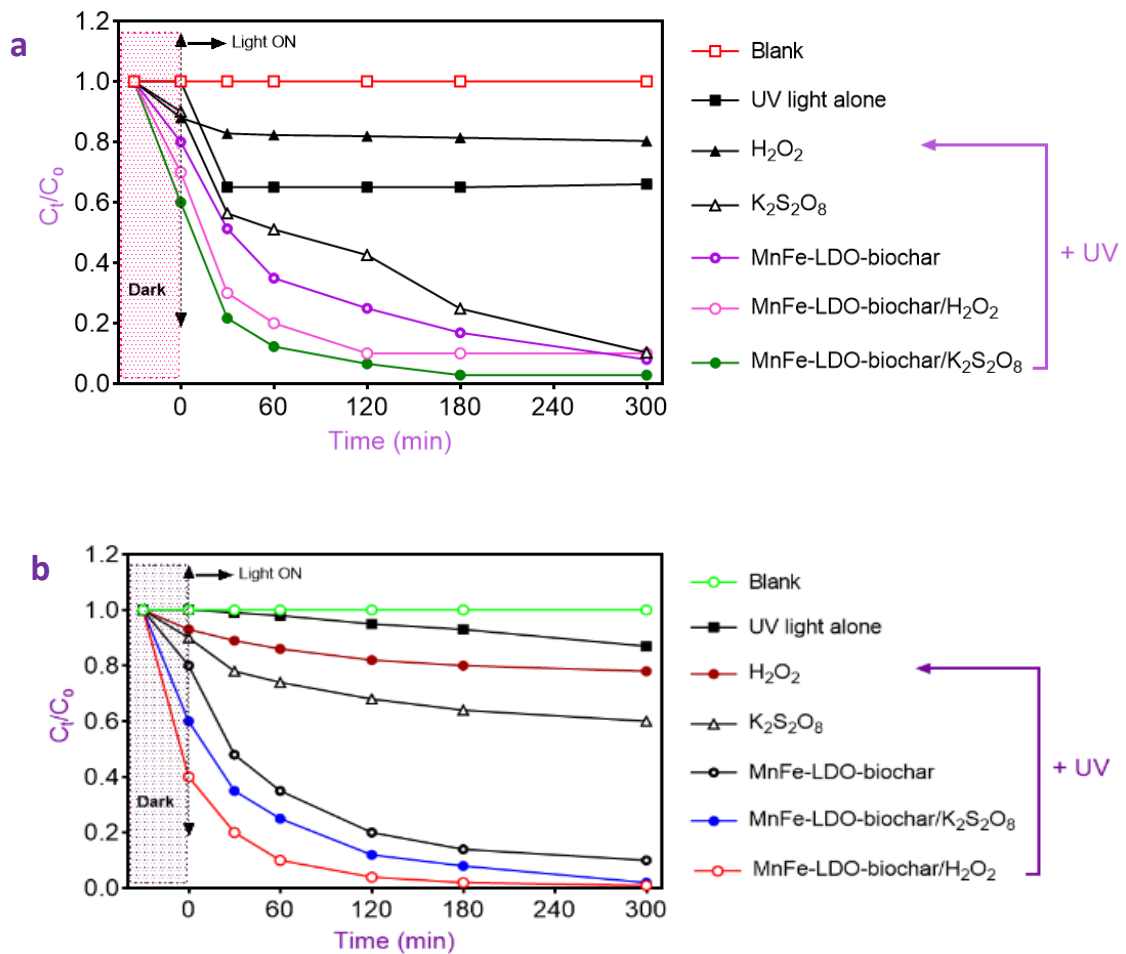


Figure 19: Comparative investigation of (a) TEC (b) MEZ degradation under different systems

4.4.2 Effect of MnFe LDO/BC Dosage

The influence of photocatalyst dosage on the photodegradation process of TEC and MEZ was examined using three different amounts of MnFe LDO/BC (0.025 g, 0.05 g, and 0.075 g); without any oxidants, and the results are shown in Figure 20 a-b, respectively. The degradation efficiency of TEC and MEZ increased from 73.5% to 90.2%, and from 80% to 97% after 120 min of irradiation time, as the composite dosage increased from 25 mg to 50 mg, respectively. As the contact time exceeded 300 min, gradual increments of the oxidation efficiency of the photocatalyst were recorded and reached 98.9% for TEC and MEZ.

The increasing trend is attributed to the increasing active sites on the surface of the catalyst with increases in the dosage which subsequently increased the quantity of photogenerated carriers or other radical oxygen species ROS ($\cdot\text{O}_2^-$ or $\cdot\text{OH}$) (Ifebajo et al., 2020). No considerable enhancement in the degradation efficiency was observed when the catalyst dosage was increase to 75 mg in both antibiotic solutions. Due to the solution turbidity with a subsequence reducing in the light dispersion in the suspension and decreased the degradation efficiency. Therefore, 50 mg (1.0 g/L) was selected as the optimum dosage of MnFe LDO/BC catalyst for further TEC and MEZ photodegradation experiments.

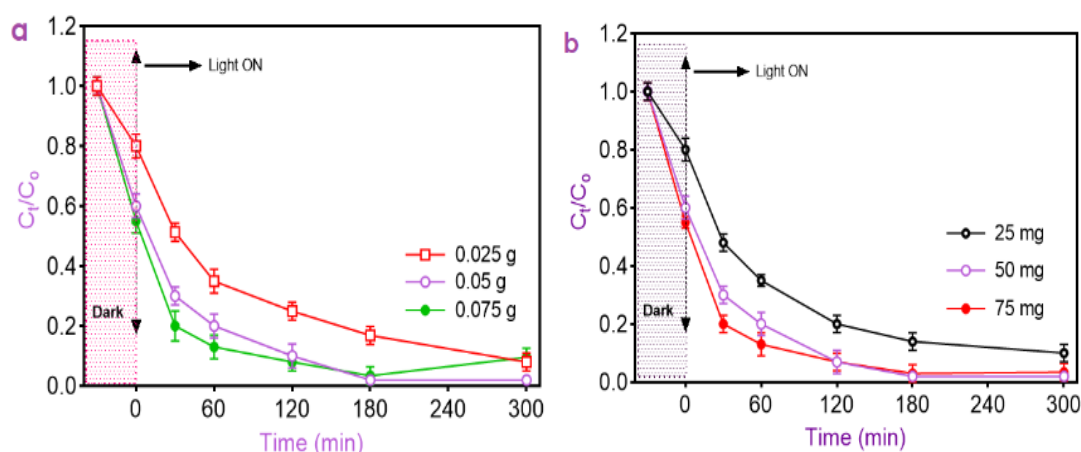


Figure 20: Effect of MnFe LDO/BC dosage on the degradation of (a) TEC, and (b) MEZ

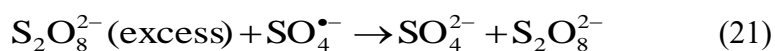
4.4.3 Effect of H_2O_2 and $\text{K}_2\text{S}_2\text{O}_8$ Oxidants Concentration

As depicted in Figure 21 a. in dark condition and when 4 mM of H_2O_2 was introduced into 20 mg/L of TEC solution containing 50 mg of the catalyst; 40% of TEC was degraded while only 12% and 10% removal was observed at 6 mM and 8 mM respectively. After 30 min of UV irradiation, the TEC degradation doubled and reached 97.9% after 120 min in the presence of 4 mM of H_2O_2 , compared with 90.0% and 92.0% removal when the concentration of H_2O_2 were 6 mM and 8 mM.

Thus, 4mM was taken as the appropriate concentration of H₂O₂ for further tests. The decreasing trend in the degradation efficiency when the H₂O₂ concentration increases is likely due to scavenging effects of excess amount of H₂O₂ as presented in the Eq. 20 (Gazi et al. 2017).



The degradation followed a similar pattern in the presence of K₂S₂O₈ as shown in the Figure 21 b and d. The optimal K₂S₂O₈ concentration of 6 mM was selected as the degradation reached 98% after 120 min which is remarkably higher than that of other concentrations. The lower degradation efficiency observed beyond 6 mM of K₂S₂O₈ might be due to the competitive consumption of the free radicals by reacting with the radical to produce relatively weaker oxidant ($\cdot\text{SO}_5^-$, 1.1 eV) (Li et al., 2020), or by the scavenging effect as represented in Eqs. 21 and 22 (Hong et al., 2019):



In the case of MEZ solution, under the same conditions of catalyst dosage and antibiotic concentration; the MEZ degradation increased gradually from 60%, 67% to 70% when the H₂O₂ concentration was changed from 4, 6 to 8 mM in the dark, respectively. After 60 min of UV exposure, the degradation increased as the concentration of the oxidant increased from 4 mM to 6 mM and reached 90% and 97.8%, due to increase the density of $\cdot\text{OH}$ radicals. However, no significant increases in the degradation rate when the H₂O₂ concentration increased to 8 mM, but it declined to 92% during first 60 min UV light irradiation (Figure 21 c). Also, when the K₂S₂O₈ concentration varied from 4 mM to 6 mM, the MEZ degradation increased from 75% to 90% after 60 min of UV irradiation, while, it decreased to 87% when the K₂S₂O₈ concentration increased to 8 mM at 60 min (Figure 21 d).

Therefore, 6 mM was chosen as the appropriate H_2O_2 and $\text{K}_2\text{S}_2\text{O}_8$ concentration for further experiments in this work.

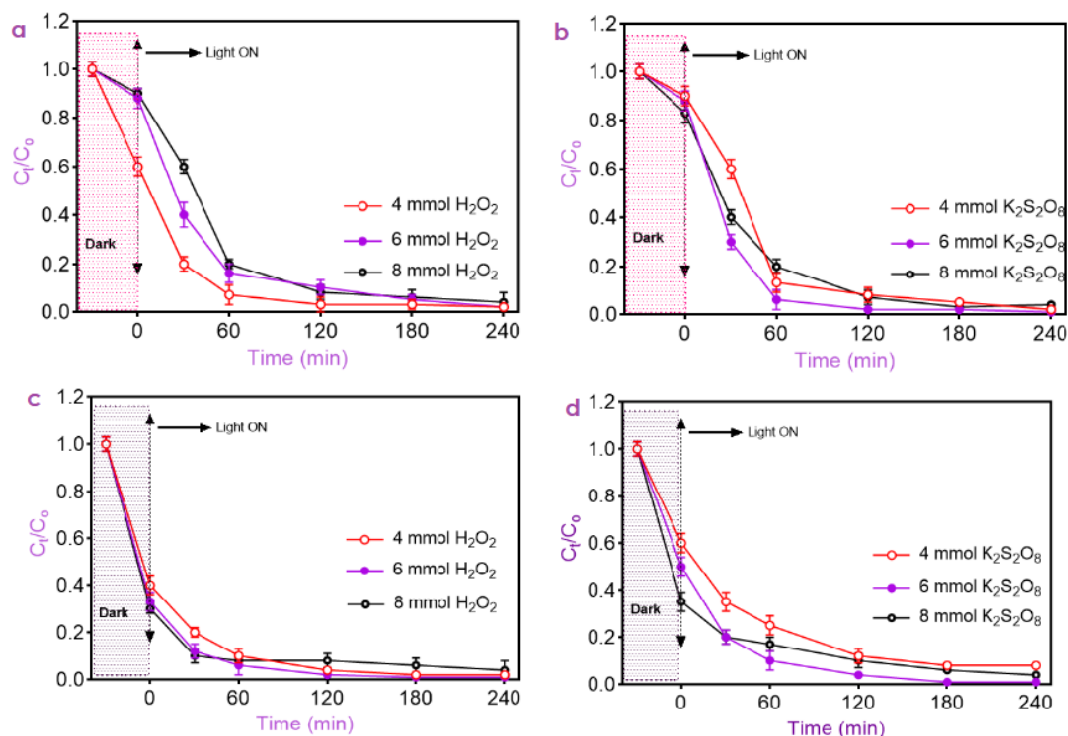


Figure 21: Effect of H_2O_2 and $\text{K}_2\text{S}_2\text{O}_8$ oxidants concentration on (a-b) TEC; and (c-d) MEZ degradation

4.4.4 Performance Under Optimized Conditions and Radical Trapping Test

The Figure 22 a, and c demonstrated the performance of the photocatalyst under the optimum conditions. In the dark, the TEC and MEZ removal reached 50, 26, 59, 60, and 22%; and 50, 26, 38, 40, and 20% by biochar, MnFe LDO alone, MnFe LDO/BC, MnFe LDO/BC/ H_2O_2 , and MnFe LDO/BC/ $\text{K}_2\text{S}_2\text{O}_8$, respectively. Obviously, after 120 min of UV irradiation, no remarkable increases in the biochar degradation efficiency, due to lack of its photocatalytic ability. On the other hand, MnFe LDO alone exhibited 91%, and MnFe LDO/BC/ H_2O_2 or MnFe LDO/BC/ $\text{K}_2\text{S}_2\text{O}_8$ reached ~98%. The prepared MnFe LDO/BC outperformed many other catalysts for TEC and MEZ degradation. For instance, the optimum TEC

degradation was 85% in 150 min when 10 mg MIL-100(Fe)@Fe₃O₄/carbon aerogel was utilized under visible light irradiation of xenon arc lamp (150 W) (Rasheed et al., 2018). Aram and other authors reported 70% as the optimum MEZ degradation in 120 min using 2 g/L Urea/TiO₂/ZnFe₂O₄/Clinoptilolite under visible-light irradiation and ozone injection (Aram et al., 2020).

To identify active species that participated during the photodegradation of TEC and MEZ, 5 mM of 1,4-benzoquinone (BQ), t-butyl alcohol (t-BuOH), sodium oxalate (Na-Ox) were introduced separately into the antibiotic solutions for capturing reactive oxygen species (ROS); superoxide radicals ($\cdot\text{O}_2^-$), hydroxyl radicals ($\cdot\text{OH}$), sulfate radicals ($\text{SO}_4^{\cdot-}$), and holes (h^+), respectively. Clearly from the Figure 22 b and d, the presence of the t-BuOH remarkably suppressed the degradation of TEC and MEZ. The degradation of TEC was inhibited by t-BuOH and resulted in 40.3% and ~60.1% in the presence of H₂O₂ and K₂S₂O₈, respectively. Similar to that, the degradation of MEZ decreased to 30.3% and ~50.1% from 98% in the presence of H₂O₂ and K₂S₂O₈ due to the addition of t-BuOH, respectively. Therefore, both $\cdot\text{OH}$ and $\text{SO}_4^{\cdot-}$ radicals contributed majorly during the photodegradation reactions while other radicals partially participated during degradation process. Notably, no significant reduction in the degradation of both antibiotics when BQ was used; only ~7.3% and 28.0% decline in TEC and MEZ degradation were recorded relative to the system without the scavenger. This suggests that $\cdot\text{O}_2^-$ contributed slightly during the degradation. On the contrary, according to the report by He et al., 2002; the degradation rate of TEC was strongly inhibited by Na-Ox and BQ, indicating that $\cdot\text{O}_2^-$ and h^+ contributed majorly in the photocatalytic process of TEC. Bashiri et al.,

2020 studied the photocatalytic degradation of MEZ over $\text{Fe}_3\text{O}_4/\text{rGO}/\text{TiO}_2$ and evaluated the degradation process in the presence of these scavengers. The results showed that the removal efficiency of MEZ reduced to 31.1% from 96.0% due to the addition of quenching agent BQ, while it reached 69.2% and 84.5% when *t*-BuOH and ammonium oxalate were used, respectively. This confirmed that the superoxide radicals $\cdot\text{O}_2^-$ were the key active species followed by $\cdot\text{OH}$, while the photo-induced holes h^+ contributed lightly during the degradation of the MEZ.

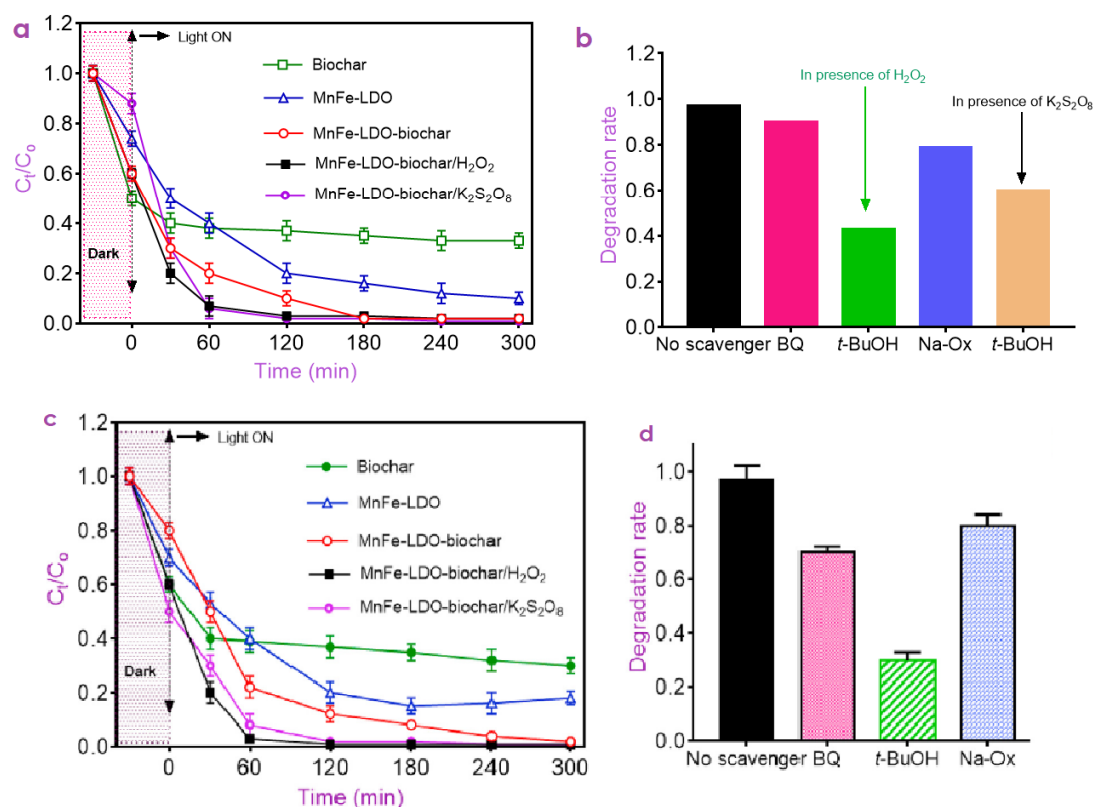


Figure 22: Performance under optimized conditions and radical trapping test of (a-b) TEC; and (c-d) MEZ degradation (in the presence of 6mM of $\text{H}_2\text{O}_2/\text{K}_2\text{S}_2\text{O}_8$)

4.4.5 Degradation Kinetics of TEC and MEZ Under Various Photo-degradation Conditions

The degradation rate was fitted with first-order kinetic equation and obtained parameters are presented in Table 12 and 13. The tables revealed that the TEC and

MEZ data showed excellent linearity with R^2 values in the range of 0.969-0.998 within identified stages. The stage I of the direct photolysis of TEC showed a rapid degradation rate (35.6%) with very low degradation rate constant ($K_{app}=0.0109$ 1/min). The apparent rate constants ($K_{app}=0.0456$ 1/min; stage I, and $K_{app}=0.0268$ 1/min; stage II) presented by MnFe LDO/BC/ $K_2S_2O_8$ were comparable to that once of MnFe LDO/BC/ H_2O_2 but extremely higher than the other degradation systems. each other but extremely higher than the other degradation systems. Thus, $SO_4^{\cdot-}$ is more selective species to TEC degradation either by the hydrogen abstraction, addition on the double bond, or electron transfer in the broad pH range (Hazime et al., 2014).

For direct photolysis of MEZ degradation exhibited the lower rate degradation (5.0%) with very slow rate constant at stage I ($K_{app}=0.0094$ 1/min), also, the total energy consumed in the photolytic degradation after 300 min was comparatively high; 69.85 KWh/ m^3 . Notably, the apparent rate constant ($K_{app}=0.226$ 1/min; stage I, and $K_{app}=0.0868$ 1/min; stage II) presented by MnFe LDO/BC/ H_2O_2 were comparable to that once of MnFe LDO/BC/ $K_2S_2O_8$ but extremely higher than the other degradation systems with the lowest energy cost (0.38-0.51\$). Additionally, the energy consumed by MnFe LDO/BC/ H_2O_2 +UV to achieve ~98% MEZ degradation within 60 min light irradiation is remarkably lower (7.56 KWh/ m^3 , 9 W UV lamp) than 32.09 KWh/ m^3 to achieve 90% of MEZ degradation in 90 min using UV/BiOI-MWCNTs (30 W UV) (Balarak et al. 2019).

Table 12: Degradation kinetics of TEC and correlation coefficients (R^2) under different processes

Process	Stage (time)	Regression equation	k_{app} (min^{-1})	η (%)
---------	--------------	---------------------	-----------------------------	---------------

Photolysis	I (0–30 min)	$Y = -0.918x + 0.023$ ($R^2 = 0.989$)	0.0109	35.6
	II (30–300 min)	$Y = -0.622x + 0.087$ ($R^2 = 0.975$)	0.0081	37.1
MnFe LDO/BC	I (0–30 min)	$Y = -1.032x + 0.088$ ($R^2 = 0.985$)	0.0358	70.2
	II (30–60 min)	$Y = -2.008x + 0.064$ ($R^2 = 0.979$)	0.0291	80.4
	III (120–300 min)	$Y = -2.562x + 0.019$ ($R^2 = 0.995$)	0.0158	97.9
MnFe LDO/BC/H ₂ O ₂	I (0–60 min)	$Y = -2.898x + 0.059$ ($R^2 = 0.997$)	0.0434	93.3
	II (60–240 min)	$Y = -1.003x + 0.077$ ($R^2 = 0.996$)	0.0262	97.9
MnFe LDO/BC/K ₂ S ₂ O ₈	I (0–60 min)	$Y = -2.021x + 0.016$ ($R^2 = 0.997$)	0.0456	94.5
	II (60–240 min)	$Y = -1.898x + 0.072$ ($R^2 = 0.998$)	0.0268	98.1
^a ZIF-8@TiO ₂	120 min	–	0.0340	90
^b SnO ₂	135 min	0.989	0.0127	77.1
^c Ag ₂ O-Ag/LDO ₅	90 min	–	0.0242	92
^d TiO ₂ -P25	II (30–120 min)	0.998	0.0200	35.7
^e TiO ₂ @Mg-Al LDH	120 min	0.997	0.0200	90
^f Graphene oxide/ZnO	100 min	–	0.0140	74
^g Al-doped BiOCl	60 min	–	–	91.1

Optimum conditions: Initial TC concentration: 20 mg L⁻¹; catalyst dosage: 50 mg; contact time 0–300 min; UV lamp (9 W); 5 mM oxidant (pH 3 for K₂S₂O₈ and pH 7 for H₂O₂).

a: 60 mg catalyst; 300 W Xe lamp; TC (100 mg L⁻¹); Li et al. 2020b.

b: 50 mg catalyst; 9 W LED bulb; TC (20 mg L⁻¹); ultrasound (40 kHz, 50 W) Yashas et al. 2020

c: 1 g L⁻¹ catalyst 500 W xenon lamp; TC (40 mg L⁻¹); Shen et al. 2020.

d: 0.2 g L⁻¹ TiO₂-P25; 300 W xenon lamp (UV, 350 nm); TC (10 mg L⁻¹); Wu et al. 2020.

e: 0.2 g L⁻¹ TiO₂@Mg-Al LDH; 0–500 W ultraviolet lamp (UV); TC (20 mg L⁻¹); Song et al. 2020.

f: 50 mg Graphene oxide/ZnO; simulated light irradiation; TC (50 mg L⁻¹, 50 mL) Qiao et al. 2020.

g: 20 mg Al-doped BiOCl; 300 W xenon lamp; TC (100 mg L⁻¹, 50 mL) Zhang et al. 2020.

Table 13: Degradation kinetics of MEZ and correlation coefficients (R^2) under different processes

Process	Stage (time)	k_{app} (min ⁻¹)	R^2	^a MSE	η (%)	E (kWh m ⁻³)	^b Cos t (\$)
Photolysis	I (0–120 min)	0.0094	0.979	0.211	5.0	98.67	4.93
	II (120–300 min)	0.0136	0.989	0.342	13	69.85	3.49
MnFe LDO/BC	I (0–60 min)	0.0997	0.969	0.189	78	27.89	1.39

	II (60–180 min)	0.0691	0.988	0.112	92	16.68	0.83
	III (180–300 min)	0.0366	0.997	0.018	98	7.98	0.40
MnFe LDO/BC/H ₂ O ₂	I (0–60 min)	0.226	0.998	0.017	97.8	7.56	0.38
	II (60–240 min)	0.0868	0.987	0.012	99	10.26	0.51
MnFe LDO/BC/K ₂ S ₂ O ₈	I (0–60 min)	0.212	0.996	0.108	92.1	11.31	0.57
	II (60–240 min)	0.0913	0.994	0.015	98.8	14.62	0.73
^c UV/BiOI–MWCNTs	90 min	0.0740	0.952	–	99.95	32.09	1.61
^d UV/TiO ₂	120 min	0.0233	–	–	99.48	–	–
^e GAC@ZnO composite	30 min	0.0074	0.946	–	83	–	–
^f N-TiO ₂ /ZnFe ₂ O ₄ /zeolite	120 min	0.0196	–	–	70	–	–

Optimum conditions: Initial MEZ concentration: 20 mg L⁻¹; catalyst dosage: 50 mg; contact time 0–300 min; UV lamp (9 W); 5 mM oxidant and pH 5.

a: mean squared error

b: Calculated using August 2020 Turkish Republic of North Cyprus energy cost =0.05\$ per kWh (1\$ ≈ 7.33 TL)

c: 0.6 g L⁻¹ BiOI–MWCNTs; 30 W UV lamp; MEZ (10 mg L⁻¹); 1 L, pH 7; Balarak et al. 2019.

d: 0.5 g L⁻¹ TiO₂; 15 W ultraviolet lamp; MEZ (80 mg L⁻¹); pH 7; 0.1 L; Farzadkia et al. 2015.

e: 2.0 g L⁻¹ catalyst dosage; pH 11, catalytic ozonation process; MZ (300 mg L⁻¹, 300 mL); Nasseh et al.2020.

f: 2.0 g L⁻¹ catalyst dosage; UV–vis (200 W, light intensity: 400 lm m⁻²); pH 5; MEZ (100 mg L⁻¹); Aram et al.2020.

4.4.6 Proposed Mechanism for TEC and MEZ Photo-degradation Study

According to the experimental results obtained under optimized conditions, radical trapping test and physicochemical characteristics of the photocatalyst; the TEC and MEZ degradation mechanism were proposed. The bandgap energy (E_g) of MnFe LDO/BC is 2.85 eV while the potentials of the valence band (VB) and conduction band (CB) were calculated accordingly (Oladipo at al., 2019; Oladipo 2018).

$$VB = \chi - E^e + 0.5E_g \quad (23)$$

$$CB = VB - E_g \quad (24)$$

The absolute electronegativity of the MnFe LDO, χ is 5.39 eV; E° is 4.5 eV and it represents the energy of free electrons on the hydrogen scale (NHE). The calculated CB and VB of MnFe LDO/BC are -0.52 eV and 2.33 eV, respectively. The hybrid catalyst offered sufficient reactive sites; in the first 30 min dark adsorption stage, both oxygen and tetracycline/metronidazole were adsorbed into the MnFe LDO/BC surface and trapped by the pores filling of the biochar and interconnected layered framework of the MnFe LDO.

As represented in Figure 23; under light irradiation, the photons excited electrons (e^-) from the valence band of the photo-active material to its CB, which resulted in the formation of holes (h^+) in the VB. Then, the photogenerated e^- at the CB can directly reduce the adsorbed oxygen into $\cdot O_2^-$ because the reduction potential of $O_2/\cdot O_2^-$ (-0.33 eV vs. NHE) is less negative than the CB potential (-0.52 eV) or can react with $S_2O_8^{2-}$ to produce the highly selective $SO_4^{\cdot-}$ radicals.

Considering the results of the radical trapping study, some of the $\cdot O_2^-$ radicals partly degraded the adsorbed TEC/MEZ or further reacted with H_2O_2 or H_2O in the system to produce $\cdot OH$ radicals which participated majorly in the degradation of the TEC/MEZ. The h^+ in the VB also contributed to the degradation of antibiotics. The VB potential (2.33 eV) is more positive than the $HO^-/\cdot OH$ (1.99 eV), hence, can generate more hole mediated $\cdot OH$ radicals. Also, the Mn and Fe ions in the surface lattice of MnFe LDO/BC can act as active sites and react with the H_2O_2 or $K_2S_2O_8$ to generate oxidant radicals, thus behaving like (Eqs. 25–27) to degrade the adsorbed TEC/ MEZ.



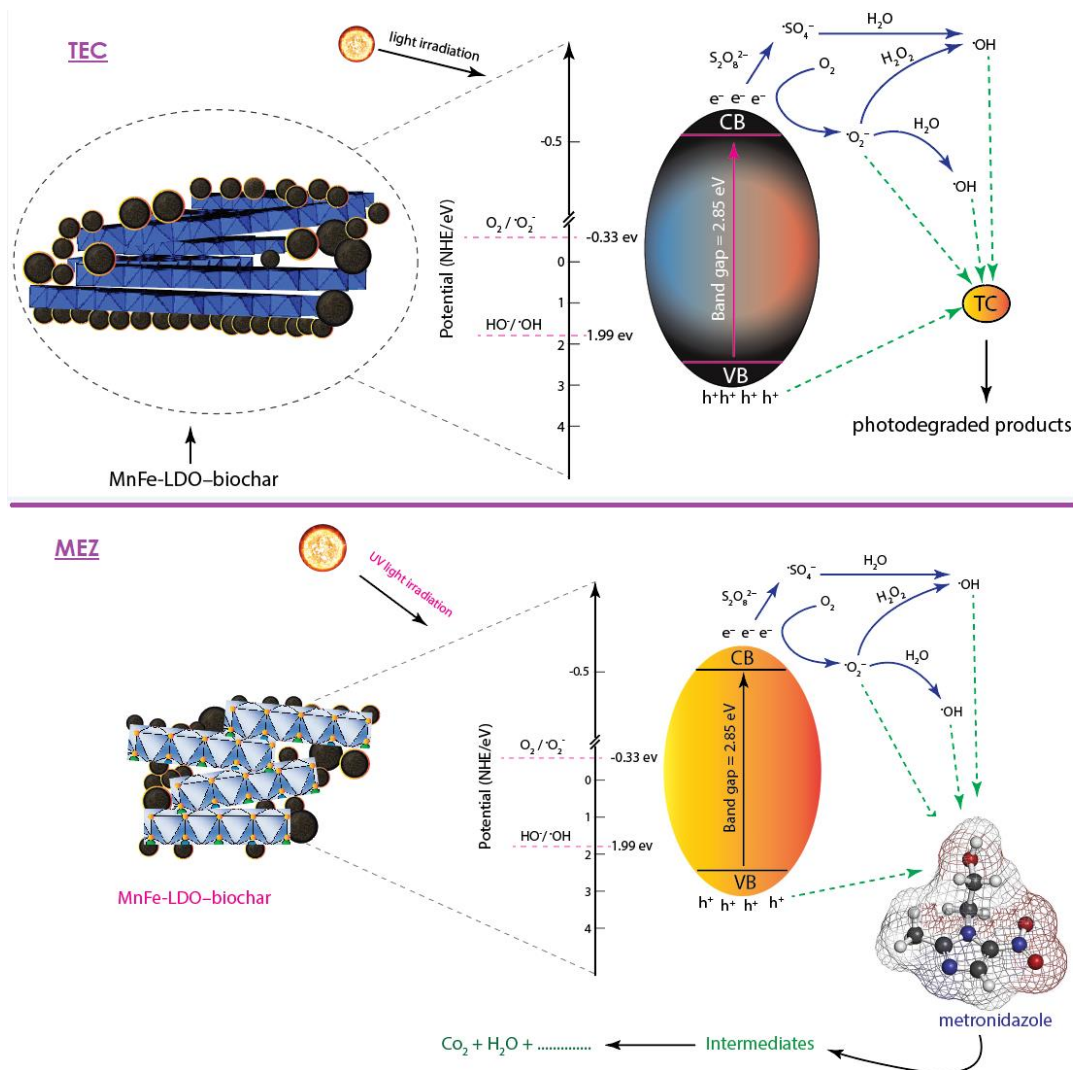
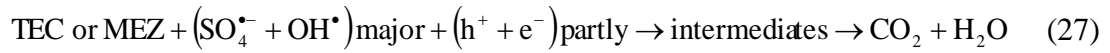
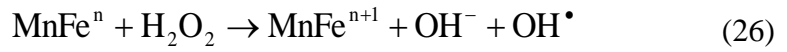


Figure 23: Schematic illustration for the proposed mechanism of TEC and MEZ degradation under UV-light irradiation using MnFe LDO/BC

4.4.7 Comparison of Photocatalytic Performance of MnFe LDO/BC

The photodegradation performance of MnFe LDO/BC for the removal of TEC and MEZ is compared with other reported studies and summarized in Table 14.

Table 14: Comparison of photocatalytic performance of MnFe LDO/BC for TEC and MEZ removal

photocatalyst	Reaction parameters				η (%)	Reference
	pH	Time (min)	Dosage (g/L)	Light source		
TEC						
MnFe LDO/BC	3	120	1.0	UV irradiation (9–30 W, T8, Philips)	99.0	This work
MnFe ₂ O ₄ /bio-char composite	5.5	120	0.5	Visible light irradiation	93.0	Lai et al., 2019
SnO ₂ 2D nanoflakes	-	135	0.27	LED (9 W, 220 V) irradiation and 40 kHz ultrasound	88.8	Yashas et al., 2020
MWCNT/Nd,N,S-TiO ₂	-	240	1.0	Xenon lamp solar simulator	85.8	Mamba et al., 2015
NiS-P zeolite	9.1	180	0.8	Hg lamp	78.5	Ejhih, & Khorsandi 2010
N-doped TiO ₂ coated on glass spheres	-	210	0.4	visible (λ = 400-800 nm), UV light (λ =365 – 400)	Vis:3 1 UV: 41	Vaiano et al., 2015
MEZ						
MnFe LDO/BC	3	60	1.0	UV irradiation (9–30 W, T8, Philips)	98.8	This work
GAC@ZnO composite	11	30	2.0	Ozone generator	83.0	Nasseh et al., 2020
ZnO/Fe ₂ O ₃ /Clinoptilolite/H ₂ O ₂	10	90	1.0	UV (8W, 254nm)	99.9	Davari et al., 2019
UV/TiO ₂	7	120	1.5	UV lamp (100 W)	>70.0	Tran et al. 2019
O ₃ /UV-vis	5	120	-	UV-vis	43.0	Aram et al., 2020
N-TiO ₂ /ZnFe ₂ O ₄ /zeolite/UV-vis	5	120	2.0	UV-vis	70.0	

4.5 Adsorptive Reusability and Photo-stability of MnFe LDO/BC

Composite

This test is very important in the evaluation of the potential of the spent adsorbent/photocatalyst as well as its commercial applications (Alamgira, et al., 2020). After each experiment, the used Mn-Fe LDO/BC was separated from the aqueous medium by using an external magnet, eluted with NaOH and/or deionized water, then dried in a conventional oven at 80°C for 2 h. for successive reuse cycles.

The % removal and % degradation of the spent composite were plotted against the number of cycles as presented in Figure 24 a-b.

In the case of TEC, the removal efficiency of the adsorbent declined from 83.2% to ~66.6% as the number of recycling increase from 1 to 4 cycles. While in MEZ system, no change in the % efficiency of the adsorbent was observed during all the reuse cycles (~84%) (Figure 24 a). As seen in Figure 24 b, the photocatalytic activity of the composite does not decline significantly during the three number of cycles (from 99% to 80%) in both pollutant system, indicating high photocatalytic performance and satisfactory reusability. Therefore, considering the results herein, MnFe LDO/BC is a good alternative adsorbent and photocatalyst that can be used several times without loss in adsorption and photodegradation properties.

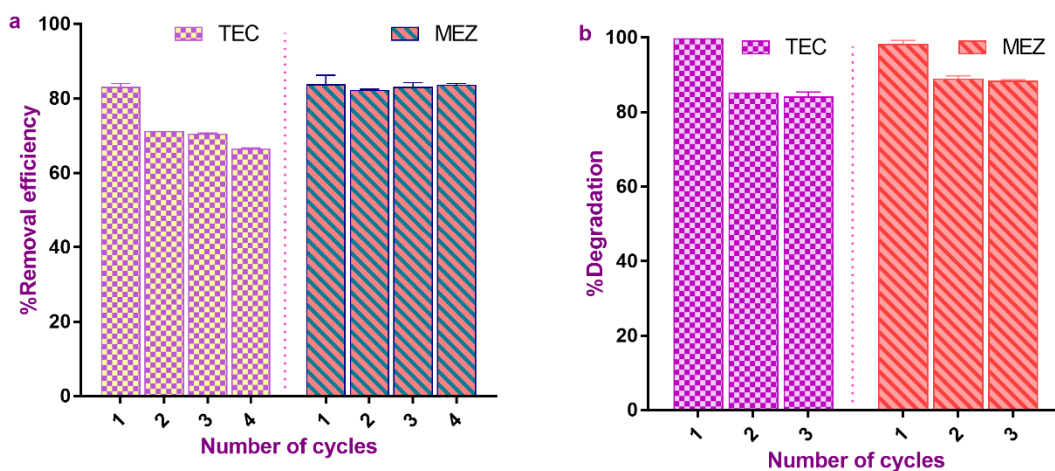


Figure 24: Regeneration and reuse of spent MnFe LDO/BC as adsorbent (a) and photocatalyst (b)

4.6 Evaluation of Adsorption and Photocatalytic Performance of MnFe LDO/BC

According to the tabulated data in Table 15, the MnFe LDO/BC can be used as an effective hybrid material for removal of the antibiotics from wastewater via adsorption and photocatalytic degradation methods.

Table 15: Evaluation of adsorption and photocatalytic performance of MnFe LDO/BC

Parameter*	Adsorption		Photocatalysis	
	TEC	MEZ	TEC	MEZ
pH	3	5	3	5
Dosage (g)	0.05	0.05	0.05	0.05
Reaction time (min)	360	30	120	60
Removal efficiency (%)	83.8	83.8	-	-
Maximum capacity (mg/g)	16.6	16.8	-	-
Oxidant concentration (mM) H ₂ O ₂ /K ₂ S ₂ O ₈	-	-	4/6	6/6
Degradation efficiency (%)	-	-	~98/~98	~98/92

*Under optimized conditions

Chapter 5

CONCLUSION AND FUTURE WORK

In this study, the adsorptive performance of biochar and photocatalytic efficiency of layered double oxide was combined to produce hybrid recyclable material (MnFe LDO/BC) through a co-precipitation technique followed by calcination. The hybrid material was characterized and the results revealed that MnFe LDO/BC possesses sufficiently high surface area ($524.8 \text{ m}^2/\text{g}$), maintained stable photocurrent response of $3.8 \text{ }\mu\text{A}/\text{cm}^2$, possesses varying pores and can be recovered rapidly from the bulk solution due to its saturation magnetization of 28.5 emu/g . The hybrid material performed effectively in removing antibiotics from synthetic solutions of tetracycline and metronidazole antibiotics. The significant results for adsorption and photocatalytic properties of MnFe LDO/BC are summarized herein:

Adsorption studies of MnFe LDO/BC:

- The adsorption of TEC and MEZ by MnFe LDO/BC was greatly influenced by the solution pH. The maximum adsorption was achieved at pH 3 and 5 for them respectively, while the lowest adsorption was obtained at the alkaline conditions.
- As the adsorbent dosage was increased from 0.05 to 0.15 g, the amount of TEC and MEZ adsorbed per unit mass decreased. Therefore, 0.05 g/L was reported as the optimal dosage.

- The adsorption process increased as the initial concentration was changed from 20 to 80 mg/L in both antibiotic systems with time until it reached an optimum level at 360 min for TEC and at 30 min for MEZ removal.
- The removal of TEC and MEZ is fitted well by pseudo-second-order kinetic model; with lowest error functions and highest R^2 values, which implies that this adsorption is possibly controlled by chemisorption.
- The experimental data was fitted Langmuir isotherm model based on its obtained error functions (Δq_e : 4.17 and 0.81 and χ : 0.11 and 0.02) and correlation coefficient R^2 (0.985-0.899) values for TEC and MEZ removal. This indicates a monolayer adsorption onto the surface of MnFe LDO/BC composite. The maximum adsorption capacity q_e for TEC and MEZ was computed 38.3 and 40.8 mg/g, respectively, also, this result was found to be comparable with the other results mentioned above.
- The thermodynamic results revealed that the adsorption of TEC and MEZ by MnFe LDO/BC was spontaneous process, exothermic, and less degree of randomness of the adsorbate, due to the (-) ΔG° , (+) ΔH° , and (-) ΔS° values, respectively.

Photodegradation studies of MnFe LDO/BC:

- The maximum photocatalytic degradation rate for TEC reached ~97.4% and 89.7% at pH 3 in the presence of $K_2S_2O_8$ and H_2O_2 respectively after 120 min UV irradiation. While for MEZ, the maximum photocatalytic degradation (~92% and ~98%) was achieved at pH 5 in the presence of $K_2S_2O_8$ and H_2O_2 after 60 min.

- The degradation efficiency of TEC and MEZ increased from 73.5% to 90.2%, and from 80.2% to 92.9% after 120 min of UV-irradiation, as the composite dosage increased from 25 mg to 50 mg. Therefore, 50 mg (1.0 g/L) was selected as the optimum dosage of MnFe LDO/BC.
- The optimal H₂O₂ concentration in this study was for 4 mM of TEC degradation and 6 mM of MEZ degradation which resulted in ~98% after 120 min and 60 min of UV irradiation, respectively. While, the optimum K₂S₂O₈ concentration of TEC and MEZ degradation was 6 mM resulted in ~98% and 90% after 120 min and 60 min of UV irradiation, respectively.
- The quenching tests revealed that $\cdot\text{OH}$ and $\text{SO}_4^{\cdot-}$ radicals contributed majorly during the TEC and MEZ photodegradation reactions while $\cdot\text{O}_2^-$ and h^+ pairs had a minor contribution.
- Under the optimum experimental conditions; 50 mg of MnFe LDO/BC achieved ~98% TEC and MEZ degradation after 120 min and 60 min upon exposure to UV irradiation with a rate constant of 0.0445 1/min and 0.226 1/min, respectively.

In summary, the prepared MnFe LDO/BC outperformed many other adsorbents and photocatalysts under the optimized conditions for TEC and MEZ removal and maintained stable to reuse after three consequence cycles with ~88% TEC and MEZ degradation efficiency.

In Future Work;

- An extension of the investigations to the treatment of real sewage treatment plant STP effluents is thus required to assess if the prepared MnFe LDO/BC

composite could be successfully applied even in the presence of multipollutant compounds.

- Toxicity of the treated water will help to further characterize the end use of the treated water.
- Following the degradation products via **GC-MS** will help to establish mineralization of pollutants.
- Comparative studies such as anodic oxidation and electro-Fenton processes of a solution containing TEC and MEZ antibiotics could be operated.

REFERENCES

- Ahmad, M., Teel, A. L., Furman, O. S., Reed, J. I., & Watts, R. J. (2012). Oxidative and Reductive Pathways in Iron-Ethylenediaminetetraacetic Acid-Activated Persulfate Systems. *Journal of Environmental Engineering*, 138(4), 411–418. [https://doi.org/10.1061/\(asce\)ee.1943-7870.0000496](https://doi.org/10.1061/(asce)ee.1943-7870.0000496)
- Ahmed, M. J., & Theydan, S. K. (2013). Microwave assisted preparation of microporous activated carbon from Siris seed pods for adsorption of metronidazole antibiotic. *Chemical Engineering Journal*, 214, 310–318. <https://doi.org/10.1016/j.cej.2012.10.101>
- Alamgir, Talha, K., Wang, B., Liu, J. H., Ullah, R., Feng, F., Yu, J., Chen, S., & Li, J. R. (2020). Effective adsorption of metronidazole antibiotic from water with a stable Zr(IV)-MOFs: Insights from DFT, kinetics and thermodynamics studies. *Journal of Environmental Chemical Engineering*, 8(1), 103642. <https://doi.org/10.1016/j.jece.2019.103642>
- Amor, C., Marchão, L., Lucas, M. S., & Peres, J. A. (2019). Application of advanced oxidation processes for the treatment of recalcitrant agro-industrial wastewater: A review. *Water (Switzerland)*, 11(2). <https://doi.org/10.3390/w11020205>
- Andreozzi, R., Caprio, V., Marotta, R., & Radovnikovic, A. (2003). Ozonation and H₂O₂/UV treatment of clofibric acid in water: A kinetic investigation. *Journal of Hazardous Materials*, 103(3), 233–246.

<https://doi.org/10.1016/j.jhazmat.2003.07.001>

Aram, M., Farhadian, M., Solaimany Nazar, A. R., Tangestaninejad, S., Eskandari, P., & Jeon, B. H. (2020). Metronidazole and Cephalexin degradation by using of Urea/TiO₂/ZnFe₂O₄/Clinoptilolite catalyst under visible-light irradiation and ozone injection. *Journal of Molecular Liquids*, 304, 112764. <https://doi.org/10.1016/j.molliq.2020.112764>

Asgari, E., Esrafil, A., Jafari, A. J., Kalantary, R. R., Nourmoradi, H., & Farzadkia, M. (2019). The comparison of ZnO/polyaniline nanocomposite under UV and visible radiations for decomposition of metronidazole: Degradation rate, mechanism and mineralization. *Process Safety and Environmental Protection*, 128, 65–76. <https://doi.org/10.1016/j.psep.2019.05.050>

Atacan, K., Güy, N., Boutra, B., & Özacar, M. (2020). Enhancement of photoelectrochemical hydrogen production by using a novel ternary Ag₂CrO₄/GO/MnFe₂O₄ photocatalyst. *International Journal of Hydrogen Energy*, 45(35), 17453–17467. <https://doi.org/10.1016/j.ijhydene.2020.04.268>

Awode, A. U., Oladipo, A. A., Guran, M., Yilmaz, O., & Gazi, M. (2020). Fabrication of trichlorovinylsilane-modified-chitosan film with enhanced solubility and antibacterial activity. *Polymer Bulletin*, 77(11), 5811–5824. <https://doi.org/10.1007/s00289-019-03056-8>

Ayeni, A. O., Daramola, M. O., Sekoai, P. T., Adeeyo, O., Garba, M. J., & Awosusi,

- A. A. (2018). Statistical modelling and optimization of alkaline peroxide oxidation pretreatment process on rice husk cellulosic biomass to enhance enzymatic convertibility and fermentation to ethanol. *Cellulose*, 25(4), 2487–2504. <https://doi.org/10.1007/s10570-018-1714-6>
- Balarak, D., Igwegbe, C. A., & Onyechi, P. C. (2019). Photocatalytic degradation of metronidazole using BIOI-MWCNT composites: synthesis, characterization, and operational parameters. *Sigma J Eng & Nat Sci*, 37(4), 1231–1245.
- Bashiri, F., Khezri, S. M., Kalantary, R. R., & Kakavandi, B. (2020). Enhanced photocatalytic degradation of metronidazole by TiO₂ decorated on magnetic reduced graphene oxide: Characterization, optimization and reaction mechanism studies. *Journal of Molecular Liquids*, 314, 113608. <https://doi.org/10.1016/j.molliq.2020.113608>
- Basu, M., Guha, A. K., & Ray, L. (2017). Adsorption of Lead on Cucumber Peel. *Journal of Cleaner Production*, 151, 603–615. <https://doi.org/10.1016/j.jclepro.2017.03.028>
- Brigante, M., & Schulz, P. C. (2011). Remotion of the antibiotic tetracycline by titania and titania-silica composed materials. *Journal of Hazardous Materials*, 192(3), 1597–1608. <https://doi.org/10.1016/j.jhazmat.2011.06.082>
- Carrales-Alvarado, D. H., Ocampo-Pérez, R., Leyva-Ramos, R., & Rivera-Utrilla, J.

- (2014). Removal of the antibiotic metronidazole by adsorption on various carbon materials from aqueous phase. *Journal of Colloid and Interface Science*, *436*, 276–285. <https://doi.org/10.1016/j.jcis.2014.08.023>
- Cazetta, A. L., Pezoti, O., Bedin, K. C., Silva, T. L., Paesano Junior, A., Asefa, T., & Almeida, V. C. (2016). Magnetic Activated Carbon Derived from Biomass Waste by Concurrent Synthesis: Efficient Adsorbent for Toxic Dyes. *ACS Sustainable Chemistry and Engineering*, *4*(3), 1058–1068. <https://doi.org/10.1021/acssuschemeng.5b01141>
- Chan, Y. H., Yusup, S., Quitain, A. T., Tan, R. R., Sasaki, M., Lam, H. L., & Uemura, Y. (2015). Effect of process parameters on hydrothermal liquefaction of oil palm biomass for bio-oil production and its life cycle assessment. *Energy Conversion and Management*, *104*, 180–188. <https://doi.org/10.1016/j.enconman.2015.03.075>
- Chen, Meiqing, Wu, P., Huang, Z., Liu, J., Li, Y., Zhu, N., Dang, Z., & Bi, Y. (2019). Environmental application of MgMn-layered double oxide for simultaneous efficient removal of tetracycline and Cd pollution: Performance and mechanism. *Journal of Environmental Management*, *246*(March), 164–173. <https://doi.org/10.1016/j.jenvman.2019.06.002>
- Chen, Ming, Zhao, J., & Xia, L. (2009). Comparison of four different chemical pretreatments of corn stover for enhancing enzymatic digestibility. *Biomass and Bioenergy*, *33*(10), 1381–1385. <https://doi.org/10.1016/j.biombioe.2009.05.025>

- Dai, Z., Shi, X., Liu, H., Li, H., Han, Y., & Zhou, J. (2018). High-strength lignin-based carbon fibers via a low-energy method. *RSC Advances*, 8(3), 1218–1224. <https://doi.org/10.1039/c7ra10821d>
- Davari, N., Farhadian, M., & Solaimany Nazar, A. R. (2019). Synthesis and characterization of Fe₂O₃ doped ZnO supported on clinoptilolite for photocatalytic degradation of metronidazole. *Environmental Technology (United Kingdom)*, 0(0), 1–13. <https://doi.org/10.1080/09593330.2019.1680738>
- Derikvandi, H., & Nezamzadeh-Ejchieh, A. (2017). Comprehensive study on enhanced photocatalytic activity of heterojunction ZnS-NiS/zeolite nanoparticles: Experimental design based on response surface methodology (RSM), impedance spectroscopy and GC-MASS studies. *Journal of Colloid and Interface Science*, 490, 652–664. <https://doi.org/10.1016/j.jcis.2016.11.105>
- Essawy, A. A., Alsohaimi, I. H., Alhumaimess, M. S., Hassan, H. M. A., & Kamel, M. M. (2020). Green synthesis of spongy Nano-ZnO productive of hydroxyl radicals for unconventional solar-driven photocatalytic remediation of antibiotic enriched wastewater. *Journal of Environmental Management*, 271(February), 110961. <https://doi.org/10.1016/j.jenvman.2020.110961>
- Farzadkia, M., Bazrafshan, E., Esrafil, A., Yang, J. K., & Shirzad-Siboni, M. (2015). Photocatalytic degradation of Metronidazole with illuminated TiO₂ nanoparticles. *Journal of Environmental Health Science and Engineering*,

13(1), 1–8. <https://doi.org/10.1186/s40201-015-0194-y>

Gazi, M., Oladipo, A. A., Ojoro, Z. E., & Gulcan, H. O. (2017). High-Performance Nanocatalyst for Adsorptive and Photo-Assisted Fenton-Like Degradation of Phenol: Modeling Using Artificial Neural Networks. *Chemical Engineering Communications*, 204(7), 729–738. <https://doi.org/10.1080/00986445.2017.1311253>

Gong, J. L., Wang, B., Zeng, G. M., Yang, C. P., Niu, C. G., Niu, Q. Y., Zhou, W. J., & Liang, Y. (2009). Removal of cationic dyes from aqueous solution using magnetic multi-wall carbon nanotube nanocomposite as adsorbent. *Journal of Hazardous Materials*, 164(2–3), 1517–1522. <https://doi.org/10.1016/j.jhazmat.2008.09.072>

Hassanein, T. F., & Koumanova, B. (2010). Evaluation of Adsorption Potential of the Agricultural Waste Wheat Straw for Basic Yellow 21. *Koumanova Journal of the University of Chemical Technology and Metallurgy*, 45(4), 407–414.

Hazime, R., Nguyen, Q. H., Ferronato, C., Salvador, A., Jaber, F., & Chovelon, J. M. (2014). Comparative study of imazalil degradation in three systems: UV/TiO₂, UV/K₂S₂O₈ and UV/TiO₂/K₂S₂O₈. *Applied Catalysis B: Environmental*, 144, 286–291. <https://doi.org/10.1016/j.apcatb.2013.07.001>

He, Y., Dong, W., Li, X., Wang, D., Yang, Q., Deng, P., & Huang, J. (2020). Modified MIL-100(Fe) for enhanced photocatalytic degradation of

tetracycline under visible-light irradiation. *Journal of Colloid and Interface Science*, 574, 364–376. <https://doi.org/10.1016/j.jcis.2020.04.075>

Hena, S., Gutierrez, L., & Croué, J. P. (2020). Removal of metronidazole from aqueous media by *C. vulgaris*. *Journal of Hazardous Materials*, 384(October 2019). <https://doi.org/10.1016/j.jhazmat.2019.121400>

Heng, K. S., Hatti-Kaul, R., Adam, F., Fukui, T., & Sudesh, K. (2017). Conversion of rice husks to polyhydroxyalkanoates (PHA) via a three-step process: optimized alkaline pretreatment, enzymatic hydrolysis, and biosynthesis by *Burkholderia cepacia* USM (JCM 15050). *Journal of Chemical Technology and Biotechnology*, 92(1), 100–108. <https://doi.org/10.1002/jctb.4993>

Hong, Y., Peng, J., Zhao, X., Yan, Y., Lai, B., & Yao, G. (2019). Efficient degradation of atrazine by CoMgAl layered double oxides catalyzed peroxymonosulfate: Optimization, degradation pathways and mechanism. *Chemical Engineering Journal*, 370(March), 354–363. <https://doi.org/10.1016/j.cej.2019.03.127>

Hou, L., Li, X., Yang, Q., Chen, F., Wang, S., Ma, Y., Wu, Y., Zhu, X., Huang, X., & Wang, D. (2019). Heterogeneous activation of peroxymonosulfate using Mn-Fe layered double hydroxide: Performance and mechanism for organic pollutant degradation. *Science of the Total Environment*, 663, 453–464. <https://doi.org/10.1016/j.scitotenv.2019.01.190>

Ifebajo, A. O., Oladipo, A. A., & Gazi, M. (2019). Efficient removal of tetracycline

by CoO/CuFe₂O₄ derived from layered double hydroxides. *Environmental Chemistry Letters*, 17(1), 487–494. <https://doi.org/10.1007/s10311-018-0781-0>

Ifebajo, A. O., Oladipo, A. A., & Gazi, M. (2020). Sun-light driven enhanced azo dye decontamination from aqueous solution by CoO-CuFe₂O₄ derived from layered double hydroxide. *Desalination and Water Treatment*, 177(May 2019), 423–430. <https://doi.org/10.5004/dwt.2020.25247>

Jain, M., Manju, Savita, Vij, A., & Thakur, A. (2020). Activation of multiple defects in zinc aluminate through gamma and UV irradiation. *Vacuum*, 180(June), 109600. <https://doi.org/10.1016/j.vacuum.2020.109600>

Jiang, Z., Chen, K., Zhang, Y., Wang, Y., Wang, F., Zhang, G., & Dionysiou, D. D. (2020). Magnetically recoverable MgFe₂O₄/conjugated polyvinyl chloride derivative nanocomposite with higher visible-light photocatalytic activity for treating Cr(VI)-polluted water. *Separation and Purification Technology*, 236(November 2019), 116272. <https://doi.org/10.1016/j.seppur.2019.116272>

Kalhuri, E. M., Al-Musawi, T. J., Ghahramani, E., Kazemian, H., & Zarrabi, M. (2017). Enhancement of the adsorption capacity of the light-weight expanded clay aggregate surface for the metronidazole antibiotic by coating with MgO nanoparticles: Studies on the kinetic, isotherm, and effects of environmental parameters. *Chemosphere*, 175, 8–20. <https://doi.org/10.1016/j.chemosphere.2017.02.043>

- Kang, J., Liu, H., Zheng, Y. M., Qu, J., & Chen, J. P. (2010). Systematic study of synergistic and antagonistic effects on adsorption of tetracycline and copper onto a chitosan. *Journal of Colloid and Interface Science*, 344(1), 117–125. <https://doi.org/10.1016/j.jcis.2009.11.049>
- Konicki, W., Hełminiak, A., Arabczyk, W., & Mijowska, E. (2017). Removal of anionic dyes using magnetic Fe@graphite core-shell nanocomposite as an adsorbent from aqueous solutions. *Journal of Colloid and Interface Science*, 497, 155–164. <https://doi.org/10.1016/j.jcis.2017.03.008>
- Lai, C., Huang, F., Zeng, G., Huang, D., Qin, L., Cheng, M., Zhang, C., Li, B., Yi, H., Liu, S., Li, L., & Chen, L. (2019). Fabrication of novel magnetic MnFe₂O₄/bio-char composite and heterogeneous photo-Fenton degradation of tetracycline in near neutral pH. *Chemosphere*, 224, 910–921. <https://doi.org/10.1016/j.chemosphere.2019.02.193>
- Li, R., Li, W., Jin, C., He, Q., & Wang, Y. (2020). Fabrication of ZIF-8@TiO₂ micron composite via hydrothermal method with enhanced absorption and photocatalytic activities in tetracycline degradation. *Journal of Alloys and Compounds*, 825, 154008. <https://doi.org/10.1016/j.jallcom.2020.154008>
- Li, X., Hou, T., Yan, L., Shan, L., Meng, X., & Zhao, Y. (2020). Efficient degradation of tetracycline by CoFeLa-layered double hydroxides catalyzed peroxymonosulfate: Synergistic effect of radical and nonradical pathways. *Journal of Hazardous Materials*, 398(February). <https://doi.org/10.1016/j.jhazmat.2020.122884>

- Li, Z., Schulz, L., Ackley, C., & Fenske, N. (2010). Adsorption of tetracycline on kaolinite with pH-dependent surface charges. *Journal of Colloid and Interface Science*, 351(1), 254–260. <https://doi.org/10.1016/j.jcis.2010.07.034>
- Liao, Y. Te, Matsagar, B. M., & Wu, K. C. W. (2018). Metal-Organic Framework (MOF)-Derived Effective Solid Catalysts for Valorization of Lignocellulosic Biomass. *ACS Sustainable Chemistry and Engineering*, 6(11), 13628–13643. <https://doi.org/10.1021/acssuschemeng.8b03683>
- Lin, J. C. Te, de Luna, M. D. G., Aranzamendez, G. L., & Lu, M. C. (2016). Degradations of acetaminophen via a K₂S₂O₈-doped TiO₂ photocatalyst under visible light irradiation. *Chemosphere*, 155, 388–394. <https://doi.org/10.1016/j.chemosphere.2016.04.059>
- Liu, H., Yang, Y., Kang, J., Fan, M., & Qu, J. (2012). Removal of tetracycline from water by Fe-Mn binary oxide. *Journal of Environmental Sciences*, 24(2), 242–247. [https://doi.org/10.1016/S1001-0742\(11\)60763-8](https://doi.org/10.1016/S1001-0742(11)60763-8)
- Lv, Z., Yang, S., Zhu, H., Chen, L., Alharbi, N. S., Wakeel, M., Wahid, A., & Chen, C. (2018). Highly efficient removal of As(V) by using NiAl layered double oxide composites. *Applied Surface Science*, 448, 599–608. <https://doi.org/10.1016/j.apsusc.2018.04.162>
- Mamba, G., Mbianda, X. Y., & Mishra, A. K. (2015). Photocatalytic degradation of the diazo dye naphthol blue black in water using MWCNT/Gd,N,S-TiO₂

nanocomposites under simulated solar light. *Journal of Environmental Sciences (China)*, 33, 219–228. <https://doi.org/10.1016/j.jes.2014.06.052>

Manikandan, A., Hema, E., Durka, M., Seevakan, K., Alagesan, T., & Arul Antony, S. (2015). Room Temperature Ferromagnetism of Magnetically Recyclable Photocatalyst of $\text{Cu}_{1-x}\text{Mn}_x\text{Fe}_2\text{O}_4\text{-TiO}_2$ ($0.0 \leq x \leq 0.5$) Nanocomposites. *Journal of Superconductivity and Novel Magnetism*, 28(6), 1783–1795. <https://doi.org/10.1007/s10948-014-2945-x>

Martins, A. C., Pezoti, O., Cazetta, A. L., Bedin, K. C., Yamazaki, D. A. S., Bandoch, G. F. G., Asefa, T., Visentainer, J. V., & Almeida, V. C. (2015). Removal of tetracycline by NaOH-activated carbon produced from macadamia nut shells: Kinetic and equilibrium studies. *Chemical Engineering Journal*, 260, 291–299. <https://doi.org/10.1016/j.cej.2014.09.017>

Matzek, L. W., & Carter, K. E. (2016). Activated persulfate for organic chemical degradation: A review. *Chemosphere*, 151, 178–188. <https://doi.org/10.1016/j.chemosphere.2016.02.055>

Mo, J., Yang, Q., Zhang, N., Zhang, W., Zheng, Y., & Zhang, Z. (2018). A review on agro-industrial waste (AIW) derived adsorbents for water and wastewater treatment. *Journal of Environmental Management*, 227(August), 395–405. <https://doi.org/10.1016/j.jenvman.2018.08.069>

Nasseh, N., Arghavan, F. S., Rodriguez-Couto, S., Hossein Panahi, A., Esmati, M.,

& A-Musawi, T. J. (2020). Preparation of activated carbon@ZnO composite and its application as a novel catalyst in catalytic ozonation process for metronidazole degradation. *Advanced Powder Technology*, *31*(2), 875–885. <https://doi.org/10.1016/j.appt.2019.12.006>

Nezamzadeh-Ejhieh, A., & Khorsandi, M. (2010). Photodecolorization of Eriochrome Black T using NiS-P zeolite as a heterogeneous catalyst. *Journal of Hazardous Materials*, *176*(1–3), 629–637. <https://doi.org/10.1016/j.jhazmat.2009.11.077>

Oh, W. Da, Dong, Z., & Lim, T. T. (2016). Generation of sulfate radical through heterogeneous catalysis for organic contaminants removal: Current development, challenges and prospects. *Applied Catalysis B: Environmental*, *194*, 169–201. <https://doi.org/10.1016/j.apcatb.2016.04.003>

Oladipo, A. A. (2018). MIL-53 (Fe)-based photo-sensitive composite for degradation of organochlorinated herbicide and enhanced reduction of Cr(VI). *Process Safety and Environmental Protection*, *116*, 413–423. <https://doi.org/10.1016/j.psep.2018.03.011>

Oladipo, A. A., & Gazi, M. (2015a). Microwaves initiated synthesis of activated carbon-based composite hydrogel for simultaneous removal of copper(II) ions and direct red 80 dye: A multi-component adsorption system. *Journal of the Taiwan Institute of Chemical Engineers*, *47*, 125–136. <https://doi.org/10.1016/j.jtice.2014.09.027>

- Oladipo, A. A., & Gazi, M. (2015b). Nickel removal from aqueous solutions by alginate-based composite beads: Central composite design and artificial neural network modeling. *Journal of Water Process Engineering*, 8, e81–e91. <https://doi.org/10.1016/j.jwpe.2014.12.002>
- Oladipo, A. A., & Ifebajo, A. O. (2018). Highly efficient magnetic chicken bone biochar for removal of tetracycline and fluorescent dye from wastewater: Two-stage adsorber analysis. *Journal of Environmental Management*, 209, 9–16. <https://doi.org/10.1016/j.jenvman.2017.12.030>
- Oladipo, A. A., Ifebajo, A. O., & Gazi, M. (2019). Magnetic LDH-based CoO–NiFe₂O₄ catalyst with enhanced performance and recyclability for efficient decolorization of azo dye via Fenton-like reactions. *Applied Catalysis B: Environmental*, 243, 243–252. <https://doi.org/10.1016/J.APCATB.2018.10.050>
- Omo-Okoro, P. N., Daso, A. P., & Okonkwo, J. O. (2018). A review of the application of agricultural wastes as precursor materials for the adsorption of per- and polyfluoroalkyl substances: A focus on current approaches and methodologies. *Environmental Technology and Innovation*, 9, 100–114. <https://doi.org/10.1016/j.eti.2017.11.005>
- Oturan, M. A., & Aaron, J. J. (2014). Advanced oxidation processes in water/wastewater treatment: Principles and applications. A review. *Critical Reviews in Environmental Science and Technology*, 44(23), 2577–2641. <https://doi.org/10.1080/10643389.2013.829765>

- Ouyang, D., Yan, J., Qian, L., Chen, Y., Han, L., Su, A., Zhang, W., Ni, H., & Chen, M. (2017). Degradation of 1,4-dioxane by biochar supported nano magnetite particles activating persulfate. *Chemosphere*, *184*, 609–617. <https://doi.org/10.1016/j.chemosphere.2017.05.156>
- Patnaik, S., Sahoo, D. P., Mohapatra, L., Martha, S., & Parida, K. (2017). ZnCr₂O₄@ZnO/g-C₃N₄: A Triple-Junction Nanostructured Material for Effective Hydrogen and Oxygen Evolution under Visible Light. *Energy Technology*, *5*(9), 1687–1701. <https://doi.org/10.1002/ente.201700071>
- Qiao, D., Li, Z., Duan, J., & He, X. (2020). Adsorption and photocatalytic degradation mechanism of magnetic graphene oxide/ZnO nanocomposites for tetracycline contaminants. *Chemical Engineering Journal*, *400*(June), 125952. <https://doi.org/10.1016/j.cej.2020.125952>
- Rasheed, H. U., Lv, X., Zhang, S., Wei, W., ullah, N., & Xie, J. (2018). Ternary MIL-100(Fe)@Fe₃O₄/CA magnetic nanophotocatalysts (MNPCs): Magnetically separable and Fenton-like degradation of tetracycline hydrochloride. *Advanced Powder Technology*, *29*(12), 3305–3314. <https://doi.org/10.1016/j.appt.2018.09.011>
- Rathod, M., Haldar, S., & Basha, S. (2015). Nanocrystalline cellulose for removal of tetracycline hydrochloride from water via biosorption: Equilibrium, kinetic and thermodynamic studies. *Ecological Engineering*, *84*, 240–249. <https://doi.org/10.1016/j.ecoleng.2015.09.031>

- Ren, J., Qian, B., Li, J., Song, Z., Hao, L., & Shi, J. (2016). Highly efficient polypyrrole sensitized TiO₂ nanotube films for photocathodic protection of Q235 carbon steel. *Corrosion Science*, *111*(June), 596–601. <https://doi.org/10.1016/j.corsci.2016.06.001>
- Robl, D., dos Santos Costa, P., Rabelo, S. C., da Silva Delabona, P., da Silva Lima, D. J., Padilla, G., & da Cruz Pradella, J. G. (2016). Use of Ascomycete Extracts in Enzymatic Cocktail Formulations Increases Sugar Cane Bagasse Hydrolysis. *Bioenergy Research*, *9*(2), 559–565. <https://doi.org/10.1007/s12155-016-9721-7>
- Rohowsky, B., Häßler, T., Gladis, A., Remmele, E., Schieder, D., & Faulstich, M. (2013). Feasibility of simultaneous saccharification and juice co-fermentation on hydrothermal pretreated sweet sorghum bagasse for ethanol production. *Applied Energy*, *102*, 211–219. <https://doi.org/10.1016/j.apenergy.2012.03.039>
- Ruiz, E., Romero, I., Moya, M., Cara, C., Vidal, J. D., & Castro, E. (2013). Dilute sulfuric acid pretreatment of sunflower stalks for sugar production. *Bioresource Technology*, *140*, 292–298. <https://doi.org/10.1016/j.biortech.2013.04.104>
- Salari Mehr, M., Akbari, A., & Damerchi, E. (2019). Electrodeposited Ni-B/SiC micro- and nano-composite coatings: A comparative study. *Journal of Alloys and Compounds*, *782*, 477–487. <https://doi.org/10.1016/j.jallcom.2018.12.184>

- Shang, S. S., & Gao, S. (2019). Heteroatom-Enhanced Metal-Free Catalytic Performance of Carbocatalysts for Organic Transformations. *ChemCatChem*, *11*(16), 3730–3744. <https://doi.org/10.1002/cctc.201900336>
- Shao, L., Ren, Z., Zhang, G., & Chen, L. (2012). Facile synthesis, characterization of a MnFe₂O₄/activated carbon magnetic composite and its effectiveness in tetracycline removal. *Materials Chemistry and Physics*, *135*(1), 16–24. <https://doi.org/10.1016/j.matchemphys.2012.03.035>
- Shen, J. C., Zeng, H. Y., Chen, C. R., & Xu, S. (2020). A facile fabrication of Ag₂O-Ag/ZnAl-oxides with enhanced visible-light photocatalytic performance for tetracycline degradation. *Applied Clay Science*, *185*(August 2019), 105413. <https://doi.org/10.1016/j.clay.2019.105413>
- Song, Z., Gao, H., Zhang, W., & Wang, D. (2020). Reinforce of hydrotalcite-like loaded TiO₂ composite material prepared by Ti-bearing blast furnace slag for photo-degradation of tetracycline. *Journal of Water Process Engineering*, *36*(May), 101399. <https://doi.org/10.1016/j.jwpe.2020.101399>
- Tran, M. L., Fu, C. C., & Juang, R. S. (2019). Removal of metronidazole and amoxicillin mixtures by UV/TiO₂ photocatalysis: an insight into degradation pathways and performance improvement. *Environmental Science and Pollution Research*, *26*(12), 11846–11855. <https://doi.org/10.1007/s11356-019-04683-4>
- Vaiano, V., Sacco, O., Sannino, D., & Ciambelli, P. (2015). Nanostructured N-doped

TiO₂ coated on glass spheres for the photocatalytic removal of organic dyes under UV or visible light irradiation. *Applied Catalysis B: Environmental*, 170–171, 153–161. <https://doi.org/10.1016/j.apcatb.2015.01.039>

Vu, B. K., Shin, E. W., Snisarenko, O., Jeong, W. S., & Lee, H. S. (2010). Removal of the antibiotic tetracycline by Fe-impregnated SBA-15. *Korean Journal of Chemical Engineering*, 27(1), 116–120. <https://doi.org/10.1007/s11814-009-0313-5>

Wang, J., Hu, J., & Zhang, S. (2010). Studies on the sorption of tetracycline onto clays and marine sediment from seawater. *Journal of Colloid and Interface Science*, 349(2), 578–582. <https://doi.org/10.1016/j.jcis.2010.04.081>

Wang, L., Yang, M., Fan, X., Zhu, X., Xu, T., & Yuan, Q. (2011). An environmentally friendly and efficient method for xylitol bioconversion with high-temperature-steaming corncob hydrolysate by adapted *Candida tropicalis*. *Process Biochemistry*, 46(8), 1619–1626. <https://doi.org/10.1016/j.procbio.2011.05.004>

Woods, R., Kolthoff, I. M., & Meehan, E. J. (1963). Arsenic(IV) as an Intermediate in the Induced Oxidation of Arsenic(III) by the Iron(II)-Persulfate Reaction and the Photoreduction of Iron(III). I. Absence of Oxygen. *Journal of the American Chemical Society*, 85(16), 2385–2390. <https://doi.org/10.1021/ja00899a010>

Wu, S., Hu, H., Lin, Y., Zhang, J., & Hu, Y. H. (2020). Visible light photocatalytic

degradation of tetracycline over TiO₂. *Chemical Engineering Journal*, 382(June 2019), 122842. <https://doi.org/10.1016/j.cej.2019.122842>

Yan, J., Lei, M., Zhu, L., Anjum, M. N., Zou, J., & Tang, H. (2011). Degradation of sulfamonomethoxine with Fe₃O₄ magnetic nanoparticles as heterogeneous activator of persulfate. *Journal of Hazardous Materials*, 186(2–3), 1398–1404. <https://doi.org/10.1016/j.jhazmat.2010.12.017>

Yashas, S. R., Shivaraju, H. P., Thinley, T., Pushparaj, K. S., Maleki, A., & Shahmoradi, B. (2020). Facile synthesis of SnO₂ 2D nanoflakes for ultrasound-assisted photodegradation of tetracycline hydrochloride. *International Journal of Environmental Science and Technology*, 17(5), 2593–2604. <https://doi.org/10.1007/s13762-020-02636-w>

Zeng, Z. W., Tian, S. R., Liu, Y. G., Tan, X. F., Zeng, G. M., Jiang, L. H., Yin, Z. H., Liu, N., Liu, S. B., & Li, J. (2018). Comparative study of rice husk biochars for aqueous antibiotics removal. *Journal of Chemical Technology and Biotechnology*, 93(4), 1075–1084. <https://doi.org/10.1002/jctb.5464>

Zhang, Gaosheng, Liu, H., Liu, R., & Qu, J. (2009). Adsorption behavior and mechanism of arsenate at Fe-Mn binary oxide/water interface. *Journal of Hazardous Materials*, 168(2–3), 820–825. <https://doi.org/10.1016/j.jhazmat.2009.02.137>

Zhang, Guanhua, Zhang, X., Meng, Y., Pan, G., Ni, Z., & Xia, S. (2020). Layered double hydroxides-based photocatalysts and visible-light driven

photodegradation of organic pollutants: A review. *Chemical Engineering Journal*, 392(November), 123684. <https://doi.org/10.1016/j.cej.2019.123684>

Zhang, J., Zhu, K., Zhu, Y., Qin, C., Liu, L., Liu, D., Wang, Y., Gan, W., Fu, X., & Hao, H. (2020). Enhanced photocatalytic degradation of tetracycline hydrochloride by Al-doped BiOCl microspheres under simulated sunlight irradiation. *Chemical Physics Letters*, 750(April), 137483. <https://doi.org/10.1016/j.cplett.2020.137483>

Zhang, X., Feng, M., Qu, R., Liu, H., Wang, L., & Wang, Z. (2016). Catalytic degradation of diethyl phthalate in aqueous solution by persulfate activated with nano-scaled magnetic CuFe₂O₄/MWCNTs. *Chemical Engineering Journal*, 301, 1–11. <https://doi.org/10.1016/j.cej.2016.04.096>

Zhao, W., Wei, Z., Zhang, X., Ding, M., Huang, S., & Yang, S. (2020). Magnetic recyclable MnFe₂O₄/CeO₂/SnS₂ ternary nano-photocatalyst for photo-Fenton degradation. *Applied Catalysis A: General*, 593(December 2019). <https://doi.org/10.1016/j.apcata.2020.117443>

Zhen, L., He, K., Xu, C. Y., & Shao, W. Z. (2008). Synthesis and characterization of single-crystalline MnFe₂O₄ nanorods via a surfactant-free hydrothermal route. *Journal of Magnetism and Magnetic Materials*, 320(21), 2672–2675. <https://doi.org/10.1016/j.jmmm.2008.05.034>

Zhu, B., Cheng, H., Qin, Y., Ma, J., Kong, Y., & Komarneni, S. (2020). Copper sulfide as an excellent co-catalyst with K₂S₂O₈ for dye decomposition in

advanced oxidation process. *Separation and Purification Technology*, 233(August 2019), 116057. <https://doi.org/10.1016/j.seppur.2019.116057>

Zhu, C., Fang, G., Dionysiou, D. D., Liu, C., Gao, J., Qin, W., & Zhou, D. (2016). Efficient transformation of DDTs with Persulfate Activation by Zero-valent Iron Nanoparticles: A Mechanistic Study. *Journal of Hazardous Materials*, 316, 232–241. <https://doi.org/10.1016/j.jhazmat.2016.05.040>